

DISS. ETH No. 30280

GROUND STATE COOLING
AND FREE FALL EVOLUTIONS
WITH LEVITATED NANOPARTICLES

A thesis submitted to attain the degree of

DOCTOR OF SCIENCES

(Dr. sc. ETH Zurich)

presented by

MARIA LUISA MATTANA

Laurea Magistrale in Fisica, Università degli Studi di Cagliari

born on 30.04.1995

accepted on the recommendation of

Prof. Dr. Lukas Novotny, examiner

Prof. Dr. Ruth Signorell, co-examiner

Prof. Dr. Bas Hensen, co-examiner

2024

The work described in this thesis is part of the Q-Xtreme research program, which is financially supported by the European Research Council (ERC), under the European Union's Horizon 2020 research and innovation programme (Grant agreement ID: 951234).

This work was carried out at the
Photonics Laboratory,
ETH Zürich, D-ITET,
HPP, Hönggerbergring 64, 8093 Zürich

There's more to them
than meets the eye.

- Optimus Prime

Acknowledgements

The completion of this work would not have been possible without the help and input from many of my colleagues and friends throughout the years.

With regards to the first project presented in this thesis, the idea of realizing a quantum ground state with a trapped femtogram mass predates my arrival in the group. The cryogenic setup (built ad hoc for the experiment here presented with help from Felix Tebbenjohanns and Massimiliano Rossi) is based on a room temperature platform designed by Felix and Vijay Jain. The electronics used to exert the active feedback on the particle were developed by Felix, who also worked on much of the data analysis and theory, and the study of the cross-sideband correlation thermometry.

Massimiliano Rossi developed the mathematical description of the in-loop detection, and took care of much of the data analysis and theory groundwork for the experiment.

I personally thank Fons van der Laan for his help towards the geometrical characterization of the trapped nanoparticles, which greatly improved their chances of survival in the cryo-trap.

Martin Frimmer and Lukas Novotny suggested the idea for the second experiment described in this work. The pioneering work of Erik Hebestreit puts the basis for many of the concepts on which the project is founded.

Throughout the development of the platform, "Titta" Nicola Carlon Zambon and Massimiliano Rossi helped me greatly both in planning the technical

improvements to the setup, but also for the theory development. Their support, know-how, and (especially) patience were fundamental for the success of the experiment. To them goes my most sincere gratitude.

I thank Andrei Militaru for the fruitful discussions and help with tackling the Langevin Equation.

Eric Bonvin taught me how to program the FPGAs needed for the timing of the protocol. Discussions with him and Louisiane Devaud were also instrumental for the completion of the phase space reconstruction which we present in this work.

Dr. Olivier Faist from Zurich Instruments provided crucial insights for the completion of the experiment. I sincerely thank him for his timely help and discussions, which greatly helped us improve the repeatability of our protocol.

I thank also the entirety of the Trappers' division of the Photonics Laboratory, for sharing their knowledge along the way during our dedicated meetings, where I could exchange ideas also with Patrick Back, Laric Bobzien, Moritz Cavigelli, Lorenzo Dania, Danut-Valentin Dinu, Jialiang Gao, Andreas Normann, Johannes Piotrowski, René Reimann, Paolo Seta, Martynas Skrabulis, Jayadev Vijayan, Dominik Windey, and Joanna Zielinska.

It would not have been possible to complete both of these projects in only four years without the generosity of Jialiang Gao, who countless times supplied the setups with his own experimental equipment, and always lent an ear when I needed to unravel my thoughts.

On the same note, I sincerely thank Yang Xu, for his encouragement during the last stages of the data acquisition, and for his immense patience in taking care of some of the duties I could not keep up with during the thesis writing.

A great "thank you!" goes also to Shengyu Shen, for lifting my spirits during this last writing period, both with her amazing energy, and with her amazing food, too!

Especially towards the last stages of my studies, the wisdom shared by Sotirios Papadopoulos has for sure been a precious guide. I thank him, Fons

van der Laan, and Ronja Khelifa for helping me in navigating some of the most difficult periods of the PhD.

I wish to also acknowledge all of the Photonics Lab Crew that made the past four years an amazing experience, even outside of the lab. To Lukas go my compliments for having put together such an amazing team! My thanks go to (in no particular order):

- *The Late Lunch Gang*TM, with Jialiang, Yang, and Lujun Wang, for keeping the lunches always interesting (and at hours acceptable for southern-European metabolisms);
- the *FitLab* > 9000 sports group, with Johannes Piotrowski, Louisiane Devaud, Fabien Dorey and Jonas Ziegler, which many times became the Champions League/rugby/pizza group. Thank you for the fun evenings!
- Moritz Cavigelli and Barbara Schirmer, always ready to offer advice on Swiss bureaucracy-related doubts;
- all the colleagues with whom I crossed paths in the last four years: Sebastian Busschaert, Maciej Dziewiecki, Lysander Huberich, Achint Jain, Anna Kuzmina, Antti Moilanen, Alfonso Nardi, Pietro Tassan, Cla Duri Tschannen, Lea Wallimann. Thank you guys for sharing a game of kicker with me, or having a chat in front of raclette!

Dulcis in fundo, let me express my gratitude for the two men without whom this journey would have never been completed. I thank my brother Fra, and my boyfriend Leo, for their precious and patient support along the way.

Gratzias a totus!

Contents

Acknowledgements	i
Abstract	ix
Sinossi	xi
Introduction	1
1 Quantum control of a levitated nanoparticle	7
1.1 Trapping a dipolar scatterer inside a cryostat	9
1.1.1 Cryogenic setup	11
1.1.2 Optical detection	13
1.1.3 Characterization of the nanoparticle's shape	14
1.1.4 Parametric particle stabilization	16
1.1.5 Data acquisition and postprocessing	16
1.2 Feedback cooling to the ground state	18
1.2.1 Cold damping electronic filter characterization	18
1.3 Quantum ground state	19
1.3.1 Sideband thermometry	20
1.3.2 Cross-correlations between Stokes and anti-Stokes sidebands	23
1.4 Estimation of the measurement efficiency	24
1.5 Conclusions	26

2	Free evolution of a thermal state	29
2.1	Protocol for repeatable free evolutions	31
2.1.1	Langevin equation: free fall of an object surrounded by gas	32
2.1.2	General conditions for recapture after the free fall	35
2.1.3	Recapture probability	37
2.1.4	Expected energy at recapture	40
2.2	The setup	44
2.2.1	Creating a steerable trapping beam	45
2.2.1.1	Estimation of the trap displacement	46
2.2.2	Discharging the particle	47
2.2.3	Detecting the particle's dynamics	48
2.2.3.1	Calibrating the signal to displacement units	49
2.2.4	Cooling the particle's motion	51
2.3	Free fall of a nanoparticle	54
2.3.1	Measuring protocol	54
2.3.2	Free fall and recapture between overlapped foci	56
2.3.3	Free fall between separated tweezers	56
2.3.4	Along z and x	61
2.4	Phase space reconstruction	63
2.4.1	Extracting phase and amplitude from the data	64
2.4.2	Phase space reconstruction after the free evolution	67
2.5	State expansion as a function of free evolution time	70
2.6	On the scalability of the setup	73
2.7	Conclusions	75
3	Levitated optomechanics for coherent state expansion	77
	Appendices	81
A	Design of the mechanical components	81
B	Detailed solution to the Langevin Equation	86
C	Stabilization of the optical trap depth	91
D	Notation	93

E Abbreviations	98
References	101
List of Publications	107
Curriculum Vitae	109

Contents

Abstract

Recent experimental breakthroughs [1–4] have brought levitated optomechanics under the limelight as a compelling candidate for probing the laws of Nature at the interface between classical and quantum mechanics. Particularly ambitious proposals envision the use of massive microparticles for the preparation of large delocalized states, on scales comparable to the particles’ size [5].

The use of a levitated system, relying on the engineering of electromagnetic fields for the confinement and control of macroscopic objects in vacuum, is promising in all of those protocols that require highly tunable confining potentials, and low coupling to the surrounding environment [6].

With this work, we address two fundamental requirements for the realization of delocalized states with large objects, namely how to initialize their center-of-mass modes in a pure state, and how to implement a reliable protocol to generate a coherent delocalization of the wave function.

Our main probing tool is a femtogram silica nanoparticle composed by several billions of atoms, levitated in a harmonic optical trap.

We first study how to carefully control the center-of-mass motion of an electrically charged 100 nm nanoparticle below single mean phonon occupation. We suppress excess decoherence by working in a cryogenic environment, and rely on a highly efficient interferometric measurement of the particle’s motion to create a linear electric feedback to damp the center-of-mass energy to the quantum ground state.

We then move to a room-temperature system, and experimentally realize controlled and repeatable free evolutions of a free falling neutral nanoparticle prepared in a thermal state. We engineer a steerable intermittent trap to actuate a release-recapture protocol, completely freeing the nanoparticle from any confining potential for up to $270\ \mu\text{s}$, and across distances over $350\ \text{nm}$, more than three times its size. We steer the recapture tweezer to overlap its center with the position of the falling nanoparticle at the moment of recapture, and use it to verify a two-hundred-fold expansions of the thermal state's probability distribution in space.

Lastly, we discuss the possibility of merging the two experiments together, to achieve a nanometer-scale delocalization of the center-of-mass wave function of a levitated nanoparticle.

Sinossi

Recenti innovazioni sperimentali [1–4] hanno portato la levitazione optomeccanica sotto i riflettori come candidata promettente per sondare le leggi della Natura all’interfaccia tra la meccanica classica e quantistica. Alcune proposte particolarmente ambiziose immaginano l’utilizzo di microparticelle di massa non trascurabile per la preparazione di stati delocalizzati su grande scala, di dimensioni comparabili a quelle delle particelle stesse [5].

L’utilizzo di un sistema in levitazione, basato sulla manipolazione di campi elettromagnetici per il confinamento e il controllo di oggetti macroscopici nel vuoto, è promettente per tutti quei protocolli sperimentali che richiedono potenziali confinanti altamente controllabili, e un basso accoppiamento tra l’oggetto intrappolato e l’ambiente circostante [6].

Con questo lavoro di ricerca, rispondiamo a due requisiti fondamentali per la realizzazione di stati delocalizzati su grande scala, in particolare l’inizializzazione dei modi del centro di massa in uno stato quantistico puro, e l’implementazione di un protocollo affidabile per la realizzazione di una delocalizzazione coerente della funzione d’onda.

Il nostro strumento d’investigazione principale è una nanoparticella di silice dalla massa di un femtogrammo e composta da miliardi di atomi, levitata in una trappola armonica ottica.

Per prima cosa investighiamo come controllare il moto del centro di massa di una nanoparticella elettricamente carica, del diametro di 100 nm, per portare l’occupazione fononica media sotto l’unità.

Sopprimiamo la decoerenza in eccesso lavorando in ambiente criogenico, e sfruttiamo una misura interferometrica ad alta efficienza del moto della particella per creare una forza con cui dissipare l'energia del centro di massa fino a raggiungere lo stato fondamentale.

Ci spostiamo poi a temperatura ambiente, e realizziamo sperimentalmente, in maniera ripetibile e controllabile, l'evoluzione libera di uno stato termalizzato preparato a partire da una nanoparticella neutra in caduta libera.

Progettiamo una trappola ottica intermittente e pilotabile per attuare un protocollo di rilascio-ricattura, liberando completamente la nanoparticella da qualunque potenziale confinante fino a $270 \mu\text{s}$, e per distanze di caduta oltre i 350 nm , di tre volte più grandi della dimensione della particella.

Muoviamo la trappola in modo da sovrapporla alla particella in caduta al momento di ricattura, e la usiamo per verificare un'espansione della probabilità di distribuzione nello spazio dello stato termalizzato di oltre duecento volte.

Infine, discutiamo la possibilità di unire i due esperimenti, per ottenere una delocalizzazione su scala nanometrica della funzione d'onda del centro di massa di una nanoparticella levitata.

Introduction

Tests of quantum mechanics with massive objects represent one of Nature's most fascinating challenges. A particularly exciting idea is the realization of large superposition states with micrometer-sized particles, with masses in the range of 10^9 AMU to 10^{12} AMU, delocalizing their wave functions over distances on the micrometer scale [5]. This is akin to reproducing Young's double-slit experiment, but with the added complexity of dealing with objects composed by several billions of atoms.

The key ingredients for reaching this goal are the following:

- the ability to prepare a pure state with a massive object;
- a coherent evolution, to preserve the purity of the state during expansion;
- a "double slit", meaning a nonlinear interaction to create the superposition;
- a way to detect the fringes arising from the interference of the two superposed states.

A mechanical oscillator with mass m and eigenfrequency Ω in its quantum ground state will be localized in space over its zero-point-fluctuation $q_{\text{zpf}} = \sqrt{\hbar/(2m\Omega)}$. For femtogram masses and 100 kHz eigenfrequencies, we calculate $q_{\text{zpf}} \sim 10$ pm. One possibility to create a big delocalized state is thus to remove the confining potential, to allow for the state's free expansion [7].

The fulfilment of all of these conditions requires a system capable of delivering high levels of control over mechanical motion for state preparation, excellent decoupling from the environment to ensure long coherence times, and a high tunability of the confining potentials.

Our optically levitated nanoparticles in ultrahigh vacuum offer a platform combining an extreme degree of environmental isolation with a fully controllable trap potential. Because of this, they are an attractive candidate for experiments at the interface between classical and quantum physics [6].

In levitated optomechanics the oscillators are not tethered, but rather held by fields, either optical, electrical or magnetic. In such systems the oscillator is trapped in a confining volume where it experiences a restoring force. The trapping potentials are usually Gaussian-shaped, but for small oscillation amplitudes the dynamics of the trapped objects are well described by harmonic motion [8, 9]. The eigenfrequencies of the center-of-mass (COM) oscillations along the three axes of motion depend on the characteristics of the trapping field and the trapped object, and range from a few hertz to several kilohertz [6].

Here, we use a optically levitated femtogram nanoparticle as our main tool to approach the first two challenges on the road towards large superposition states.

In the first part of this work, we show how we exert quantum control over the motional degrees of freedom of a 100 nm nanoparticle ($> 10^9$ AMU) levitated in an optical trap.

Quantum control has already been achieved with tethered mechanical oscillators embedded in optical resonators [10–14]. The use of an optical cavity to enhance the optomechanical interaction constrains the bandwidth at which the system can operate. Moreover, the non tunable restoring force (due to the physical clamping) limits the range of expansion of the oscillator's wave function.

To overcome such restrictions, our experiments are carried out in a free space system, where the optical trap is created by strongly focusing a laser beam through an aspheric lens.

Two requirements need to be satisfied to reach quantum control over the

mechanical motion of the nanoparticle [15].

Firstly, we need to work in the backaction limited regime, meaning that the dominant noise contribution to our measurement is photon recoil from the measurement itself, and all excess noise sources (gas damping, vibrations, etc.) are suppressed.

Secondly, the optical readout of the nanoparticle's position must be shot-noise limited, and the overall measurement efficiency η_{meas} must be higher than 11%. This represents the minimum threshold to reach average phonon occupations \bar{n} lower than unity, according to the relation $\bar{n} = (1/\sqrt{\eta_{\text{meas}}} - 1)/2$.

With our research, we demonstrate how we exploit a highly efficient interferometric measurement ($\eta_{\text{meas}} = 24\%$) to generate an electric feedback force to damp the oscillations of an electrically charged femtogram nanosphere. We place the setup inside a cryostat, to suppress decoherence due to gas interactions and blackbody radiation. Working at the backaction limited regime, we reduce the nanoparticle's COM energy close to its quantum ground state, with a mean residual population of 0.65 phonons, and a purity of 43%.

Our result represents a milestone for the levitodynamics community, as it is one of the earliest examples [4] of extreme control reached on a femtogram mass's motion in a free-space system.

In the second part of this work we engineer a reliable protocol to generate a coherent delocalization of the COM wave function of a nanoparticle.

We mentioned how the presence of a restoring force limits the maximum achievable state expansion. Our strategy is hence to perform free state evolutions by completely shutting off the optical trap.

The implementation of this idea is not trivial: without the confining potential the nanoparticle is accelerated by external forces (due to stray electric fields, gravity etc.) and quickly falls out of the trapping volume.

State expansion protocols based on free evolution are routinely performed in cold atom experiments [7, 16], and with molecular beams [17]. However, when working with nanoparticles one cannot rely on a reservoir from which to draw identical samples for each experiment realization. We thus need to engineer a system to reliably "recycle" the same particle for multiple iterations,

while still achieving long evolution times.

In one of our standard platforms, based on a single fixed optical tweezer with waist $w \sim 1 \mu\text{m}$, up to now the action of gravitational acceleration has limited the maximum achievable free fall time to $140 \mu\text{s}$ [18]. Suggested protocols thus prescribe carrying out the experiments in microgravity, using free falling elevators [16], or by launching full setups in space [19].

Coming back to Earth, another approach envisions the use of hybrid traps, meaning a combination of optical and radio-frequency (RF) traps [20]. These systems rely on the nanoparticle's net electrical charge to keep it confined in the shallower "dark" electric potential during the state evolution, in absence of optical tweezer. The drawback is of course that the RF potential, although shallow, still limits the achievable state expansion [21]. Moreover, the presence of stray electric fields strongly impacts the success rate of the experiment [22], and further limits the achievable evolution times.

Instead of simply accepting the antagonistic role of gravity, here we show how we work around it, through the use of a steerable intermittent tweezer. We shut off the trapping beam to completely free a neutral nanoparticle from any confining potential, and then vertically shift the position of the trap focus to overlap it with the trajectory of the free falling particle, and ensure its recapture.

We experimentally prove that through control of the position of the tweezer, we realize repeatable free falling experiments on the same nanoparticle, over a wide range of distances and free evolution times. Here we test the protocols with a thermal state, verifying its expansion by a factor of two hundred, from 0.51 nm up to 115 nm .

Our experiment provides a reliable and controllable tool for the realization of true free evolutions, towards the objective of achieving large delocalized states with a femtogram levitated nanoparticle, starting from its quantum ground state.

This introduction is partially based on the publication [3].

Outline of this thesis

This work is structured as follows.

In Chapter 1 we delve in the description of how to obtain quantum control of the COM motion of a 100 nm silica nanoparticle, and reach a mean phonon occupation below unity. We first discuss the setup, and the importance of working in a cryogenic environment with a shot-noise limited detection scheme. Lastly, we describe how to measure the mean phonon population, and present our experimental results.

In Chapter 2 we present our novel platform for the realization of repeatable free evolutions with a 120 nm silica nanoparticle. We first study the phenomena governing the motion of the falling nanoparticle, to better understand its dynamics during the free evolution. Then, we describe the on/off and steering mechanism that controls power and position of the tweezer. Lastly, we test the protocol at room temperature, demonstrating a thermal state expansion of a factor >200 between tweezers displaced over distances wider than the size of the particle itself.

1

Quantum control of a levitated nanoparticle

This chapter is based on the publication

F. Tebbenjohanns¹, M. L. Mattana¹, M. Rossi¹, M. Frimmer, and L. Novotny, *Quantum control of a nanoparticle optically levitated in cryogenic free space*, *Nature* **565**, 378 (2021), doi: 10.1038/s41586-021-03617-w, URL <https://www.nature.com/articles/s41586-021-03617-w>.

A prerequisite for investigating quantum effects with a macroscopic object is to prepare it in a quantum mechanically pure state, such as its motional ground state. To this end, a great effort has been made in recent years towards the realization of cavity-mediated ground state cooling of the center-of-mass motion of a levitated particle [1, 2, 23–25].

Borrowing techniques developed for tethered optomechanical systems [14, 26–28], a possible approach to purify the particle’s motional state relies on an active, measurement-based feedback which does not necessitate the aid of an optical resonator, but nevertheless achieves single digit phonon occupations [29]. Such cavity-free optomechanical systems are unrestricted by the limitations

¹These authors contributed equally

regarding bandwidth, stability, and mode-matching associated with an optical resonator.

Operating these techniques in the quantum regime relies on performing measurements whose quantum backaction represents the dominant disturbance of the system [30, 31], and also on high detection efficiency to compensate the measurement backaction with the feedback system [14, 28, 32]. Furthermore, one should take care of eliminating possible sources of decoherence, like collisions with gas molecules and recoil from blackbody photons [5, 33]. In this context, the use of a cryogenic environment is particularly beneficial, providing at the same time the required extreme high vacuum and the sufficiently low thermal population of the electromagnetic continuum.

In this work, we optically levitate a nanoparticle in a cryogenic environment, which renders decoherence due to gas collisions negligible. We exploit a highly efficient quantum measurement of the particle's position and exert quantum control over its dynamics. This is achieved through a free space feedback cooling technique which relies on an optical measurement of the particle's position that approaches the minimum of the Heisenberg relation to within a factor of two. We use the measurement-based feedback to cool the particle's center-of-mass motion to an average occupancy of 0.65 motional quanta, corresponding to a state purity of 43%.

The absence of an optical resonator and its bandwidth limitations holds promise to transfer the full quantum control available for electromagnetic fields to a mechanical system. Together with the fact that the optical trapping potential is highly controllable, our experimental platform offers a route to investigating quantum mechanics at macroscopic scales [34].

In this chapter we will give a detailed overview of the setup and cooling feedback mechanism, before discussing the main experimental achievements.

1.1 Trapping a dipolar scatterer inside a cryostat

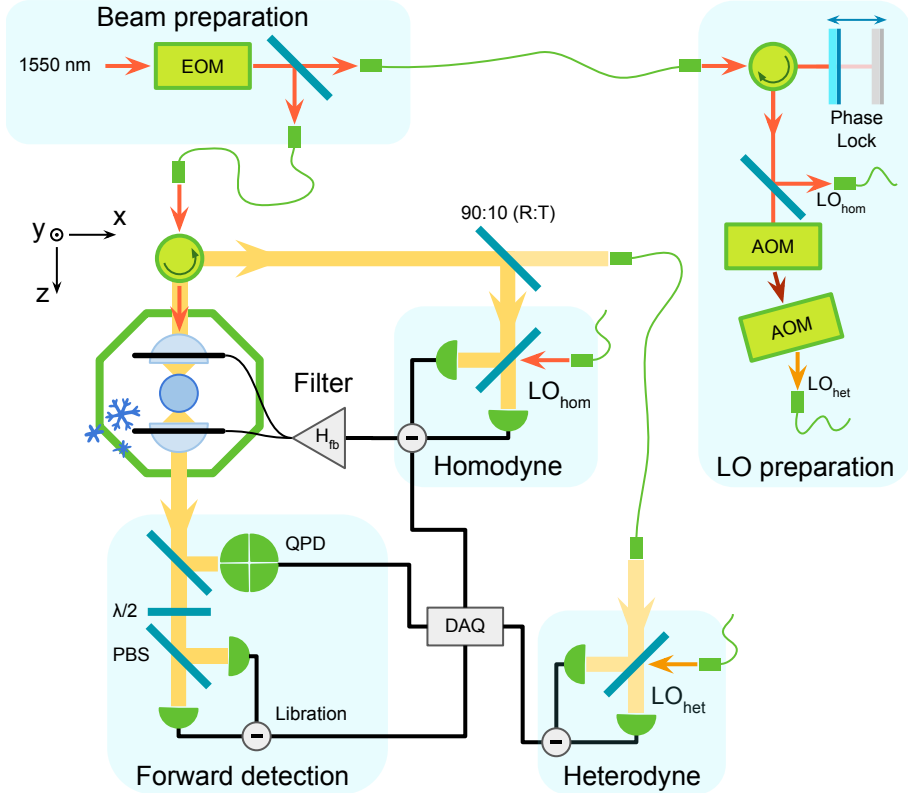


Figure 1.1: Schematic view of the setup. We optically trap a nanoparticle inside a cryogenic vacuum chamber using a telecom laser. In the forward direction, we employ a libration and position detection system. In the backward direction, we place both a homodyne and a heterodyne photodetector. AOM: acousto-optic modulator. DAQ: data acquisition card. EOM: electro-optic modulator. $\lambda/2$: half-wave plate. LO: local oscillator. PBS: polarizing beam-splitter. R: reflection. T: transmission.

In Fig. 1.1 we show our experimental system. We trap a dipolar dielectric scatterer in the focus of a linearly polarized laser beam, where it experiences a three-dimensional confining potential. For small displacements of the object from the focal center, the potential can be described as harmonic. The trap is generated by a single-beam laser (power $P_t \approx 1.2$ W, wavelength $\lambda = 1550$ nm, linearly polarized along the x axis) strongly focused through an aspheric trapping lens (numerical aperture 0.75).

Our dipolar scatterer is a single spherical silica nanoparticle of 100 nm

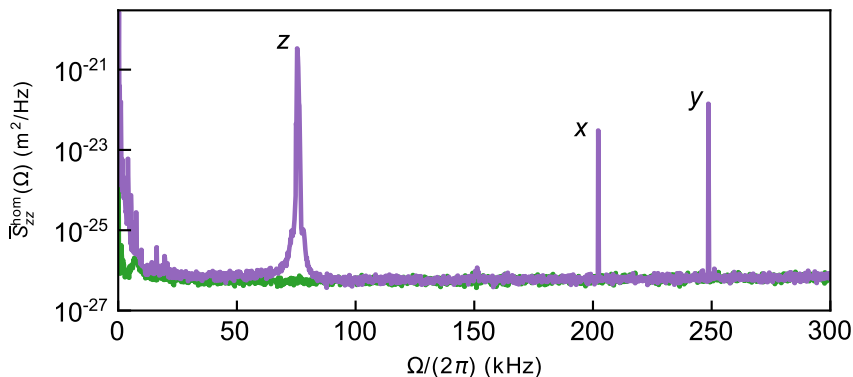


Figure 1.2: Power spectral density of the parametrically pre-cooled center-of-mass oscillation modes (purple) along the z , x , and y axis (at 77 kHz, 202 kHz, and 249 kHz, respectively). The information on the particle’s position along the z axis is predominantly encoded in the phase of the light scattered back into the trapping lens [35], while the information on the x and the y modes is equally distributed along the positive and the negative axis of propagation of the laser. As a result, by collecting the light backscattered by the particle, the detection efficiency is higher for the z mode, while we lose at least half of the information on the x and y modes, thus reducing their signal-to-noise ratio.

diameter, and a mass of about 1 fg. The resonance frequency of the particle’s COM motion along the optical axis z is $\Omega_z/(2\pi) = 77.6$ kHz (see Fig. 1.2). The resonance frequencies in the focal plane are $\Omega_x/(2\pi) = 202$ kHz along the polarization axis, and $\Omega_y/(2\pi) = 249$ kHz perpendicular to it.

To stabilize the particle inside the trap and to avoid nonlinearities of the trapping potential, we pre-cool the particle’s motion in the three dimensions using optical parametric feedback [36]. Throughout this chapter, we will focus our attention on the motion along the optical z axis.

The silica nanoparticle has a net charge, which we exploit to deliver a stronger electrical feedback to exert quantum control on the z COM mode.

We operate our optical trap inside a commercial 4 K closed-cycle cryostat, and take advantage of the cryogenic pumping effect to work in ultra-high vacuum conditions without the need for a bake-out. An ionization gauge located in the outer chamber (at 295 K) of the cryostat reads a pressure of 3×10^{-9} mbar, which we treat as an upper bound for the pressure at the location of the particle.

Our main goal with this setup's design is to obtain the highest possible efficiency for the interferometric measurement with which we evaluate the position of the particle. In fact, our detection of the particle's motion relies on the fact that the information on its position along the z axis is predominantly encoded in the phase of the light scattered back into the trapping lens [35]. We use an optical circulator to direct this backscattered light to our detection setup, where 90% (10%) of the signal is sent to a homodyne (heterodyne) receiver. These receivers convert the phase of the optical field into an electrical signal. We use the homodyne measurement for feedback-control, and the heterodyne signal for an independent out-of-loop measurement of the particle's motion.

We opted for a modular design, building the different stages of beam preparation, trapping, and detection on separated and self-contained breadboards, connected via optical fibers. Each block is designed to be as much as possible independent from the rest, which makes the setup more adaptable.

In the following sections we give a detailed overview of the core components of the setup.

1.1.1 Cryogenic setup

The imprecision on the measurement of the particle's position is affected by the fluctuating force $\overline{S}_{FF}^{\text{tot}} \propto T_{\text{gas}} P_{\text{gas}}$ arising from the interactions with the gas particles inside the vacuum chamber at temperature T_{gas} and pressure P_{gas} .

We optically trap the nanoparticles inside a vacuum chamber connected to a closed-cycle cryostat² to lower both the temperature and the pressure of the gas around the particle, thus reducing the fluctuating force disturbing its motion.

The optical tweezers are formed by focusing a linearly polarized laser³. We use an asymmetric lens system, with a 0.75 NA trapping lens⁴, with clear aperture $CA = 0.79$ mm, and a 0.6 NA collection lens⁵ ($CA = 5.2$ mm) to

²attocube attoDRY800, nominal cold-plate temperature 4 K

³NKT Photonics Koheras Adjustik E15, amplified by a NKT Photonics Koheras Boostik

⁴LightPath 355617

⁵Lightpath 355330

collimate the beam after the trap. The larger clear aperture of the output lens simplifies its alignment to the axis of the trapping lens, ensuring a good collimation of the light even in presence of small tilts between the surfaces of the two lenses. Nevertheless, due to the NA mismatch, about 25% of the light does not exit the trapping volume and is at least partly absorbed by the cryostat, increasing the temperature of the volume around the trap, next to which we measure a temperature of ~ 57 K.

The lenses are encased in a threaded steel mount, and screwed into a threaded holder machined out of electrically insulating polyether ether ketone (PEEK). The PEEK holder is mounted on top of a solid copper post in thermal contact with the cold plate of the cryostat. Although the use of PEEK limits the efficiency of the thermal contact between the cold plate and the trap assembly, its insulating properties are a necessity when performing linear feedback cooling. In fact, we control the particle's motion through Coulomb forces, taking advantage of the nanoparticle's net charge. The feedback can thus be applied directly on the lenses' metal mounts [37, 38], since they sit very close to the particle, and are electrically insulated from each other by the PEEK coupler.

The main effect through which we reduce the impact of the fluctuating force on the particle is by limiting the amount of hot gas molecules in its surroundings. To this end, we installed two concentric metallic cylinders inside the vacuum chamber, each of them connected to one of the two cold stages of the cryostat. Additionally to screening from blackbody radiation from the external surfaces of the chamber at room temperature, another one of their purposes is to also shield the innermost trapping volume from hot gas particles in thermal equilibrium with the vacuum chamber. The outer cylinder made of aluminium is thermally connected to the first stage of the cryostat, with a nominal temperature of 40 K. The inner shield, made of oxygen-free copper, contains the trapping assembly and is in thermal contact with the cold plate of the cryostat (nominal temperature 4 K).

More details on the design and fabrication of the components installed inside the vacuum chamber are available in Appendix A.

1.1.2 Optical detection

We use four photodetectors to characterize, stabilize, and localize the particle in the optical trap.

First, in the forward direction, we make use of a quadrant photodetector⁶ (QPD) and a polarisation sensitive libration detector⁷. We exploit their signals in the characterisation procedure of the particle as detailed below.

Second, we do homodyne and heterodyne detection on the field scattered by the particle back into the trapping lens. We employ a combination of a Faraday rotator and a polarizing beamsplitter to deflect the backscattered field from the forward direction. We derive our feedback signal for cold damping of the particle motion from a balanced, homodyne detector⁸, for which the backscattered light is mixed with a local oscillator (LO) beam whose phase we control with a piezo mirror. This is done to counteract the effect of slow drifts of the interferometer arms' length due to temperature fluctuations in the room, and to keep the phase of the LO locked to a difference of $\pi/2$ with respect to the backscattered light. This ensures our detection of the backscattered light is optimally phase-sensitive.

To maximize the detection efficiency, it is essential to properly overlap the signal beam (which has a dipolar scattering pattern collimated by the trapping lens) and the local oscillator, which has a Gaussian mode shape. To this end, we adjust the beam size of the local oscillator with a telescope and carefully tune the propagation distance of signal and reference beam to the detector.

To perform the out-of-loop analysis and sideband thermometry, we use a fiber-coupled balanced heterodyne detector⁹. Here, the LO beam is frequency shifted using two acousto-optic modulators¹⁰. The first AOM downshifts the laser frequency by 80 MHz, while the second upshifts it by 81 MHz (79 MHz) to blueshift (redshift) the LO by $\Omega_{\text{rf}}/(2\pi) = 1$ MHz. The resulting detuned LO beam is mixed with the signal in a 50:50 fiber coupler.

⁶Thorlabs PDQ30C

⁷homemade balanced detector

⁸Thorlabs PDB210C, quantum efficiency 0.88 at 1550 nm

⁹Newport 2117-FC-M

¹⁰Gooch&Housego 3080-1912

Detection noise characterization

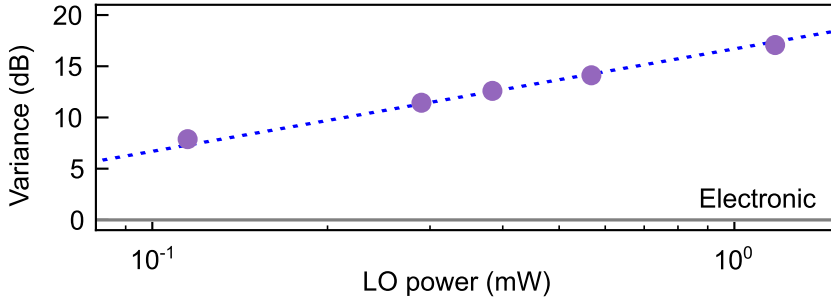


Figure 1.3: Variance of the laser noise as a function of local oscillator power in homodyne detection. The variance, expressed in dB, is normalized to the variance of the electronic noise floor of the detector (grey). The dotted blue line provides a guide for the eyes for the linear dependence between variance and power of the beam.

For feedback-based ground-state cooling, it is critical that our in-loop, homodyne detection noise is limited by the shot noise of the optical field. In Fig. 1.3 we show the measured noise power on the homodyne detector when only the LO beam is switched on (and the particle signal is blocked) as a function of the LO power. The noise power is obtained by integrating the measured PSD from 60 to 90 kHz and normalizing it by the detector electronic background-noise power (indicated by the grey line). The LO power is tuned by rotating a half-wave plate in front of a polarizer. We observe that the noise power increases linearly with the LO power, thus indicating that our detection is shot-noise limited. In the experiment, we operate at 560 μW of LO power, where the optical shot noise is 14 dB above the electronic noise floor.

1.1.3 Characterization of the nanoparticle’s shape

Our silica nanoparticles have a nominal diameter of 100 nm¹¹. They are provided in an aqueous solution, which we dilute in isopropanol and load into the optical trap with a nebulizer.

We work with single spherical nanoparticles, without rotational degrees of freedom, to eliminate the possibility of any coupling between the COM and

¹¹Nanocomposix

the rotational modes, which would disturb the experiment. To this end, we characterize the geometry of each trapped object to ensure it is isotropic.

In the following, we describe the two procedures we use for the characterization.

Damping rates of transverse motion

The first method consists in comparing the damping rate of the transverse x and y modes of oscillation, as we expect that spherical objects have equal damping rates along both axes [39].

At a pressure of a few mbar and at room temperature, we record a time trace of the x and y oscillation modes on our QPD placed in forward detection. Next, we estimate the PSDs from the time traces and fit them to a Lorentzian model. From the fit we extract the linewidths, and thus the damping rates, of the corresponding modes. Hence, we compute the ratio between the extracted damping rates and use it to identify spherical particles. Additionally, we estimate the size of the particle using the measured (absolute) damping rate at known pressure and temperature [40] (see also Section 2.2.3.1 for a detailed example). We perform this characterization at pressures ranging from 4 mbar to 8 mbar.

For the particle used in the particular realization of the experiment that we discuss in this chapter, we estimated a diameter of (106 ± 5) nm, and a ratio of the damping rates of 0.98 ± 0.04 .

Libration motion

A second characterization method is the detection of a libration motion of the trapped object. In a linearly polarized electromagnetic field, an anisotropic scatterer aligns itself to the polarization axis and oscillates around this equilibrium position. This libration motion is encoded in fluctuations of the polarization of the scattered light, which we measure using our polarization sensitive balanced photodetector in the forward direction [41]. If the scatterer is anisotropic, a libration mode is visible at frequencies between 400 kHz and 700 kHz [42, 43]. The particle used in the present work did not show any signature of a libration mode.

1.1.4 Parametric particle stabilization

Throughout our experiment, we stabilize the particle’s position along all three axes using parametric feedback cooling [36]. This reduction of the thermal motion suppresses any coupling of the three center-of-mass degrees of freedom (which can arise due to anharmonicities of the optical potential), leading to a three-dimensional, effectively harmonic trapping configuration with the eigenfrequencies Ω_x , Ω_y , and Ω_z .

We implement parametric feedback cooling using three phase-locked loops (PLLs), integrated in a lock-in amplifier¹². Each PLL generates an oscillating signal with constant amplitude and a fixed phase relation to the particle motion along one direction (x , y , or z). We feed the sum of all signals (oscillating at Ω_x , Ω_y , and Ω_z) to a digital squaring unit¹³, which effectively doubles the frequencies, and use this signal to modulate the intensity of the laser beam using an electro-optic modulator, thereby implementing ‘PLL-based feedback cooling’ [31]. We note that on top of the signals at twice the oscillation frequencies, our squaring unit also generates all sum and difference frequencies between the axes. These spurious signals do not affect the particle’s motion in practice since they are off resonant.

1.1.5 Data acquisition and postprocessing

We acquire both the homodyne and heterodyne detector signals by demodulating them at our frequencies of interest using lock-in amplifiers. The homodyne detector provides the signal which we use to actuate the linear feedback cooling (more details in Section 1.2), while the heterodyne is used to measure the temperature of the z COM mode through sideband asymmetry.

We demodulate our homodyne signal close to the eigenfrequency Ω_z , and denote the demodulated, complex-valued time trace by $i_{\text{hom}}[t]$. The square brackets indicate the discrete nature of the time trace. We furthermore demodulate our heterodyne signal close to the two sidebands generated by the particle’s motion around the LO frequency (acquired time traces $i_r[t]$ at $\Omega_{\text{rf}} - \Omega_z$ and $i_b[t]$ at $\Omega_{\text{rf}} + \Omega_z$), and at the LO frequency itself (acquired time trace $i_{\text{lo}}[t]$

¹²Zurich Instruments MFLI

¹³STEMLab Red Pitaya

at Ω_{rf}). We use 8th order demodulation filters with a 3 dB low-pass frequency of 5 kHz and a sample frequency of 53.57 kHz. For a typical experiment, we acquire 100-second-long demodulated time traces. In addition, we also acquire the homodyne detector signal at baseband ($i_{\text{dc}}[t]$), which we use both for locking our interferometer with a PI loop integrated into the MFLI and to aid in the postprocessing of the data, as described below.

Postselecting the data

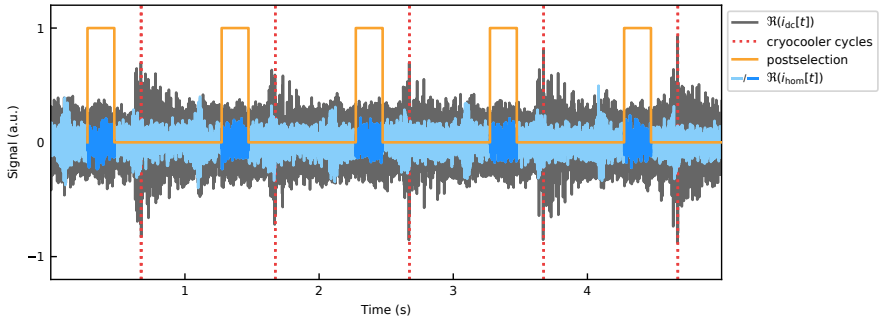


Figure 1.4: The compression cycles of the cryocooler are visible in our interferometric signal at baseband ($i_{\text{dc}}[t]$ in grey). We identify the cycles (red dotted lines) and postselect 300 ms long intervals (indicator function in orange) of the time traces containing the particle motion (exemplary for $i_{\text{hom}}[t]$ in blue).

Roughly every second the cryocooler compresses and expands the helium gas in the cold head, generating periodic mechanical vibrations on the optical table and the trap itself at ~ 1 Hz. These vibrations disturb both the interferometric read-out of the particle's position and its motion. In our recorded measurements, we hence postselect the time intervals in between the compression cycles.

In Fig. 1.4 we show an example of the homodyne detector signal at baseband ($i_{\text{dc}}[t]$, grey). We also show the real part of the particle's signal $i_{\text{hom}}[t]$ (blue). We identify the helium compression cycles from $i_{\text{dc}}[t]$ as burst signals with a repetition period of 1 s (marked as red dotted lines in Fig. 1.4). Finally, we postselect our demodulated time traces ($i_{\text{hom}}[t]$, $i_r[t]$, $i_b[t]$, and $i_{l0}[t]$) by choosing intervals of 300 ms duration at a fixed delay in between the bursts (indicated by the orange indicator function). We note that the interval length of

300 ms is much longer than any time scale of the particle motion.

1.2 Feedback cooling to the ground state

Our experimental platform is a cavity-free optomechanical system, performing a continuous measurement of the displacement of the particle [13, 44]. According to quantum theory, this measurement inevitably entails a backaction. For the levitated particle, this quantum backaction is associated with the radiation pressure shot noise arising from the quantization of the light field's linear momentum [31]. Importantly, with a sufficiently efficient detection system in place, it is possible to apply a feedback force to the particle that fully balances the effect of the backaction [14, 26, 32].

We use a feedback method termed *cold damping* [32]. In this scheme, a viscous feedback force is derived from the measurement signal, increasing the dissipation while adding a minimum amount of fluctuations. Our feedback circuit is a digital filter that electronically processes the homodyne signal in real-time. The filter mainly comprises a delay line to shift the phase of the frequencies near Ω_z by $\pi/2$. This procedure exploits the particle's harmonic motion to estimate the velocity from the measured displacement, and to first order acts as an optimal filter for a high-Q harmonic oscillator [45]. The filtered feedback signal is applied as a voltage to a pair of electrodes located near the nanoparticle. The particle is charged, and thus the feedback can be actuated via the Coulomb force [37].

1.2.1 Cold damping electronic filter characterization

Here we characterize the transfer function H_{fb} of the electronic feedback loop used to create the cold damping signal (see Fig. 1.1).

In Fig. 1.5 we plot the results of a network-analyzer measurement of the electronic components in the loop. Our designed digital filter contains several elements. First, we have a first-order high-pass filter with a 9 kHz cut-off frequency, which we use to remove any DC component to prevent saturation of the electronics. Second, we implement two digital 2nd-order notch filters

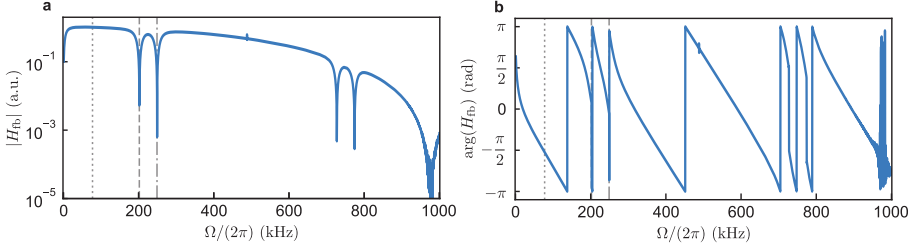


Figure 1.5: Measured magnitude (a) and phase (b) response of the experimentally used delay filter. The dotted, dashed, and dot-dashed vertical lines mark the location of the resonance frequency of motion along the z , x , and y axes, respectively.

at $\Omega_x/(2\pi) \approx 200$ kHz and $\Omega_y/(2\pi) \approx 250$ kHz with a quality factor of 5. This way we prevent the feedback from heating the transverse mechanical modes. We also observe two copies of such filters at around 750 kHz. This is due to aliasing of the signal during the frequency sweep measurements. In fact, the sampling rate is at ≈ 977 kHz, resulting in a Nyquist frequency of 488.5 kHz. Finally, we introduce a time delay such that at Ω_z the phase response is $-\pi/2$. Supposing that the phase contributions of the high-pass and the notch filters are negligible at Ω_z , one can tune the delay time such that $\Omega_z \tau = \pi/2 + 2\pi n$, where n is an integer. For any $n > 1$, the larger phase slope lowers the value of the feedback gain at which the closed-loop system becomes unstable, limiting the cooling performance. Therefore, we choose to implement the smallest possible time delay, which in our case is $\tau \approx 3.2$ μ s.

1.3 Quantum ground state

We now turn to the analysis of the particle's motional energy under feedback. In particular, in this work we extract the average phonon population of the z COM mode for different feedback gains, and corroborate our findings by comparing the results of two estimation methods based on the out-of-loop detection, namely sideband thermometry and sideband cross-correlation evaluation.

In the following section we will briefly discuss each technique, and demonstrate how an effective dissipation rate of $\gamma_{\text{eff}}/(2\pi) = 11.1$ kHz is the optimal one for ground-state cooling of our system.

1.3.1 Sideband thermometry

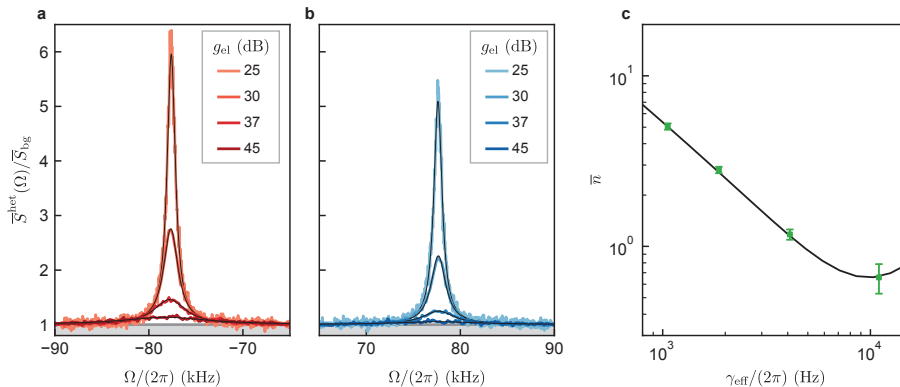


Figure 1.6: Stokes (a) and anti-Stokes (b) sidebands, at different electronic feedback gains, normalized to the estimated background level (grey line). Each sideband pair is simultaneously fitted to a theoretical model. c. Mechanical occupations (green squares) at different feedback gains. The black solid line is a theoretical model based on an ideal delay filter with parameters estimated from the in-loop spectra. The error bars are obtained by propagating the fit uncertainties (s.d.) of the areas.

The first method is Raman sideband thermometry [29, 46, 47]. Here, the ratio between the areas under the Stokes and anti-Stokes sidebands is used to extract the phonon population of the particle’s z COM mode. We note that the method of Raman thermometry does not rely on any calibration of the system. Instead, it is the zero-point energy of the oscillator which serves as the absolute scale all energies are measured against.

To resolve the Stokes and anti-Stokes sidebands from each other we analyze the signal recorded on the heterodyne receiver presented in Fig. 1.6, which provides an out-of-loop measurement of the motion of the particle [48]. The power spectral density (PSD) of both the red-shifted Stokes sidebands $\bar{S}_{rr}(\Omega)$ and of the blue-shifted anti-Stokes sidebands $\bar{S}_{bb}(\Omega)$ (Fig. 1.6a) shows a Lorentzian lineshape on top of a white noise floor. Importantly, the total noise power in the two sidebands is visibly different. From this sideband asymmetry,

we extract the phonon occupation by fitting our data to the expressions

$$\bar{S}_{rr}(\Omega) = \bar{S}_{\text{bg}}^r + R|\chi_{\text{eff}}(\Omega)|^2(\bar{n} + 1), \quad (1.1a)$$

$$\bar{S}_{bb}(\Omega) = \bar{S}_{\text{bg}}^b + R|\chi_{\text{eff}}(\Omega)|^2\bar{n}, \quad (1.1b)$$

with $\bar{S}_{\text{bg}}^{r,b}$ the spectral background floor, $R = m\gamma_{\text{eff}}\hbar\Omega_z/\pi$ a scaling factor, \hbar the reduced Planck constant, $\chi_{\text{eff}}(\Omega) = 1/[m(\Omega_z^2 - \Omega^2 - i\gamma_{\text{eff}}\Omega)]$ the effective mechanical susceptibility modified by the feedback, γ_{eff} the effective linewidth including the broadening due to feedback, and \bar{n} the average phonon occupation of the mechanical state. In the fit model, we allow the two sidebands to assume different force noise and background values, but we constrain them to have the same resonance frequency Ω_z , and linewidth γ_{eff} .

The fitted force-noise values are a direct measure of the enclosed area in the two sidebands. Thus, the occupation \bar{n} can be extracted according to

$$\frac{\bar{S}_{FF}^r}{\bar{S}_{FF}^b} = 1 + \frac{1}{\bar{n}}, \quad (1.2)$$

with $\bar{S}_{FF}^r = R|\chi_{\text{eff}}(\Omega)|^2(\bar{n} + 1)$, and $\bar{S}_{FF}^b = R|\chi_{\text{eff}}(\Omega)|^2\bar{n}$.

The uncertainties of these areas crucially depend on the precision of the background-noise estimation from the fitting routine, especially at the largest feedback gain where the signal-to-noise ratio becomes small. Another possible source of systematic error is a frequency-dependent response of the acquisition chain (photodetector and DAQ). To rule out this effect, we measure the motional sidebands both using a positive and a negative frequency for the heterodyne local oscillator $\omega_{\text{LO}} = \omega_L - \Omega_{\text{rf}}$, where ω_L is the frequency of the laser and $\Omega_{\text{rf}}/(2\pi) = \pm 1$ MHz denotes the frequency shift induced with the AOMs [29]. We then extract the phonon occupation according to

$$\bar{n} = \left(\sqrt{\frac{S_{FF}^{r,+} S_{FF}^{b,-}}{S_{FF}^{b,+} S_{FF}^{r,-}}} - 1 \right)^{-1}, \quad (1.3)$$

where the \pm superscripts stand for the sign of the LO frequency shift. Using this method, any frequency dependence of the transfer function of the measure-

ment chain is cancelled. In Fig. 1.6c, we show as green squares the phonon occupations estimated from the asymmetry of the measured heterodyne spectra. We also show as a black line the theoretical cooling model extracted from the analysis of the signals collected from our in-loop detector (the homodyne one, from which we derive the feedback). More details on the in-loop detection theory can be found in the supplementary information to the publication [3]. The error bars are obtained by propagating in Eq. (1.3) the fit uncertainties (s.d.) of the four areas extracted from the fits (two areas per each frequency of the local oscillator). The larger error bars for lower occupations reflect the reduced signal-to-noise ratio in the PSDs.

In Fig. 1.7a we plot the Stokes (in red) and anti-Stokes (in blue) sidebands measured at the largest electronic feedback gain $g_{\text{el}} = 45$ dB. From the fit of our data (solid lines in Fig. 1.7a), we extract a linewidth of $\gamma_{\text{eff}}/(2\pi) = 11.1$ kHz together with a residual occupation of $\bar{n} = 0.66 \pm 0.08$, corresponding to a ground-state occupancy of $1/(\bar{n} + 1) = 60\%$.

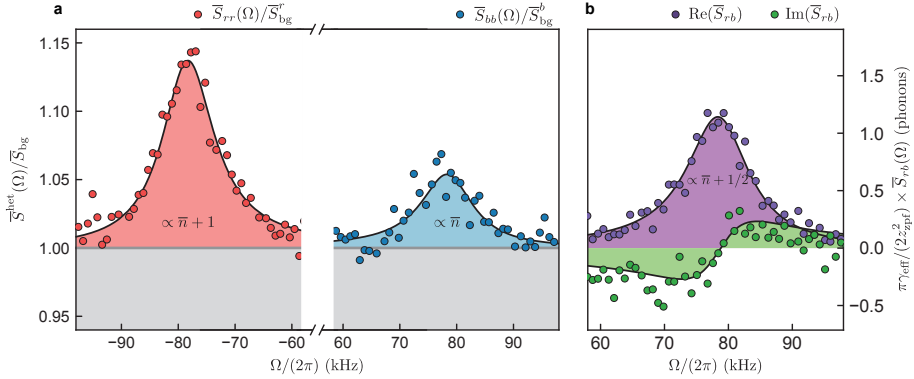


Figure 1.7: **a.** Stokes (red circles) and anti-Stokes (blue circles) sidebands measured by the out-of-loop heterodyne detector, at the largest electronic feedback gain. The black lines are fits to Eqs. (1.1), from which we extract the sideband powers. From their ratio, we extract a final occupation of $\bar{n} = 0.66 \pm 0.08$. **b.** Real (purple circles) and imaginary (green circles) parts of the cross-power spectral density between the Stokes and anti-Stokes sideband, together with theoretical fits (black lines). We calibrate the vertical axis using the imaginary part, and we extract a final occupation of $\bar{n} = 0.64 \pm 0.09$ from the real part.

1.3.2 Cross-correlations between Stokes and anti-Stokes sidebands

As mentioned in the previous section, the estimation of the spectral background floor $\bar{S}_{\text{bg}}^{r,b}$ heavily affects the uncertainties on the areas under the Stokes and anti-Stokes sidebands. The estimation of the occupation through analysis of the spectral cross-correlation between the two sidebands is instead robust against this possible source of error. The cross-PSD between these two sidebands can be expressed as [49]

$$\bar{S}_{rb}(\Omega) \propto \bar{S}_{zz}(\Omega) + \frac{i\hbar}{2\pi} \text{Re}\{\chi_{\text{eff}}(\Omega)\}, \quad (1.4)$$

which we simplify to [50]

$$\bar{S}_{rb}(\Omega) = R |\chi_{\text{eff}}(\Omega)|^2 \left(\bar{n} + \frac{1}{2} + \frac{i}{2} \frac{\Omega^2 - \Omega_z^2}{\gamma_{\text{eff}} \Omega_z} \right). \quad (1.5)$$

where R is a constant proportionality factor. Importantly, the imaginary part of the cross-correlation is independent of the phonon population \bar{n} . It arises purely from the zero-point fluctuations and can thus serve to calibrate the real part.

In Fig. 1.7b, we show the real part of the measured cross correlation $\text{Re}(S_{rb})$ (purple) and its imaginary part $\text{Im}(S_{rb})$ (green), fitted with Eq. 1.5. With this method we extract a phonon occupation of $\bar{n} = 0.64 \pm 0.09$, well in agreement with the value extracted from the sideband asymmetry. The error is obtained from the propagation of the uncertainties (s.d.) in the fitted parameters. More details on cross-correlation thermometry can be found in [49, 50] and in the supplementary information to [3].

Estimation of spectral densities.

In the following, we give some more details on how we compute the power spectral densities (PSDs) of the measured time traces.

We estimate the PSD of the acquired homodyne data according to

$$\bar{S}_{\text{hom}}[\Omega] = \langle |i_{\text{hom}}[\Omega]|^2 \rangle, \quad (1.6)$$

where $i_{\text{hom}}[\Omega]$ is the discrete Fourier transform (DFT) multiplied by \sqrt{T} (T being the total acquisition time of each realization) and $\langle \dots \rangle$ is the ensemble average over the different realizations.

In contrast to homodyne detection, the heterodyne detector's arm lengths are not actively stabilized, and we have to correct for phase drifts in postprocessing. These phase drifts are reflected in the phase of the demodulated LO frequency $i_{\text{lo}}[t]$. Since the frequency components of both motional sidebands have a definite phase relative to the LO, we can remove the drifts from the time traces by redefining $i_j[t] \rightarrow i_j[t]e^{-i\arg(i_{\text{lo}}[t])}$, where $j = r, b$. After this phase correction, we estimate the PSDs of each sideband as well as the cross-PSD between them as

$$\overline{S}_{rr}[\Omega] = \langle |i_r[-\Omega]|^2 \rangle, \quad (1.7)$$

$$\overline{S}_{bb}[\Omega] = \langle |i_b[\Omega]|^2 \rangle, \quad (1.8)$$

$$\overline{S}_{rb}[\Omega] = \langle i_r[-\Omega]i_b[\Omega] \rangle. \quad (1.9)$$

We note that the phase correction described above only affects the cross-PSD $\overline{S}_{rb}[\Omega]$.

1.4 Estimation of the measurement efficiency

Efficient quantum measurement is a prerequisite for stabilizing the levitated nanoparticle in its quantum ground state via feedback. In the following, we perform a detailed analysis of our measurement system. To this end, we analyze the measurement record of our in-loop homodyne receiver and derive the measurement efficiency η_{meas} , representing the amount of information gathered per disturbance incurred [15].

In Fig. 1.8a we show, in dark red, the homodyne spectrum acquired at the lowest feedback gain labelled by the set gain $g_{\text{el}} = 0$ dB ($\gamma_{\text{eff}} = 2\pi \times 21.9$ Hz). At such low gain, the measured fluctuations on resonance largely exceed the noise floor and the feedback solely leads to a broadening of the mechanical susceptibility. In this regime, the detection noise fed back as a force does not play any role, and can be safely ignored. We calibrate our in-loop measurement by performing sideband thermometry on the out-of-loop detector at a moderate

gain of $g_{\text{el}} = 25$ dB. Subsequently, we fit the calibrated in-loop spectrum to

$$\bar{S}_{zz}^{\text{hom}}(\Omega) = \bar{S}_{\text{imp}} + |\chi_{\text{eff}}(\Omega)|^2 \bar{S}_{FF}^{\text{tot}}, \quad (1.10)$$

where $\bar{S}_{FF}^{\text{tot}} = \hbar^2 \Gamma_{\text{tot}} / (2\pi z_{\text{zpf}}^2)$ is the total force noise PSD, $\bar{S}_{\text{imp}} = z_{\text{zpf}}^2 / (8\pi \Gamma_{\text{meas}})$ is the imprecision noise PSD of the detection, and $z_{\text{zpf}}^2 = \hbar / (2m\Omega_z)$ denotes the zero-point fluctuations of the oscillator. We note that these two spectral densities can be equivalently written in terms of a measurement rate $\Gamma_{\text{meas}} = \eta_d \Gamma_{\text{qba}}$ (with Γ_{qba} the decoherence rate due to the quantum backaction, and η_d the overall detection efficiency), and a total decoherence rate $\Gamma_{\text{tot}} = \Gamma_{\text{qba}} + \Gamma_{\text{exc}} = \gamma_{\text{eff}}(\bar{n} + 1/2)$ (with Γ_{exc} the decoherence rate in excess of quantum backaction). From the fit, we extract a measurement rate of $\Gamma_{\text{meas}} / (2\pi) = (1.33 \pm 0.04)$ kHz and a total decoherence rate of $\Gamma_{\text{tot}} / (2\pi) = (5.5 \pm 0.3)$ kHz. The measurement rate approaches the total decoherence rate, giving a measurement efficiency of $\eta_{\text{meas}} = \Gamma_{\text{meas}} / \Gamma_{\text{tot}} = 0.24 \pm 0.02$, which is bounded by $\eta_{\text{meas}} \leq 1$ according to the Heisenberg measurement-disturbance relation [15, 46]

Next, we characterize the role of the feedback gain in our system. To

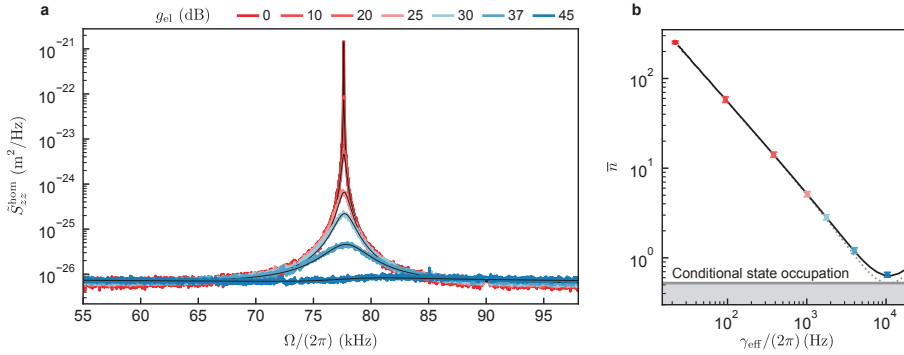


Figure 1.8: a. Single-sided displacement spectra measured by the in-loop homodyne detector at different electronic gains g_{el} . We exclude three narrow spectral features from the analysis. The black lines are fits to a theoretical model (see Methods to [3]). **b.** Mechanical occupations extracted from integrating the computed position and momentum spectra, which are based on parameters estimated from the in-loop spectra. The solid black line is a theoretical model assuming an ideal delay filter. The dotted grey line assumes ideal cold damping. The horizontal grey line corresponds to the occupation of the conditional state, stemming from the performed measurements. The error bars reflect the standard deviation (s.d.) in the fitted parameters, as well as the statistical error on the calibration method.

this end, we record homodyne spectra at increasing gain settings, as shown in Fig. 1.8a. For small gain values, the feedback only increases the mechanical linewidth. For high gain values, however, the spectra flatten and even dip below the imprecision noise, an effect known as *noise squashing* [26]. In this case, the feedback-induced correlations become dominant and increase the displacement fluctuations, rather than reducing them. Having characterized the transfer function of the electronic loop, we can fit each spectrum to a full in-loop model (see Methods in [3]). Then, we use the results of the fits to compute the effective linewidths and the phonon occupations, shown in Fig. 1.8b. At the highest gain, we estimate an occupation of $\bar{n} = (0.65 \pm 0.04)$, consistent with both other methods described previously. The good agreement between our three methods to extract the phonon occupation suggests that the contribution of classical laser noise to the sideband asymmetry is negligible [51].

Based on the estimated measurement and total decoherence rates, we calculate a theoretical model for the occupations under a pure delay filter (black line in Fig. 1.8b). For comparison, we show the theoretical results achievable under ideal cold damping [32] in the limit of $\gamma_{\text{eff}} \ll \Omega_z$ (dotted grey line). In this case, an induced linewidth of γ_{eff} corresponds to an occupation $\bar{n} = \Gamma_{\text{tot}}/\gamma_{\text{eff}} + \gamma_{\text{eff}}/(16\Gamma_{\text{meas}}) - 1/2$ [48], dependent only on the measurement and decoherence rates.

1.5 Conclusions

In summary, we have achieved quantum control over the motion of a levitated nanosphere. This control relies on the high reported measurement efficiency of 24%, comparable to what has been achieved with tethered micromechanical resonators [14], atomic systems [52], and superconducting circuits [53].

As an example of measurement-based quantum control, we have experimentally stabilized the nanoparticle’s motion in its quantum ground state via active feedback. The prepared quantum state has a residual occupation of $\bar{n} = 0.65$ phonons, corresponding to a purity of $1/(1 + 2\bar{n}) = 43\%$. Under optimal control, achievable by optimization of the feedback circuit, we expect to reach the same occupation as the conditional state [15], that is, $\bar{n}_{\text{cond}} \approx (1/\sqrt{\eta_{\text{meas}}} - 1)/2 = 0.5$ (see Fig. 1.8b). Our experiment approaches this limit to within 30%.

Notably, this is the first time that quantum control of mechanical degrees of freedom has been achieved without the use of an optical resonator. In a study conducted in parallel to ours, similar results have been achieved with an optimal-control approach [54].

Importantly, we conduct levitated-optomechanics experiments in a cryogenic environment for the first time. This represents a milestone towards the generation of genuine macroscopic quantum states of a nanosphere, which would require extremely low levels of decoherence [5].

2

Free evolution of a thermal state

There are two main ways of performing a coherent state expansion of the center-of-mass mode of an oscillator [55, 56].

One option is parametric amplification, in which the COM oscillation frequency is modulated in time. This approach has been realized in a variety of systems, both with charged and neutral objects [55, 57, 58]. Restricting ourselves to the domain of levitated nanoparticles, successful implementations of parametric amplification have been achieved by abruptly changing the oscillation eigenfrequency modulating the stiffness of the trap [21], to provide a strong confining potential for state preparation, and a shallower one for the state evolution. The shallow potential keeps the nanoparticle weakly confined in a volume later addressable by the optical tweezers for state verification, ensuring the same object can be used for multiple runs of the experiment. The disadvantage is that the confinement limits the maximum achievable state expansion, depending on the ratio of the eigenfrequencies of the oscillator in the two potentials [21, 58].

Another way to achieve coherent expansion is through free evolution, by releasing the state from any confining potentials. Such protocols have

already been successfully implemented with atoms and molecules, to reach delocalizations up to the meter scale [7, 16, 17].

In levitated systems, a truly free evolution is interesting because it eliminates photon backaction from the optical trap. In addition, the state expansion would scale linearly in time, and be limited only by decoherence originating from background gas and blackbody radiation.

Nevertheless, the total absence of a trapping potential makes a charged nanoparticle particularly sensitive to stray electric fields, and to the gravitational pull. These forces accelerate the particle outside the trapping volume, and limit the maximum achievable evolution time. Therefore, earlier works towards free evolutions with nanoparticles were limited to free fall times of $140\ \mu\text{s}$ [59].

Here we pursue this promising second approach to state expansion using a nanoparticle with zero net electrical charge to avoid any influence from stray electric fields. Furthermore, we deal with the effect of gravitational acceleration by implementing a release-and-catch geometry with vertically shifting tweezers. The ability to move the recapturing trap and overlap it with the position of the free falling particle allows us to achieve free evolution times up to $270\ \mu\text{s}$, across distances of $350\ \text{nm}$, bigger than three times the particle's size.

We prepare a neutral $120\ \text{nm}$ nanoparticle in a thermal state, with root-mean-square oscillation amplitude of $0.51(7)\ \text{nm}$, and evaluate the state evolution through phase space reconstruction at recapture. For a free fall time of $250\ \mu\text{s}$, we observe an expansion of a factor $223(45)$, achieving a broadening of the position phase space distribution up to $115(16)\ \text{nm}$.

Importantly, our platform enables controllable and repeatable free evolution experiments with the same nanoparticle, over thousands of realizations.

In this chapter we present our protocol in detail. We study the equations that govern the dynamics of the particle during the free fall, and at recapture, and determine which parameters affect the controllability and repeatability of the protocol. We then give an overview of the setup, before presenting the experimental results.

2.1 Protocol for repeatable free evolutions

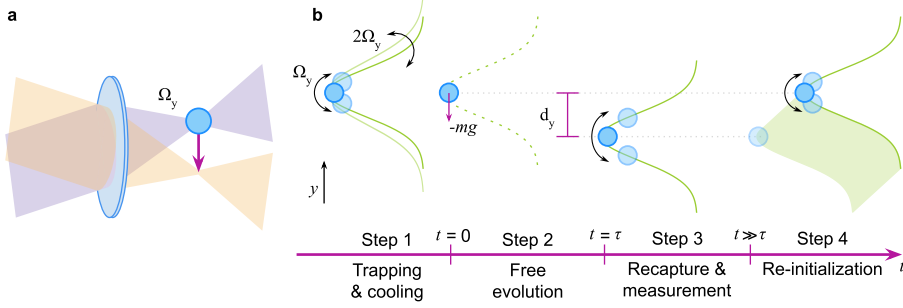


Figure 2.1: **a.** Illustration of the trap’s configuration along the vertical axis y . **b.** Free fall protocol. First, the COM mode is initialized in a thermal state. Then, the particle is released and let free fall for a time τ , after which it is recaptured in a trap sitting below the starting position. After studying its dynamics at recapture, the particle is brought back in the upwards position, for re-initialization.

The free fall protocol consists of four steps, represented in Fig. 2.1b.

- Step 1: the particle is confined in the optical trap and its COM motion is pre-cooled via parametric feedback along all axes.
- Step 2: at time $t = 0$ the feedback and the trap are switched off. The particle undergoes a free fall under the influence of gravitational acceleration.
- Step 3: at time $t = \tau$, the particle is recaptured by a displaced trap whose center is roughly aligned with the particle COM position after the free fall (see Section 2.1.2).
- Step 4: the trap is moved back in the initial release position, dragging the particle along so that it can be recycled to perform the experiment for several times.

The position of the particle is encoded in the phase of the scattered field. Between steps 3 and 4, after recapture in the optical trap, we read out the particle’s motion with a quadrant photodetector (QPD) placed in forward detection. From the QPD signal we can extract information on the evolution of the thermal state at the instant of recapture τ .

2.1.1 Langevin equation: free fall of an object surrounded by gas

In this section we address the main parameters influencing the dynamics during the free fall. We consider an initial thermal state with effective temperature $T_{i,0}$, undergoing a free fall in presence of residual gas, modelled as a thermal bath with temperature T_{gas} and pressure P_{gas} .

The thermal state is prepared through parametric cooling. Since the feedback is non-linear, we apply it with a very mild gain, to reduce the effect of the non-linearities induced in the potential, such that we can neglect them in our analysis. We thus assume that the COM behaves as a harmonic oscillator, and we describe it in phase space as a thermal state identified by Gaussian probability density distributions in position ($\mathcal{P}(q_i)$) and momentum ($\mathcal{P}(p_i)$). We want to determine how $\mathcal{P}(q_i)$ expands during the fall, by analyzing the evolution of its mean and variance. Finally, we determine the optimal recapture conditions to ensure a high repeatability of the experiment. In particular, we study how do $T_{i,0}$ and P_{gas} affect the probability of recapturing the nanoparticle.

The evolution of the system during step 2 is described by the Langevin equation

$$\ddot{\mathbf{q}} = -\gamma\dot{\mathbf{q}} - \nabla V(\mathbf{q}) + \boldsymbol{\eta}(t). \quad (2.1)$$

Here $\boldsymbol{\eta}(t) = F_{\text{fluct}}(t)/m$ is proportional to the fluctuating force originating from the interactions between the nanoparticle of mass m and the background gas. This stochastic parameter is a Gaussian white noise, with magnitude f given by the autocorrelation function $\langle \eta_i(t)\eta_i(t+t') \rangle = f\delta(t')$. The magnitude f is linked to the gas damping rate γ by the fluctuation-dissipation theorem, according to $f = 2\gamma k_B T_{\text{gas}}/m$ in one dimension [60].

During the free fall, the nanoparticle is subjected to the gravitational force $m\mathbf{g} = -\nabla V(\mathbf{q})$, with acceleration $\mathbf{g} = (g_x, g_y, g_z) = (0, -g, 0)$. The force acts only along the vertical axis y , and we assume that the magnitude of the gravitational acceleration $g \approx 9.81 \text{ m/s}^2$ stays constant during the fall.

From the Langevin equation we derive velocity and position of the object

in one dimension along the axis $i = x, y, z$:

$$v_i(t) = v_{i,0}e^{\gamma t} + \frac{g_i}{\gamma}(1 - e^{-\gamma t}) + \int_0^t e^{-\gamma(t-t')} \eta_i(t') dt', \quad (2.2)$$

$$q_i(t) = q_{i,0} + \frac{v_{i,0}}{\gamma} e^{-\gamma t} + \frac{g_i}{\gamma} t - \frac{g_i}{\gamma^2} (1 - e^{-\gamma t}) + \frac{1}{\gamma} \int_0^t (1 - e^{-\gamma(t-t')}) \eta_i(t') dt'. \quad (2.3)$$

Here $v_{i,0}$ and $q_{i,0}$ denote respectively velocity and position along axis i at time $t = 0$. The detailed derivation of our results can be found in Appendix B.

At $t = 0$, the COM modes of the nanoparticle are each represented by a thermal state characterized by an effective temperature $T_{i,0}$, related to the kinetic (K) and potential (U) energy of the mode according to

$$\begin{aligned} K + U &= k_B T_{i,0} \\ &= \frac{1}{2} m \left(\langle v_{i,0}^2 \rangle + \Omega_{i,0}^2 \langle q_{i,0}^2 \rangle \right) = k_B T_{i,0}, \end{aligned} \quad (2.4)$$

in which $\langle v_{i,0}^2 \rangle$ and $\langle q_{i,0}^2 \rangle$ are the second moments of velocity and position of the COM mode i , with $\Omega_{i,0}$ denoting its eigenfrequency.

For a given $T_{i,0}$, we define two probability density functions $\mathcal{P}(v_i)$ and $\mathcal{P}(q_i)$, which indicate the probability of finding the particle with velocity v and at position q along axis i . Because the COM behaves like a harmonic oscillator, the distributions are Gaussian, and are fully characterized by only two parameters: mean μ and variance σ^2 :

$$\mathcal{P}(X(t)) = \frac{1}{\sqrt{2\pi\sigma_X^2(t)}} e^{-\frac{(X-\mu_X(t))^2}{2\sigma_X^2(t)}}, \quad (2.5)$$

where we used the following definitions of mean $\mu_X(t)$ and variance $\sigma_X^2(t)$ of a variable X :

$$\mu_X(t) = \langle X(t) \rangle; \quad \sigma_X^2(t) = \langle X^2(t) \rangle - \langle X(t) \rangle^2, \quad (2.6)$$

with $\langle X^2(t) \rangle$ being the second moment of X .

From Eq. 2.2 and Eq. 2.3, we derive the mean and the variance of velocity

and displacement as a function of time (see Appendix B), thus also describing the evolution of the two Gaussian distributions $\mathcal{P}(v_i)$ and $\mathcal{P}(q_i)$.

For the initial conditions of the system, we assume that

- $\langle v_{i,0} \rangle = 0$; $\langle q_{i,0} \rangle = 0$ at equilibrium;
- $\langle v_{i,0}^2 \rangle = k_B T_{i,0} / m$; $\langle q_{i,0}^2 \rangle = k_B T_{i,0} / (\Omega_{i,0}^2 m)$ from the equipartition theorem, from which follows that $\langle v_{i,0}^2 \rangle = \Omega_{i,0}^2 \langle q_{i,0}^2 \rangle$.

We find

$$\mu_{v_i}(t) = \frac{g_i}{\gamma} (1 - e^{-\gamma t}); \quad (2.7)$$

$$\sigma_{v_i}^2(t) = \langle v_{i,0}^2 \rangle e^{-2\gamma t} + \frac{f}{2\gamma} (1 - e^{-2\gamma t}); \quad (2.8)$$

$$\mu_{q_i}(t) = \frac{g_i}{\gamma} t - \frac{g_i}{\gamma^2} (1 - e^{-\gamma t}); \quad (2.9)$$

$$\begin{aligned} \sigma_{q_i}^2(t) &= \langle q_{i,0}^2 \rangle + \frac{\langle v_{i,0}^2 \rangle}{\gamma^2} (1 - e^{-\gamma t})^2 \\ &+ \frac{f}{\gamma^2} t - \frac{f}{2\gamma^3} (3 - e^{-\gamma t})(1 - e^{-\gamma t}). \end{aligned} \quad (2.10)$$

When friction due to the background gas is negligible, the standard deviation of $\mathcal{P}(v_i)$ stays constant, while σ_{q_i} evolves linearly in time, for $\Omega_{i,0}^2 t^2 \gg 1$:

$$\lim_{\gamma \rightarrow 0} \sigma_{v_i}(t) = \sqrt{\langle v_{i,0}^2 \rangle}, \quad (2.11)$$

$$\lim_{\gamma \rightarrow 0} \sigma_{q_i}(t) = \sqrt{\langle q_{i,0}^2 \rangle (1 + \Omega_{i,0}^2 t^2)}, \quad (2.12)$$

The mean velocity and position of the nanoparticle evolve as expected in the case of uniform acceleration:

$$\lim_{\gamma \rightarrow 0} \mu_{v_i}(t) = g_i t. \quad (2.13)$$

$$\lim_{\gamma \rightarrow 0} \mu_{q_i}(t) = \frac{1}{2} g_i t^2. \quad (2.14)$$

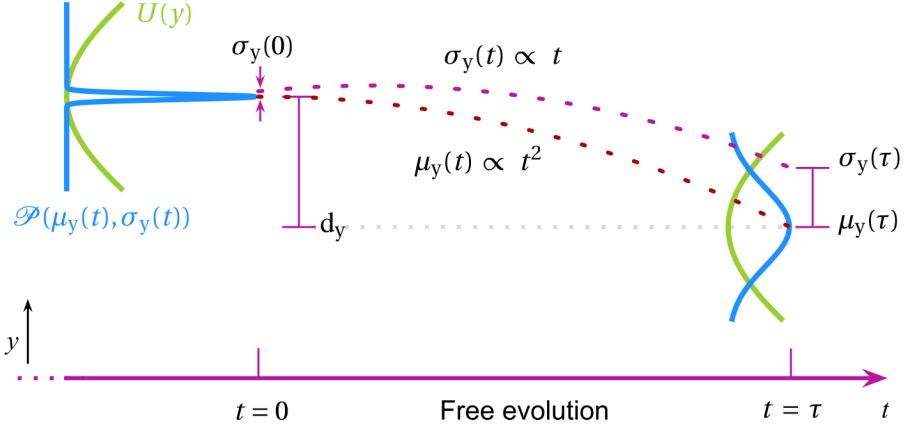


Figure 2.2: The particle's position along the vertical axis is represented by a Gaussian probability density $\mathcal{P}(q_y) = \mathcal{P}(\mu_y(t), \sigma_y(t))$, with mean μ_y and standard deviation σ_y that evolve during the free fall. For small gas damping σ_y increases linearly with time.

2.1.2 General conditions for recapture after the free fall

We now analyze which parameters determine the success of the recapture. Ideally, we want to turn on the recapturing trap when the particle is close to its center. We expect this minimizes the amplitude of the oscillatory motion, increasing the chances of keeping the particle in the new trap after the free fall.

Let's assume an extreme case of a free fall time of 1 ms. We consider a nanoparticle with diameter 143 nm (the nominal size indicated by the manufacturer), and a mass $m = 3.4$ fg. The conditions for recapture are:

- the kinetic energy at the recapture time $t = \tau$ must be less than the depth of the optical trap, which we estimate to be $U_0 \approx 50k_B T_{\text{gas}}$ [8];
- the particle must have a high probability of being located inside the trapping volume, delimited by the trap waist radius ω_i . We summarize this imposing $3\sigma_{q_i}(\tau) \ll \omega_i$.

The first condition implies that $\langle v_i^2(\tau) \rangle = \sigma_{v_i}^2(\tau) + \mu_{v_i}^2(\tau) < 2U_0/m \approx (35 \text{ cm s}^{-1})^2$, where $\langle v_i^2(\tau) \rangle$ is the second moment of velocity. Here we assume a gas temperature of 300 K, and pressure 1×10^{-6} mbar.

We use Eq. 2.7 and Eq. 2.8 to calculate $\langle v_i^2(\tau) \rangle$ along the y axis at $\tau = 1$ ms, as a function of different initial temperatures $T_{i,0}$ and gas pressures P_{gas} .

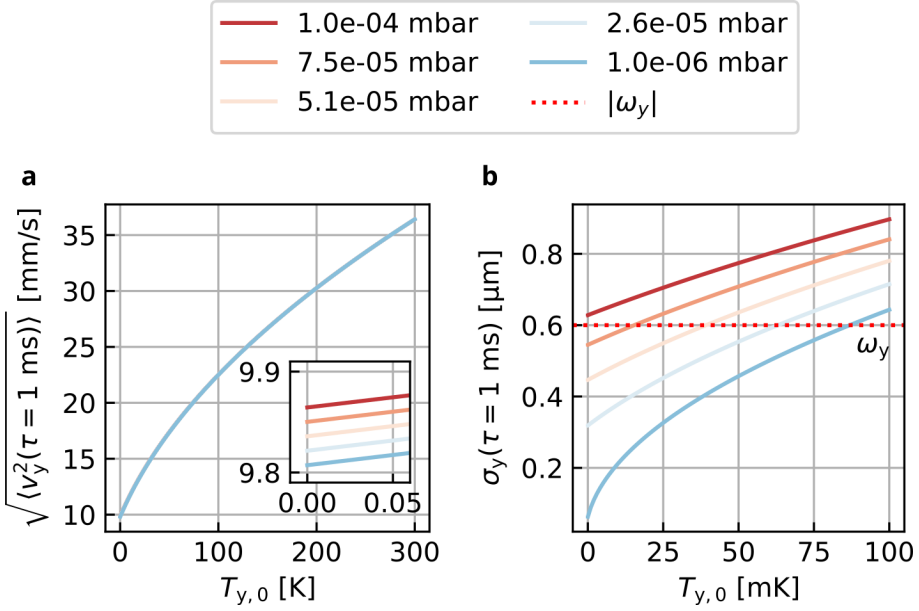


Figure 2.3: **a.** Expected final velocity $\sqrt{\langle v_y^2 \rangle}$ at recapture time $\tau = 1$ ms. **b.** Standard deviation σ_y of the position distribution along the y axis, at recapture time $\tau = 1$ ms. The red dotted line represents the width ω_y of the recapturing trap. For both graphs we plot the relevant quantities evaluated as a function of initial effective temperature $T_{y,0}$ and gas pressure, after a free fall time $\tau = 1$ ms. Here, we assume the nanoparticle has mass $m = 3.4$ fg.

In Fig. 2.3a we observe how even starting with a "hot" COM mode (meaning a high initialization temperature), the velocity stays small enough to satisfy the first requirement. We also notice how the interactions with the gas are a negligible contribution to the overall kinetic energy after the fall.

The depth of the trap is the main parameter that limits the maximum achievable free fall, which in our case is of 37 ms. This can be increased by simply increasing the trap depth.

The second condition limits how much the initial state can expand before $\mathcal{P}(q_i)$ becomes larger than the trapping volume. To ensure high probability of recapture, after τ the standard deviation of $\mathcal{P}(q_i)$ must be smaller than the waist radius ω_i of the focused trapping beam along the respective axis. Knowing the laser power and the focusing lens' characteristics (see Section 2.2), we estimate

that $\omega_z \approx 1.1 \mu\text{m}$, $\omega_x \approx 0.7 \mu\text{m}$, and $\omega_y \approx 0.6 \mu\text{m}$ [8, 18]. The requirement is stricter along the y axis. In Fig. 2.3b we plot $\sigma_y(\tau)$ after a 1 ms free fall, as a function of $T_{y,0}$, and for different P_{gas} . The red dotted line indicates the width of the trap. Here we clearly see an influence of $T_{y,0}$ and P_{gas} over the evolution of the state.

The results give an estimate on the initial requirements. At pressures $< 1 \times 10^{-6}$ mbar, with $T_{y,0} < 1$ mK, the probability of losing the particle would be less than 10^{-6} , or once every one billion repetitions of the experiment, as we explain in detail in the next section.

We work with nanoparticles pre-cooled to COM temperatures of $10 \text{ mK} < T_{y,0} < 50 \text{ mK}$ (see Section 2.2.4). Conducting the experiments at 1×10^{-6} mbar, we estimate a maximum achievable τ of less than 0.5 ms (See Fig. 2.4). We can extend it by working at lower P_{gas} and $T_{i,0}$.

Let's consider the case of a particle cooled to its motional quantum ground state, with $q_{y,\text{zpf}} = 10$ pm. Referring to Eq. 2.12, we impose the condition that $3\sigma_y(t) < 0.6 \mu\text{m}$, and obtain

$$\begin{aligned} \tau &< \sqrt{\frac{\omega_y^2 - 9\langle q_{y,0}^2 \rangle}{9\langle v_{y,0}^2 \rangle}} \\ &< \sqrt{\frac{(0.6 \mu\text{m})^2 - 9q_{y,\text{zpf}}^2}{9\Omega_{y,0}^2 q_{y,\text{zpf}}^2}} < 23 \text{ ms}, \end{aligned} \tag{2.15}$$

with $\Omega_{y,0} = 2\pi \cdot 140$ kHz.

This threshold can be increased by making the waist of the trap bigger, or by initializing the state in a momentum-squeezed configuration, to reduce the speed of its the expansion.

2.1.3 Recapture probability

Based on the considerations of Section 2.1.2, we will now quantify the probability ρ of recapturing the particle after a free fall of duration τ , as a function of

- the initial temperature $T_{i,0}$ of the COM mode;
- temperature T_{gas} and pressure P_{gas} of the gas in the chamber;
- the geometric properties of the recapturing trap, namely its depth U_0 , and center coordinates \mathbf{d} .

The probability of finding a particle in phase space with position q_i and momentum $p_i = mv_i$ is [61]

$$\mathcal{W}(q_i, p_i) \approx \mathcal{P}(q_i)\mathcal{P}(p_i), \quad (2.16)$$

where $\mathcal{P}(p_i) = \mathcal{P}(mv_i)$, and $\mathcal{W}(q_i, p_i)$ is normalized over integration across the whole phase space. The approximation holds only if correlations between q_i and p_i are negligible. For the evolution times considered in this work ($\propto 100 \mu\text{s}$) this condition is verified, since the major and minor axis of the elongated phase space distribution are well aligned with the axes of phase space. Referring to Eq. 2.11 and Eq. 2.12, we normalize σ_{v_i} by the eigenfrequency $\Omega_{y,0}$ to calculate the angle θ between the major axis of the elongated distribution, and the horizontal axis of phase space:

$$\tan(\theta) = \frac{1}{\Omega_{y,0}} \frac{\sigma_{v_i}(t)}{\sigma_{q_i}(t)} \quad (2.17)$$

For $t = 100 \mu\text{s}$, we calculate $\theta = 0.1 \text{ mrad}$, indicating that the off-diagonal terms of the covariance matrix of σ_{q_i} and $\sigma_{v_i}/\Omega_{y,0}$ are vanishingly small, and the two quantities can be treated as not correlated.

We calculate the recapture probability ϱ_i by integrating $\mathcal{W}(q_i, p_i)$ over the portion of the phase space domain that satisfies the recapture conditions.

The kinetic energy K of the particle recaptured at position q_i must be smaller than the depth of the recapturing potential $U(q_i - d_i)$, shifted from the origin of axis i by the distance d_i :

$$K \leq U(q_i - d_i) \rightarrow \frac{p_i^2}{2m} \leq U(q_i - d_i). \quad (2.18)$$

Eq. 2.18 sets a lower and upper boundary to the particle's momentum:

$$p_i \in [-\tilde{p}(q_i), \tilde{p}(q_i)], \quad (2.19)$$

with

$$\tilde{p}(q_i) = \sqrt{2mU(q_i - d_i)}, \quad (2.20)$$

and the recapturing Gaussian potential expressed as

$$\begin{aligned} U(q_i - d_i) &= -U_0 e^{(q_i - d_i)^2 \xi} = \frac{k}{2\xi} e^{(q_i - d_i)^2 \xi} \\ &= -\frac{m\Omega_{i,0}^2 \omega_i^2}{4} e^{-2\frac{(q_i - d_i)^2}{\omega_i^2}}, \end{aligned} \quad (2.21)$$

where $k = m\Omega_{i,0}^2$ is the spring constant, and $\xi = -2/\omega_i^2$ is a measure of the non-linearity of the trapping potential, according to the radius ω_i of the Gaussian beam waist along the considered axis [62].

We integrate Eq. 2.16 over the interval $[-\tilde{p}(q_i), \tilde{p}(q_i)]$ of the momentum domain, and across all the space domain, to find the recapture probability as

$$\begin{aligned} \rho_i &= \int_{\mathcal{R}} \mathcal{P}(q_i) dq_i \int_{-\tilde{p}(q_i)}^{\tilde{p}(q_i)} \mathcal{P}(p_i) dp_i \\ &= \int_{\mathcal{R}} \mathcal{P}(q_i) dq_i \cdot \frac{1}{2} \left\{ \operatorname{erf} \left[\frac{\tilde{p}(q_i) - \mu_{p_i}}{\sqrt{2}\sigma_{p_i}} \right] + \operatorname{erf} \left[\frac{\tilde{p}(q_i) + \mu_{p_i}}{\sqrt{2}\sigma_{p_i}} \right] \right\}. \end{aligned} \quad (2.22)$$

The total recapture probability is given by the product of the contributions of all axes:

$$\rho_{\text{tot}} = \Pi_i \rho_i, \quad (2.23)$$

where $i = x, y, z$, and Π_i indicates the product across the three indexes.

In the following we focus on the one-dimensional probability. We solve Eq. 2.22 numerically to evaluate the loss probability, $1 - \rho_y$, as a function of $T_{y,0}$ and τ . In Fig. 2.4a and b we compare respectively the cases in which the recapturing trap is fixed at the initial position (solving Eq. 2.22 with $d_y = 0 \forall \tau$), and when it is shifted to follow the trajectory of the falling particle (setting $d_y = \mu_y(\tau)$).

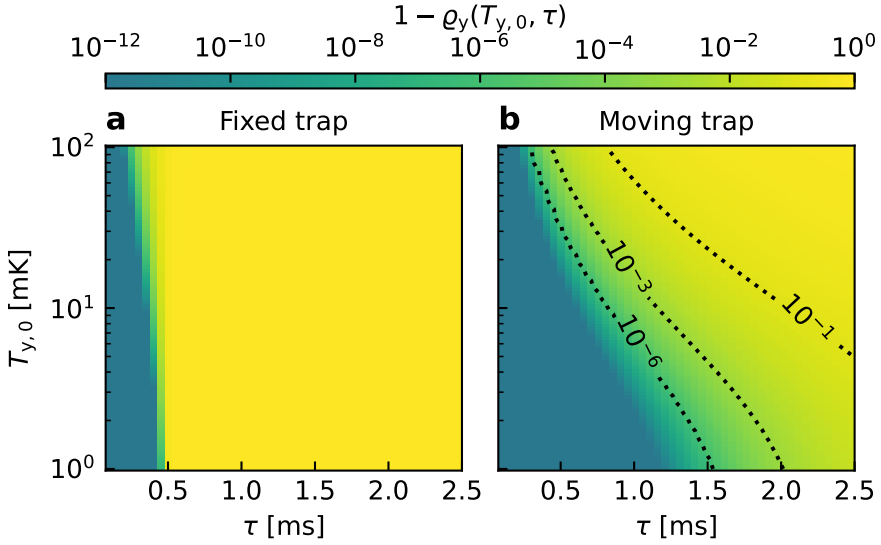


Figure 2.4: Loss probability $1 - \rho_y(T_{y,0}, \tau)$ as a function of initial temperature $T_{y,0}$ and free fall time τ . We compare (a) the cases of a fixed tweezer, and (b) a moving tweezer overlapping with the particle's position at time τ , which we computed imposing $d_y = \mu_y(\tau)$.

As expected, for a fixed $T_{y,0}$, moving the trap along the particle's trajectory allows to perform longer free falls while keeping the loss probability low.

These calculations give us another confirmation of the range of $T_{y,0}$ and τ in which we can operate, although they do not take into account the failure rate due to external factors, such as the electronics or hardware that govern the experiment. Working with $10 \text{ mK} < T_{i,0} < 50 \text{ mK}$, we aim for $\tau \geq 250 \text{ } \mu\text{s}$.

2.1.4 Expected energy at recapture

In the previous sections we investigated the time evolution of the probability distributions for velocity $\mathcal{P}(v_i)$ and displacement $\mathcal{P}(q_i)$ of an object surrounded by gas and subjected to uniformly accelerated motion along the axis i . Additionally, we described how to tune the initial parameters of the experiment (particle kinetic energy, gas pressure etc.) to grant a high recapture probability of the particle for a chosen distance and fall time.

Now we analyze the third part of the protocol, in which the particle is

recaptured. Assuming the distance between the two tweezers is fixed, we calculate the optimal time between the switching of the two traps, ensuring the particle is recaptured with the least total energy. Later, we use this information to calibrate the actual displacement of the movable trap, which in our setup we can only estimate from geometric considerations (see Section 2.2.1.1).

The expectation value for the total energy $\langle H_i(\tau) \rangle$ along a specific axis i as a function of tweezer displacement d_i and fall time τ , is [63]

$$\begin{aligned}
 \langle H_i(\tau) \rangle &= \int_{\mathcal{R}'} dp_i \frac{p_i^2}{2m} \mathcal{P}(p_i, \tau) \\
 &+ \int_{\mathcal{R}} dq_i U(q_i - d_i) \mathcal{P}(q_i, \tau) \\
 &- \int_{\mathcal{R}} dq_i mg_i q_i \mathcal{P}(q_i, \tau) \\
 &= 2 \cdot \frac{1}{2} m \Omega_i^2 \langle q_i^2(\tau) \rangle,
 \end{aligned} \tag{2.24}$$

in which $p_i = mv_i$ indicates momentum, q_i is the particle's displacement and d_i is the center of the recapturing trap. The last contribution is non-zero only along the vertical axis y .

On the right-hand side of the equation we applied the virial theorem [64] to link $\langle H_i(\tau) \rangle$ to the second moment $\langle q_i^2(\tau) \rangle$ of the position of the fallen object, which is what we measure from the data. Upon recapture, the COM resumes its oscillatory motion in the optical trap, with a total energy which depends on the kinetic energy gained during the free fall. The virial theorem allows us to link the total kinetic energy of the COM with its total potential energy. The theorem is applicable to systems not at thermal equilibrium, provided all acting forces are conservative. Experimentally, we evaluate the mean energy at recapture by averaging our signals over many oscillation periods of the COM. Working at 1×10^{-6} mbar, the time of observation (10 ms) is much smaller than the characteristic time $1/\gamma \approx 1 \times 10^3$ s of the non-conservative, relaxational dynamics of the system. Therefore, their effect on the average energy can be neglected.

Solving the integral yields:

$$\begin{aligned} \langle H_i(\tau) \rangle = & \frac{m}{2} \left\{ \mu_{v_i}^2(\tau) + \sigma_{v_i}^2(\tau) \right. \\ & - \frac{\Omega_{i,0}^2 \omega_i^2}{2} \frac{\omega_i}{\sqrt{\omega_i^2 + 4\sigma_{q_i}^2(\tau)}} \exp \left[-2 \frac{(d_i - \mu_{q_i})^2}{\omega_i^2 + 4\sigma_{q_i}^2(\tau)} \right] \\ & \left. - 2g_i \mu_{q_i}(\tau) \right\} + U_0, \end{aligned} \quad (2.25)$$

in which U_0 is the depth of the recapturing trap, and μ and σ refer to mean values or standard deviations, and depend on τ .

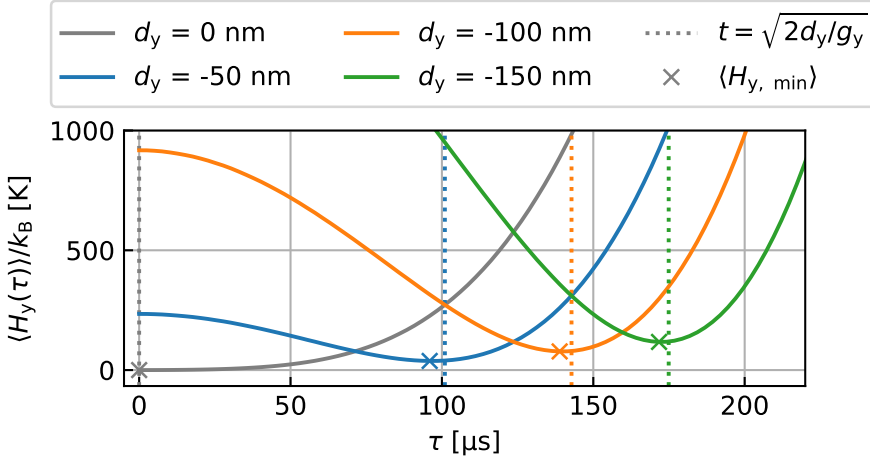


Figure 2.5: Expected energy $\langle H_y(\tau) \rangle$ at recapture along the y axis. We analyze the dynamics as a function of recapture time τ , for different vertical displacements d_y , and fixed initial temperature $T_{y,0} = 10$ mK. The dotted lines indicate at what time the falling nanoparticle reaches the center of the trap. The crosses indicate the minimum $\langle H_{y,\min} \rangle$ of each curve.

In Fig. 2.5 we plot the theory curves for the expected energy along the y axis, with $T_{y,0} = 10$ mK, for different trap displacements. We observe how, depending on d_y , for too short or too long evolution times the energy is higher, as the particle is recaptured far from the center of the trap, with higher potential energy. We notice that the predicted minimum recapture energy $\langle H_{y,\min} \rangle$ is achieved earlier than expected if assuming an average null initial velocity $\langle v_{i,0} \rangle$.

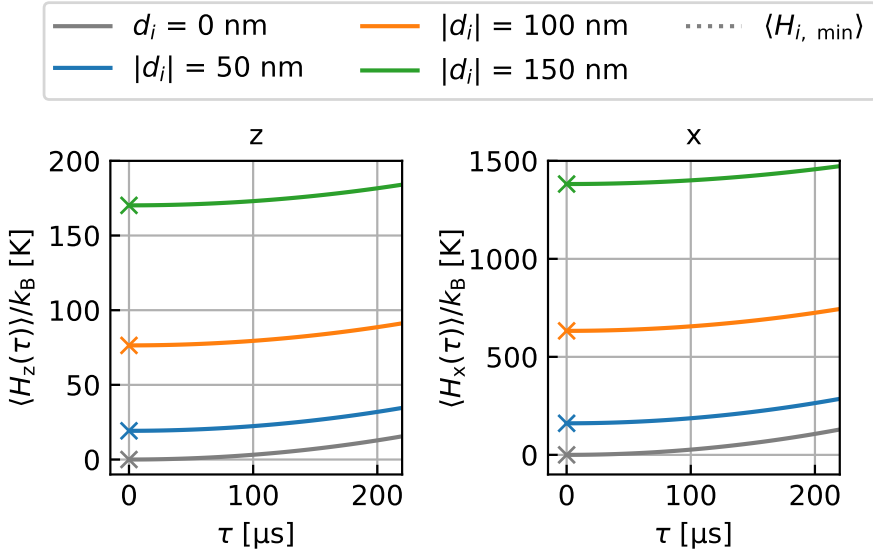


Figure 2.6: Expected energy at recapture along the z and x axes, as a function of τ and displacement d_i along the respective axis, with fixed initial temperature $T_{i,0} = 10$ mK. The crosses indicate the minimum $\langle H_{i, \min} \rangle$ of each curve. Here, $g_x = g_z = 0$.

This is because the second moment $\langle v_{i,0}^2 \rangle$ of velocity at $t = 0$ is not null, and contributes to the energy of the state.

In Fig. 2.6 we plot the curves of the expected energies at recapture along the z and x axis, as a function of different displacements. In absence of any force acting on the falling object, the minimum energy is always at time $t = 0$. This can be deduced from Eqs. 2.10 and 2.24: as the free fall time increases, the linear evolution of σ_{q_i} in time steadily increases the energy of each mode. For small displacements of the trap center along z or x , this is also the dominating contribution to the total energy at recapture.

2.2 The setup

Here we discuss the technical details of the free fall setup.

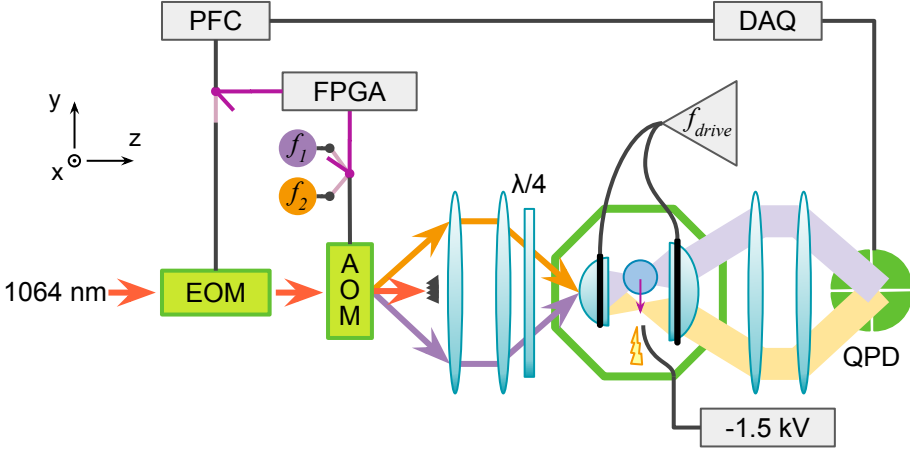


Figure 2.7: Schematic view of the setup. A solid state switch selects between two RF tones, f_1 and f_1 , to drive an AOM and generate an optical trap from the first diffracted order beam. A telescopic system images the resulting beam onto the trapping lens installed inside the vacuum chamber. The nanoparticle is trapped at the focus, which will be at different vertical coordinates depending on the driving frequency. We use a QPD to analyze the light forward-scattered by the particle, and detect its motion. A set of electrodes lets us control the net charge of the particle. AOM: acousto-optic modulator. DAQ: data-acquisition. EOM: electro-optic modulator. PFC: parametric feedback cooling. QPD: quadrant photodiode.

The nanoparticle is trapped in a 100 mW, 1064 nm beam supplied by a free-space laser¹. The polarization is aligned to the horizontal axis of the laboratory, and has a 20° ellipticity.

The core element of the setup is an acousto-optic modulator (AOM). A solid state switch selects between two radio-frequency (RF) tones, f_1 and f_2 , to drive the AOM, creating the optical trap from the first diffracted order beam (see Section 2.2.1). A telescopic system images the tilted beam onto the trapping lens², with clear aperture CA = 0.9 mm, and numerical aperture NA = 0.75. We use a collecting lens³ to collimate the light scattered from the particle, and send it to a QPD placed in forward detection.

¹Mephisto, Coherent

²LightPath, model 355617, working distance 0.19 mm

³LightPath, model 355330, NA = 0.6 at 1064 nm, CA = 5.2 mm, working distance 1.6 mm

The optics are fitted in a custom PEEK mount including a set of three low voltage electrodes, and a high voltage (HV) electrode pointed towards the trapping volume. The HV electrode generates ionized gas molecules to neutralize the charge of the particle in a controlled way. The low-voltage electrodes are used to confirm the particle's charge, by trying to electrically drive the COM motion along the three axes of space, and verifying the absence of a response.

The trapping assembly is mounted inside a vacuum chamber, which can reach pressures of 1×10^{-7} mbar at room temperature. A small amount of the collimated light is reflected by the exit port of the vacuum chamber, and is coupled back into the collimating lens creating a standing wave at the trapping site. This is detrimental for the stability of the trapped particles, as the depth of the standing wave changes with the distance between the exit port and the trap, depending on temperature fluctuations or mechanical vibrations. To mitigate the problem we place a 3 dB absorptive filter (ND = 0.3) inside the vacuum chamber, just before the back optical port, tilted by 30° . The filter attenuates the signal-to-noise ratio (SNR) of our detection by a factor $10^{-ND} = 0.5$, reducing the overall measurement efficiency, but its use is necessary to stabilize the eigenfrequencies of the COM modes for the whole length of the experiment.

2.2.1 Creating a steerable trapping beam

Here we describe in detail how we exploit the AOM to create a movable trapping beam.

The AOM⁴ has a center frequency of 80 MHz, and a RF bandwidth of 30 MHz. The angle at which the diffracted beams emerge from the AOM depends on the frequency f_n of the driving RF tone, according to the Bragg condition

$$\theta_B \approx a \frac{\lambda f_n}{2V} \quad (2.26)$$

in which $a \in \mathbb{Z}$ is the order of diffraction ($a = 1$ in our case), λ is the laser wavelength, and V the acoustic velocity in the AOM crystal. Changing f_n , we thus control the angle of incidence of the beam onto the trapping lens, after

⁴Gooch&Housego 3080-197, designed for 1550 nm light

imaging through the telescope. As a consequence, the focus is shifted vertically along the trapping plane.

The transfer function of the AOM has a finite bandwidth, so different RF tones have different diffraction efficiencies. By controlling the amplitude of the tones we compensate for this effect, and make sure the trapping beam has a constant power no matter the frequency chosen (see Appendix C).

We characterize the response time of the AOM to be ~ 300 ns, much faster than the particle's dynamics. Hence, using the AOM we can easily tune the particle's free evolution time, by using the solid state switch to shut off (turn on) the RF drive to extinguish (shine on) the corresponding diffracted beam which creates the trap.

Moreover, this configuration makes it easy to reinitialize the system after each completed protocol. Once the particle is recaptured in the lower tweezer, the frequency f_2 of the second driving tone can be shifted towards that of the first RF tone, f_1 , thus bringing the particle back to the drop point.

2.2.1.1 Estimation of the trap displacement

Here we estimate by how much we displace the focus of the optical tweezer as a function of the difference Δf_{AOM} between the frequencies f_1 and f_2 of the driving tones. We use geometrical considerations knowing the magnification of the telescope used to image the beam onto the trapping lens, and the effective focal length of the lens itself.

For our estimation, we drive the AOM with two tones, at 65 MHz and 85 MHz, and measure their distance after the first lens of the telescope with a beam profiler⁵, yielding a beam separation of 1.1(1) mm between their centers. Knowing the focal length of the second lens in the telescopic system ($F_2 = 30$ cm) and the effective focal length of the trapping lens ($F_{\text{EFL}} = 0.53$ mm), we can work out the reduction factor M for the distance between the centers of the foci:

$$M = \frac{F_{\text{EFL}}}{F_2} \approx 1.77 \cdot 10^{-3} . \quad (2.27)$$

From this, we estimate that for each MHz of difference between the two driving

⁵Thorlabs BP209-VIS/M

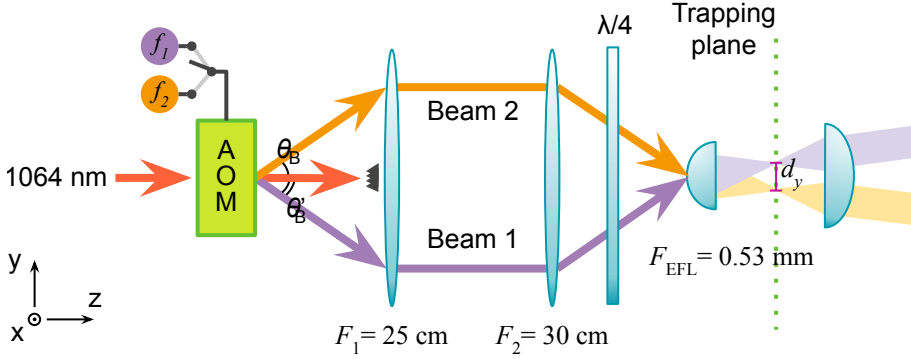


Figure 2.8: Imaging system for the vertically diffracted beams. We can roughly estimate the distance between the tweezers' foci by knowing the focal length of each lens, and the angular displacement between the beams.

tones, the separation between the foci will be ~ 100 nm:

$$d_y \approx \frac{100 \text{ nm}}{\text{MHz}} \Delta f_{\text{AOM}}. \quad (2.28)$$

We check the validity of this calibration a posteriori from the free fall experimental data in Section 2.3.3.

2.2.2 Discharging the particle

The particle's electrical charge is neutralized before starting the experiment, to avoid disturbances from electric stray fields. We use an high voltage generator (-1.5 kV, designed by Karol Luszcz) to ionize the air in the chamber at a pressure of 0.4 mbar. As the ionized gas molecules collide with the particle, they will change the net charge on its surface.

The HV signal is brought close to the particle with a thin copper wire placed inside the vacuum chamber, and connected to the voltage generator via a feedthrough in one of the viewports. One extremity of the copper wire is sharpened, and taped in place so that it sits 1 cm from the trapping volume. When the particle is still charged, we drop the pressure in the chamber to 0.4 mbar, and drive the particle motion with a coherent electrical tone. We then switch on the HV generator, and monitor the response of the particle to

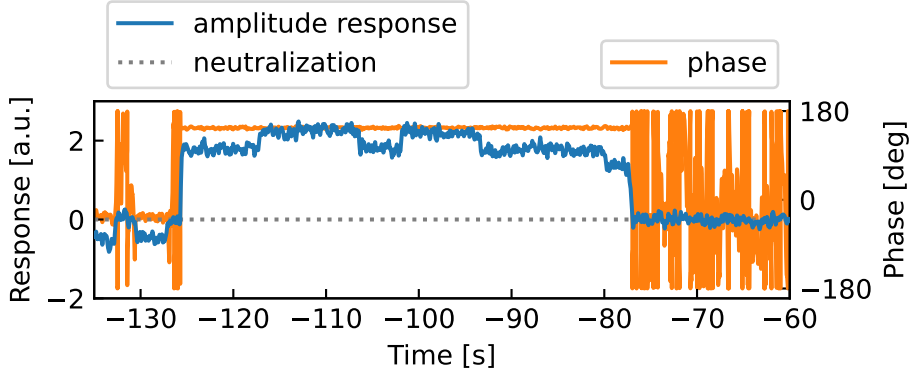


Figure 2.9: Neutralization of the particle’s electrical charge. We drive the charged particle with a coherent electrical tone, and demodulate the QPD signal at the drive’s frequency to study the amplitude response (in blue) and phase (in orange). The smaller discrete steps in the amplitude response indicate a variation of the total charge by an elementary unit $|e^-|$.

the electrical drive. As the ionized molecules strike the particle, we can resolve single charging/discharging events from the amplitude of the response at the driving tone (Fig. 2.9) [65]. When the amplitude response to the electrical drive is null, the particle has reached charge neutrality.

2.2.3 Detecting the particle’s dynamics

The motion of the particle is encoded in the phase of its scattered field. We read it out using a high power QPD (designed and built by Erik Hebestreit [18]) to measure the particle’s motion along all axes simultaneously.

The QPD features a bandwidth (BW) of ≈ 1 MHz, and can withstand up to 50 mW of total incident light. It can be directly placed in forward detection without the need to dramatically attenuate the beam power, which would reduce the SNR. Due to the NA mismatch between the trapping and collimating lens, and the 3 dB attenuation in front of the output port of the vacuum chamber, 27 mW of light reach the QPD diodes. When performing longer free fall experiments ($\tau > 200 \mu\text{s}$) we attenuate the incident power by an additional 3 dB, to prevent the voltage signal from saturating the detector output. The magnitude of the signal is proportional to the amplitude of the COM motion. When the particle’s oscillations become too big at recapture, attenuating the incident laser

power ensures the voltage signal does not exceed the detector output range, which would lead to loss of information on the particle's dynamics.

With this amount of incident light, the overall detection noise is close to the shot noise limit, but still dominated by the detector's electronic noise, and by the AOM pointing noise, due the phase noise of its driving source.

Traps created by different RF tones are not vertically overlapped. After propagation through the trapping and collimating lens, the signals reach the quadrants of the detector at different heights, giving rise to an imbalance in the QPD y channel. This results in a suppressed common-mode rejection ratio (CMMR), and thus an increase in the noise floor due to classical laser noise. We observed that when the traps are switched on or off, this also generates a significant DC offset of the output. The sudden change sometimes induces a temporary ringing of the amplification circuit, saturating the outputs for a few milliseconds. To solve the problem we built an imaging system in forward detection, so that no matter the angle of the beam (i.e. the displacement between the traps), the signals are all co-aligned on the same spot of the QPD, reducing the sudden electronic saturation effects while improving the overall CMMR stability.

Nevertheless, the outputs still saturate after the second trap is switched on, so the information about the particle's motion is lost or severely distorted in the first few hundreds of microseconds after the particle's recapture. This data is then excluded from the analysis.

2.2.3.1 Calibrating the signal to displacement units

The signals collected for this experiment are derived from the photocurrents generated by the QPD, and converted to voltages. To have a quantitative idea of the magnitude of the particle's displacement, we convert the voltage values to units of displacement (i.e., meters) [40]. To do so, we rely on a reference signal acquired at high pressures, where we assume the particle to be thermal equilibrium with the surrounding gas bath at $T = 300$ K. From the equipartition theorem we estimate the second moment $\langle q_i^2 \rangle$ of the COM displacement along

the axis i :

$$\frac{1}{2}k_B T = \frac{1}{2}m\Omega_i^2\langle q_i^2 \rangle. \quad (2.29)$$

We analyze the system's dynamics in frequency domain, by calculating the power spectral densities (PSDs) of the signals, shown in Fig. 2.10. We measure the energy in each COM mode by integrating the area under the relative peak in the PSD curve, corresponding to $\langle q_i^2 \rangle$. This value is in V^2 . At high pressures, we apply Eq. 2.29 (with $T = 300$ K) to the integral values extracted for each mode, thus retrieving a calibration factor which we then use to convert the signals acquired at lower pressures from volts to meters.

The x and y modes are very close to each other. To get a better result, we fit a double Lorentzian, with a peak at Ω_x and one at Ω_y . We do the same also for the z COM mode, which we fit together with the x peak. With this we estimate the damping ratio across all three axis.

In Tab. 2.1 we present a summary of the values calculated for all three COM modes from the calibration signal acquired at 10 mbar with the particle used in

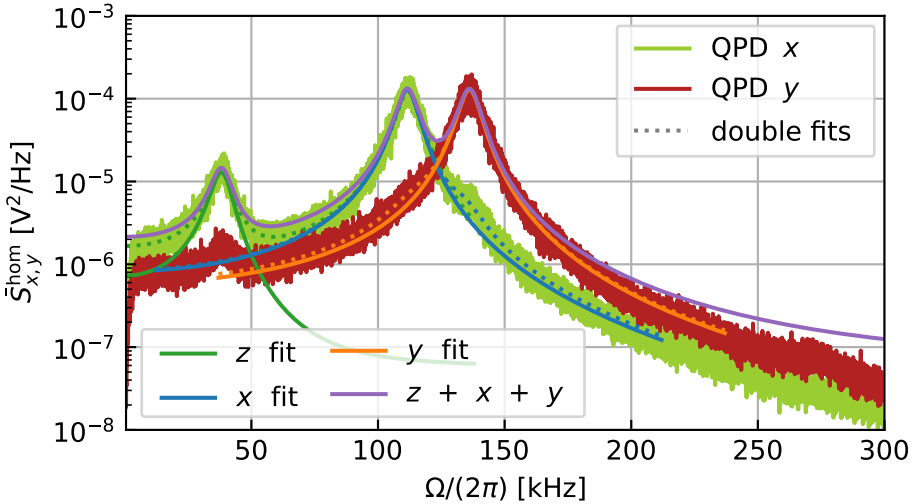


Figure 2.10: PSDs $\bar{S}_{x,y}^{\text{hom}}$ of the x and y channels QPD photocurrents acquired at 9.8 mbar. We fit double Lorentzians (dotted lines), to extract the parameters relevant to each of the three modes (amplitude, linewidth, central frequency). In solid lines, we plot the fitted Lorentzians for each mode. We do not record the output from the QPD's z channel, so we use the x channel signal to calibrate also the motion along the z axis.

this work. We denote with c the conversion factor from Volts to meters, with γ the damping ratio, and with $\Omega_{i,HP}/(2\pi)$ the eigenfrequency of each mode at high pressure. At lower pressures, when we apply the parametric feedback cooling (see Section 2.2.4), the eigenfrequencies all increase by 1%, as the thermal state is confined to the steeper bottom of the Gaussian potential well. From the fitted linewidths γ we also estimate radius R and mass m of the particle, knowing that [40]

$$R = 0.619 \frac{9}{\sqrt{2\pi}\rho_{\text{part.}}} \sqrt{\frac{M}{N_A k_B T_{\text{gas}}} \frac{P_{\text{gas}}}{\gamma}}, \quad (2.30)$$

where $\rho_{\text{part.}} = 2200 \text{ kg/m}^3$ is the density of silica, $M = 28.97 \times 10^{-3} \text{ kg/mol}$ is the molar mass of air, and N_A the Avogadro number.

We find that the radius is 58(8) nm, for a diameter of 116 nm. The mass has an uncertainty of 40% its own value. This will be relevant for the analysis of the data based on Eq. 2.25, where we will reformulate our model to simplify the mass out of the equations.

2.2.4 Cooling the particle's motion

We use parametric feedback cooling (PFC) to reduce the COM oscillation amplitudes [66]. The technique relies on detecting the oscillations of the COM, and modulating the intensity of the trapping beam at double their frequency. By choosing the correct phase, we exploit the stiffening and relaxing of the trapping potential to reduce the energy of the COM modes, effectively damping the oscillations. The COM oscillates along three different axes, so we perform

	$\Omega_{i,HP}/(2\pi)$ [kHz]	c [V/ μm]	γ [kHz]	m [fg]	R [nm]
x	111.99(2)	18.8(5)	9.43(4)	1.6(6)	59(8)
y	136.38(3)	23.9(6)	9.18(4)	1.7(8)	57(8)
z	38.36(3)	2.2(6)	8.87(4)	1.9(8)	59(8)

Table 2.1: Summary of the conversion factor c and gas damping ratio γ extracted from a signal acquired at 10 mbar with the nanoparticle used in this work. We also estimate its mass m and radius R .

PFC across all of them by summing up the signals. At high pressures, the COM modes are thermalized with the surrounding gas, at 300 K. We apply PFC from 1×10^{-3} mbar and below, to reduce the effective temperature along each axis to the millikelvin range.

We keep track of the instantaneous oscillation frequencies with the use of three phase-locked loops (PLLs). Each loop takes as input the signal detected by the QPD, looks for the tone with the highest amplitude in the appropriate BW (chosen depending on which axis we want to cool), then outputs a signal at double the frequency of the mode. The phase offset of each output tone is set experimentally, observing the response of the particle to different phases, and choosing the one that minimizes the energy in the mode (i.e., minimizes the area under the PSD peak). A comprehensive overview of PFC can be found in [9].

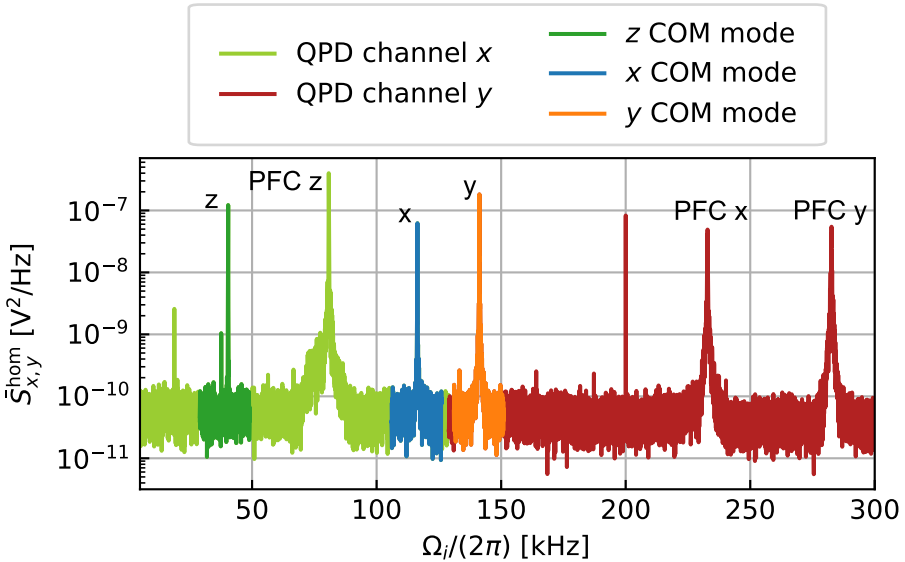


Figure 2.11: PSDs of the PLL-cooled COM modes at 1×10^{-6} mbar. With our system's parameters (100 mW of 1064 nm light focused by a 0.75 NA lens) our modes have frequencies $\Omega_{z,0} = 2\pi \cdot 40.6(1)$ kHz, $\Omega_{x,0} = 2\pi \cdot 116.6(1)$ kHz and $\Omega_{y,0} = 2\pi \cdot 141.6(1)$ kHz. At double these frequencies we apply the PFC tones, which can be seen in the graph above at $\approx (81, 234, 282)$ kHz respectively, due to the imperfect balancement of the signal.

Minimizing the COM energy ensures that the recapture probability after

the drop is large, as shown in Fig. 2.4. Another (more technical) parameter that strongly constrains the repeatability of the experiment is how reliably the PLLs stay locked on the COM signals, since this heavily influences how many times the experiment can be performed without losing the particle after recapture. The greatest challenge is to keep a stable lock on the COM y eigenfrequency when it abruptly changes at recapture due to the nonlinear potential [67] as the particle's oscillations become of the order of ~ 100 nm. This induces a sudden redshift of the COM eigenfrequencies of as much as 10 kHz along the vertical axis. Occasionally, this causes the PLLs to lose lock to the actual signal, applying the PFC at the wrong frequency, thus further exciting the particle and kicking it out of the trap.

Throughout this project great effort has been dedicated to increasing the overall performance of the cooling, by improving the SNR of the detection, but especially the reliability of the PLLs that generate the cooling feedback.

We apply the PFC by modulating the laser intensity with a dedicated electro-optic modulator (EOM). The PFC signals are generated by two Zurich Instrument MFLI boxes. Originally, we experimented with the PLLs integrated in the Zurich Instrument HF2LI box. However, such digital PLL loops struggle to lock to signals that have sudden changes over a large bandwidth. Finally, we implemented our PFC entirely with the MFLI PLL/PID modules. Their software offers a phase unwrap option, which automatically corrects for phase discontinuities bigger than π , originating when the oscillator frequency has a sudden change. This greatly increases the stability of the loop, and its bandwidth [68]. The COM modes across all axes can now be cooled reliably to < 50 mK for initialization and after recapture. More importantly, we reduced the particle loss rate to well below 1×10^{-3} , meaning that we can complete more than one thousand repetitions of the experiment before accidentally dropping the particle, and having to load a different one.

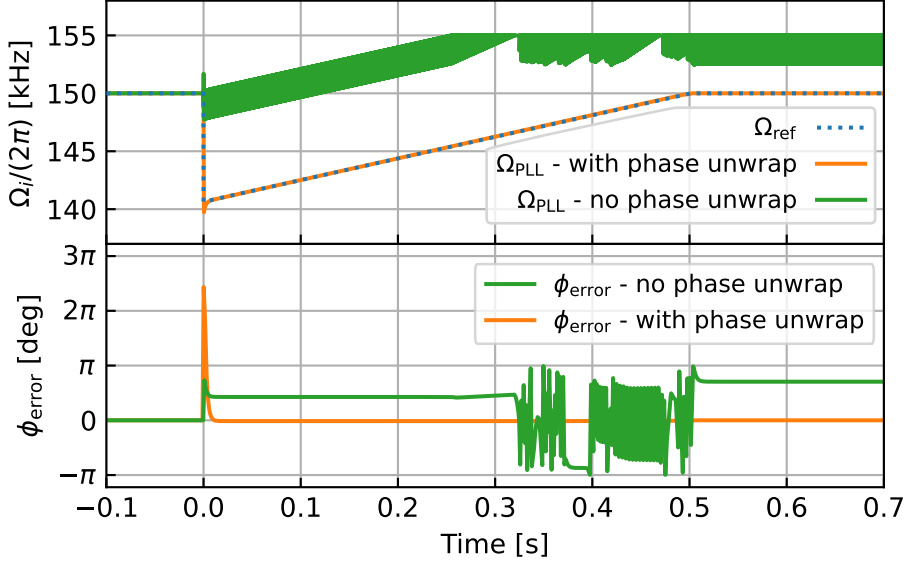


Figure 2.12: Simulation of the effect of phase unwrap correction on the MFLI PLL frequency output (top panel) and error (bottom panel). We control a reference oscillator Ω_{ref} to simulate the abrupt redshift of the COM y frequency during our experiment. We try to lock two identical MFLI PLLs to this signal, but disable the phase unwrap correction for one of them. As a result, this PLL cannot lock back to Ω_{ref} after the frequency jump.

2.3 Free fall of a nanoparticle

2.3.1 Measuring protocol

We use a field-programmable gate-array⁶ (FPGA) to create digital (TTL) signals that coordinate the action of all the electronics involved in the experiment, timing its various stages.

The process is initialized from the computer via Ethernet, through a custom Python interface, which modifies the registers on the FPGA according to the user's inputs. When the FPGA is prompted to start the protocol, it generates four trigger signals, with relative delays between each other.

One of them is the "master" trigger, used to start the data acquisition; the other three are connected to solid state switches, and control either the status of the traps, or the feedback cooling. The delays between each pair of trigger can

⁶RedPitaya STEMLab 125-14, programmed with custom code

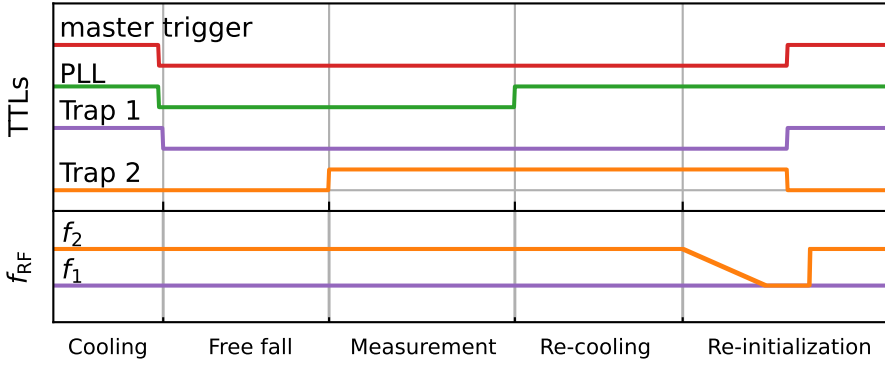


Figure 2.13: Status of the FPGA outputs during the different phases of the experiment. During the re-initialization phase, the frequency f_2 of the recapturing beam is shifted towards f_1 . The particle is dragged along the vertical axis, to bring it to its initial position. The two tweezers are then instantaneously swapped, and f_2 reset to its original value, to start the protocol again.

be set by the user.

The algorithm controlling the experiment works as follows.

First, we record a spectrum of the COM motion to calculate the effective temperature of the initial state, from the PSD integral. If the temperature is above 50 mK, the protocol is paused, the PLLs reset, and the procedure is halted until the COM temperature drops again. This step is optional, and lengthens the total acquisition time, but increases the experiment's chances of success.

When the COM's temperature is low enough, a signal prompts the FPGA to start the free fall protocol. The master trigger is engaged, and the data acquisition starts. At the same time, a second trigger controls a solid state switch that stops the PLL cooling, which we switch off before the optical trap to prevent any spike of the detector signal to be fed back through the electronics.

After 1 μ s, a third trigger sends the input to shut off the primary trap, thus starting the particle's free fall.

After a delay τ , a fourth trigger gives the input to turn on the second trap, recapturing the particle. Light reaches the detector again, and the particle's oscillations are visible in the signal. The particle can now be cooled, and brought up to its initial position by shifting the tweezer upwards, terminating one repetition of the experiment.

2.3.2 Free fall and recapture between overlapped foci

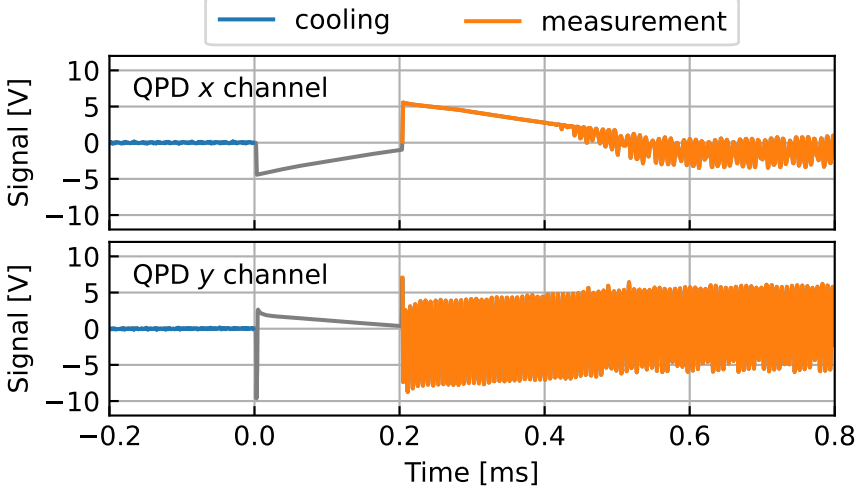


Figure 2.14: Dynamics of a nanoparticle in free evolution for $200 \mu\text{s}$, released and recaptured over overlapped tweezers.

We first test the protocol working in the geometry already studied in [59], in which the release and recapture tweezer are overlapped.

We choose a nanoparticle with diameter of $122(17) \text{ nm}$, and run the protocol at pressures of $1 \times 10^{-6} \text{ mbar}$. Currently, we reliably achieve $200 \mu\text{s}$ of free evolution between release and recapture of the particle. In Fig. 2.14 we plot a single shot timetrace of the QPD signals after a free fall of $200 \mu\text{s}$. The particle should have travelled $\approx 200 \text{ nm}$ from the center of the tweezer, whose radius we estimate to be $\omega_y = 700 \text{ nm}$. To the best of our knowledge, it is the first time that such a free evolution has been realized at a pressure of $1 \times 10^{-6} \text{ mbar}$ on these timescales, and with nanoparticles of this dimensions.

2.3.3 Free fall between separated tweezers

We now describe the measurements realized by dropping the particle between displaced tweezers. We use a nanoparticle with a diameter of $116(16) \text{ nm}$ (see Tab. 2.1), and drop it at $1 \times 10^{-6} \text{ mbar}$ across tweezers that are displaced across estimated distances that range from 50 nm to 150 nm . The datasets are

acquired with the Scope module of a Zurich Instruments MFLI, triggered on the master trigger generated by our FPGA. Following the experimental protocol

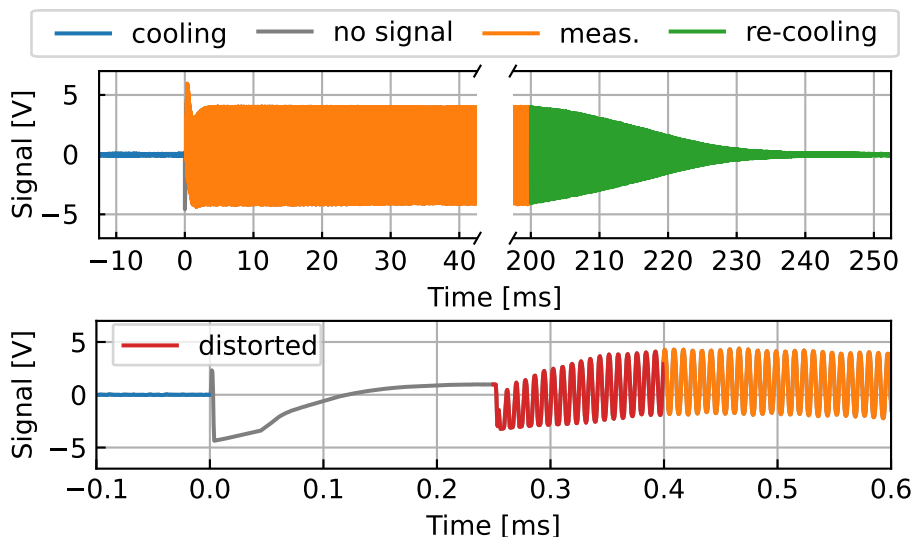


Figure 2.15: Example of a recorded timetrace, with highlighted protocol phases. On the bottom panel we show the details of a realization with free fall time of 250 μs , between tweezers displaced by -222 nm ($\Delta f_{\text{AOM}} = 2.5\text{ MHz}$).

detailed in Section 2.3.1, each timetrace can be divided in different sections, highlighted in Fig. 2.15, corresponding to each block of the protocol.

- First section: the particle sits in the upper trap, and its motion is cooled via parametric feedback. This section thus contains information on the initial state of the particle, before the free fall.
- Second section: starts when the first tweezer is shut off, and ends when the second tweezer is turned on. It varies in length accordingly with the free fall time chosen. It does not contain any information on the particle's dynamics, since no light is reaching the detector.
- Third section: is the one we use to verify the state after the free fall. It starts as soon as the second tweezer is turned on, and carries information on the energy and dynamics of the particle right after recapture. The first 150 μs are discarded, due to being distorted by the saturation of the QPD's amplification chain.

- Fourth section: starts when the parametric cooling is reactivated, and is recorded for diagnostics reasons in the event that the PLLs fail to engage.

We analyse the data by taking the ratio $\tilde{H}_i(\tau)$ between the energy at recapture $\langle H_i(\tau) \rangle$, and the energy of the initialized state $\langle H_i(0) \rangle$. Starting from Eq. 2.25, which we evaluate for $\gamma \rightarrow 0$, we recall that $\langle H_{i,0} \rangle = m\Omega_{i,0}\langle q_{i,0}^2 \rangle$, and obtain

$$\begin{aligned} \tilde{H}_i(\tau) &= \frac{\langle H_i(\tau) \rangle}{\langle H_{i,0} \rangle} = \frac{m\Omega_i^2(\tau)\langle q_i^2(\tau) \rangle}{m\Omega_{i,0}^2\langle q_{i,0}^2 \rangle} \\ &= \frac{1}{2} - A \frac{\omega_i^2}{4\langle q_{i,0}^2 \rangle} \frac{\omega_i}{\sqrt{\omega_i^2 + 4\sigma_{q_i}^2(\tau)}} \exp \left[\frac{-2(d_i - \mu_{q_i})^2}{\omega_i^2 + 4\sigma_{q_i}^2(\tau)} \right] \\ &\quad - A \frac{\omega_i^2}{4\langle q_{i,0}^2 \rangle}. \end{aligned} \quad (2.31)$$

The normalization simplifies the mass m out of the equation, to suppress uncertainties due to the imprecision on the estimated particle mass (Tab. 2.1).

For the same reason, we introduced a scaling factor A to account for the error in the conversion of $\langle q_{i,0}^2 \rangle$ to meters. In fact, we measure $\langle q_{i,0}^2 \rangle$ in V^2 from the first section of the acquired data, by integrating the area under the peak of the i -th mode of the signal's PSD. The conversion to meters relies on the calibration factor c we extracted previously, in Tab. 2.1, which also has a significant uncertainty.

We do not include a scaling factor for $\sigma_{q_i}^2(\tau)$, as it appears only in terms summed in quadrature with ω_i . Since $\omega_i \gg \sigma_{q_i}(\tau)$, those terms are dominated by the size of the waist of the beam, which we take as fixed, recalling that $\omega_y = 0.6 \mu\text{m}$, $\omega_z = 1.1 \mu\text{m}$, and $\omega_x = 0.7 \mu\text{m}$ [8].

The frequencies $\Omega_{i,0}$ and $\Omega_i(\tau)$ are evaluated from the data. Note how in general $\Omega_i(\tau) \neq \Omega_{i,0}$, because of the redshift at recapture due to the Duffing nonlinearities. Before release, we measure $\Omega_{z,0} = 2\pi \cdot 40.6(1)$ kHz, $\Omega_{x,0} = 2\pi \cdot 116.6(1)$ kHz and $\Omega_{y,0} = 2\pi \cdot 141.6(1)$ kHz.

In Fig. 2.16 we plot $\tilde{H}_i(\tau)$ as a function of recapture time τ and tweezer

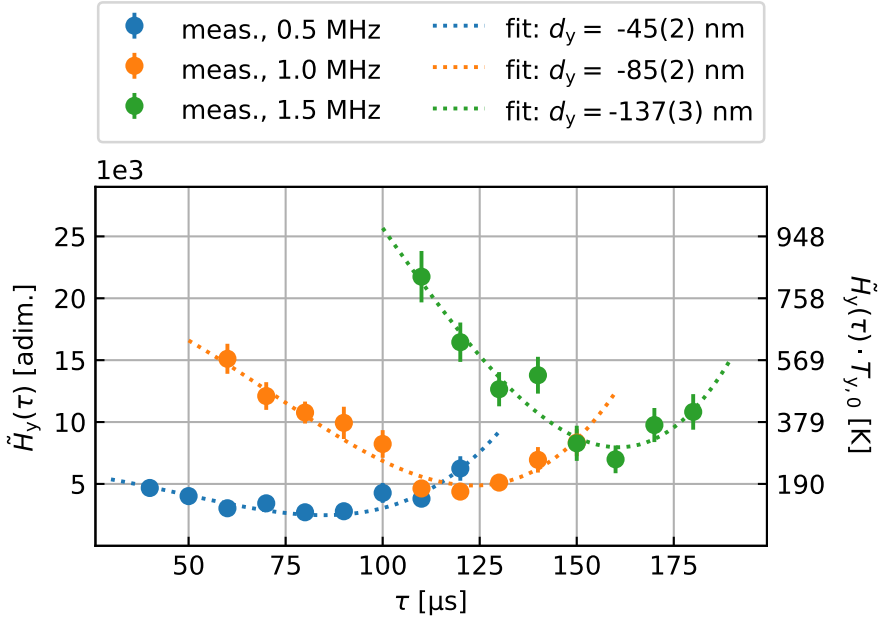


Figure 2.16: Normalized average recapture energy $\tilde{H}_y(\tau)$ as a function of τ and d_y . All three datasets were acquired with the same particle. The dots represent experimental data, and the error bars the unbiased standard error calculated over the average of one hundred acquisitions. The dotted lines are fits of Eq. 2.31 with d_y , $\langle q_{y,0}^2 \rangle$ and A as parameters. On the left side of the figure we rescale the ratio, assuming an initial temperature $T_{y,0} = 37$ mK, which we extrapolate by comparing the average integral under the PSD y peak at recapture with the PSD acquired at high pressure (Fig. 2.10).

y COM mode			
	0.5 MHz	1.0 MHz	1.5 MHz
d_y [nm]	-45(2)	-85(4)	-137(3)
$\langle q_{y,0}^2 \rangle$ [nm ²]	1.13(1)		
A [adim.]	1.4(2)		

Table 2.2: Fitted values of the trap displacement d_y , the scaling factor A , and $\langle q_{y,0}^2 \rangle$.

separation d_y , set by changing Δf_{AOM} from 0.5 MHz to 1.5 MHz.

The three datasets were acquired using the same particle. Each point in the graph is the result of averaging over one hundred realizations of the experiment,

for each configuration of free fall time and displacement.

The error bars represent the unbiased standard error over the hundred averaged ratios (i.e., the standard deviation divided by the square root of the number of samples minus one).

The dotted lines in Fig. 2.16 are fits of Eq. 2.31, with d_y , A , and $\langle q_{y,0}^2 \rangle$ as parameters. We summarize the results in Tab. 2.2.

On the right side of the graph we rescale the ratio by the temperature $T_{y,0}$ of the thermal state at initialization, which we evaluate from the PSD by comparing the average of the one hundred integrals under the y peak for all one hundred realizations, with the integral of the PSD acquired at high pressures. We find $T_{y,0} = 37$ mK, $T_{x,0} = 16$ mK and $T_{z,0} = 45$ mK.

From Fig. 2.16 we identify at which τ do we find the minima of the experimental curves. For different tweezer displacements, we observe that the recapture energy is minimized for τ that approach the expected time needed for an object accelerated by gravity to cross the distance d_y . The minima lie slightly before $t = \sqrt{2d_y/g_y}$, as expected from the theory model presented in Fig. 2.5. For increasing free fall times, the total energy grows again, as the particle crosses the center of the recapturing trap and samples areas characterized by a higher potential energy.

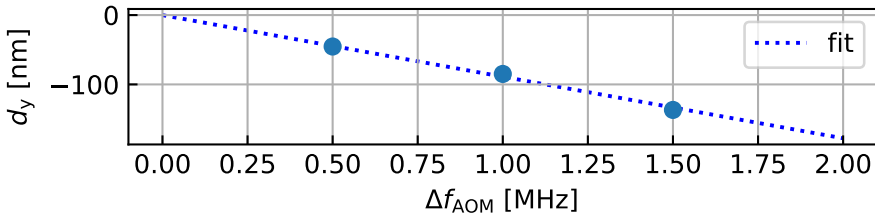


Figure 2.17: Trap separation d_y as a function of frequency difference Δf_{AOM} between the AOM driving tones. The values extrapolated from the data lie on a line with slope of $-89(3)$ nm/MHz, and intercept of $0(3)$ nm.

We use the position of the minima to calibrate the distance between the center of the tweezers (Fig. 2.17). Each megahertz of difference between the frequency tones corresponds to $89(3)$ nm of separation between the traps' centers, close to the value we estimated.

We use this information for later acquisitions, in which we push the free fall time up to 270 μs , moving the tweezer by $-356(12)$ nm.

From the data in Fig. 2.16, and the fit results summarized in Tab. 2.2, we conclude that although there is a systematic error in the conversion of $\langle q_i^2(\tau) \rangle$ to meters, due to the imprecision on the estimate of the factor c in Tab. 2.1, the experimental data is well described by our model.

2.3.4 Along z and x

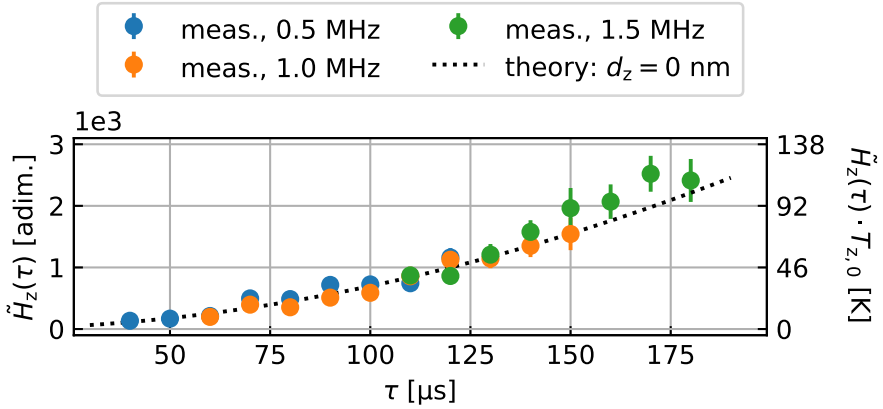


Figure 2.18: Measured normalized energy $\tilde{H}_z(\tau)$ at recapture along the axis z , as a function of τ and Δf_{AOM} . The black dotted line is a fit of Eq. 2.31. We assume $d_z = 0$, and leave only the scaling factor $A = 2.2(1)$ as a free parameter. On the left, the vertical axis is rescaled assuming an initial temperature $T_{z,0} = 45$ mK, which we extrapolate from the data.

		z COM mode		
		0.5 MHz	1.0 MHz	1.5 MHz
A [adim.]	2.2(1)			

Table 2.3: Fitted values of the scaling factor A for the z COM mode analysis.

We now focus on the experimental analysis of $\tilde{H}_i(\tau)$ at recapture along the axes z and x , perpendicular to the free fall.

In Fig. 2.18 we plot the data relative to the z axis. We see that independently of Δf_{AOM} the points follow a trend which increases monotonically with τ . This

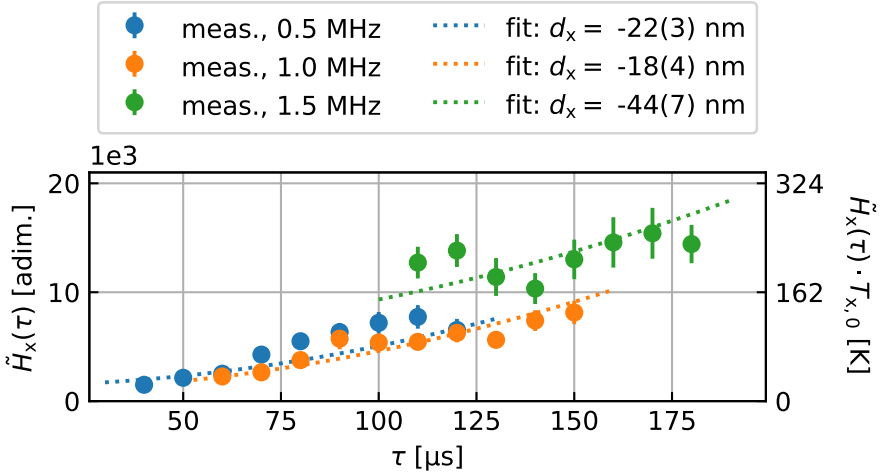


Figure 2.19: Measured $\tilde{H}_x(\tau)$ at recapture, as a function of τ and Δf_{AOM} . The dotted lines are fits of Eq. 2.31, with d_x and A as parameters. On the right side, we rescale the axis considering $T_{x,0} = 16$ mK, which we extrapolate from the PSD.

x COM mode			
	0.5 MHz	1.0 MHz	1.5 MHz
d_x [nm]	-18(2)	-15(4)	-36(6)
A [adim.]	1.4(2)		

Table 2.4: Fitted values of the displacement between the tweezers d_x , and the scaling factor A , for the x COM mode.

is congruent with our model, in which the center of the release and recapturing tweezers are coincident along z , such that the least recapture energy is at $\tau = 0$. The main contribution to $\tilde{H}_z(\tau)$ is the expansion of $\sigma_z(\tau)$. We fitted the data with Eq. 2.31, leaving as only fit parameter the scaling factor A , and assuming an initial temperature of $T_{z,0} = 45$ mK, which we extrapolate comparing the interval of the PSD z peak with our reference at high pressure. We find $A = 2.2(1)$.

Similarly, we analyze the information collected along the x axis, which is perpendicular to the gravitational acceleration. Also in this case, the model

follows a general trend of increasing $\tilde{H}_x(\tau)$ for increasing τ .

Here we left both d_x and A as fit parameters, assuming an initial temperature of $T_{x,0} = 16$ mK which we measure from the PSDs.

From the results in Tab. 2.4 we conclude that by changing Δf_{AOM} we are moving the trap diagonally, so also along the x axis. This influences the potential landscape, as highlighted by Fig. 2.6, but does not determine a change of momentum along x , since the gravitational acceleration acts only along y .

Overall, a diagonal displacement of the trap is not a problem for our measurements, and can eventually be corrected by more carefully tilting the AOM.

2.4 Phase space reconstruction

We now reconstruct the phase space distribution of the state before release, and at the recapture instant τ , to experimentally verify how do the probability distributions $\mathcal{P}(q_i)$ and $\mathcal{P}(p_i)$ evolve as a function of free fall time. We do so using the information contained in the timetraces, to extrapolate phase and amplitude of the COM dynamics just before release of the particle from the trapping field, and at the instant of recapture.

The thermal state is described by Gaussian probability distributions both in position domain q_i , and momentum domain p_i , with $i = z, x, y$. As mentioned before, a Gaussian is characterized by its mean and its standard deviation, so we can reconstruct the trajectory of the thermal state in phase space by knowing the mean $\mu(t)$ and standard deviation $\sigma(t)$ for both the position and momentum distributions.

The only force acting during the free fall is gravity. Along the vertical axis we expect a deterministic drift of the mean position $\mu_y(t)$ and momentum $\mu_{p_y}(t)$ of the nanoparticle, while the center of the distributions for the z and x COM modes stay centered around the origin of phase space for the whole evolution. Regarding the width of the distributions (i.e., their standard deviations σ), we expect that points that have positive (negative) momentum in phase space at the start of the free evolution, will keep moving at constant speed along the positive (negative) position axis, in absence of an external force. After a time τ , the

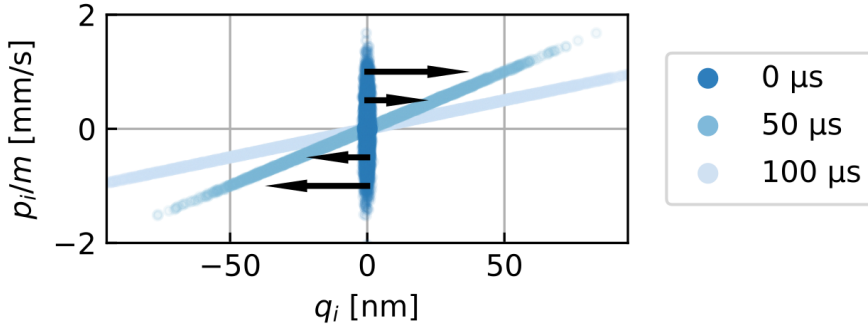


Figure 2.20: Monte Carlo simulation of the evolution of a thermal state ($T_{i,0} = 50$ mK, $\Omega_{i,0} = 2\pi \cdot 140$ kHz), at different observation points. The black arrows represent magnitude and direction of the velocity of the phase space points, according to their coordinate on the vertical axis.

phase space distribution will be elongated along q_i . Effectively, the size σ_{q_i} of the state will have expanded.

In the following paragraphs, we briefly describe how to reconstruct the phase space distributions from the data, before showing the experimental results.

2.4.1 Extracting phase and amplitude from the data

As soon as the particle is released from the upper tweezer, it starts its evolution under gravitational acceleration with an initial displacement $q_{i,0}$ and velocity $v_{i,0}$ which depend on the phase ϕ_0 and amplitude r_0 of the oscillation at the moment of release. Similarly, as soon as the particle is recaptured it starts oscillating in the new trapping potential, with ϕ_τ and r_τ now depending on the final values of $q_i(\tau)$ and $v_i(\tau)$ reached after the evolution (Eqs. 2.3 and 2.2). To reconstruct the phase space distributions before release and just before recapture, we extract amplitude and phase of the COM modes from the timetraces. In the following, we explain our procedure for the reconstruction of phase space before release of the nanoparticle.

First, we identify the part of each timetrace that contains information on the COM's oscillation just before release. For this analysis we use only the last 5 ms recorded before the detector becomes blind. We refer to this signal as

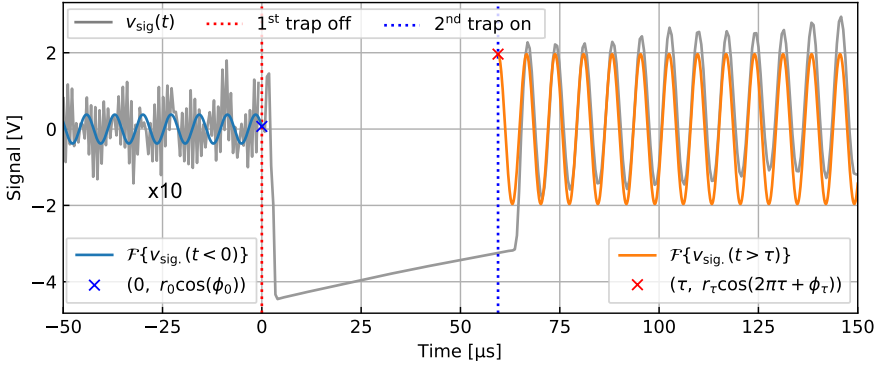


Figure 2.21: Example of a filtered timetrace, where we use a bandpass filter to extract information on phase and amplitude of the particle’s COM oscillations at release and recapture. The portion of the timetrace recorded at $t < 0$ has been multiplied by a factor of 10 to make it more visible.

$v_{\text{sig.}}(t)$. We calculate the PSD of the trace, and find the exact eigenfrequency $\Omega_{i,0}$ for each mode. We demodulate $v_{\text{sig.}}(t)$ around the carrier frequency $\Omega_{i,0}$ by mixing it in postprocessing with a unit amplitude tone at $\Omega_{i,0}$. We then filter the mixed signal with a first order lowpass Butterworth filter. The output of this process are the quadratures I and Q of the filtered signal, $v_{\text{filt.}}(t)$, which can be reconstructed considering that

$$v_{\text{filt.}}(t) = \mathcal{F}(v_{\text{sig.}}(t)) = I + iQ, \quad (2.32)$$

where \mathcal{F} denotes the full filtering process, and i is the imaginary unit.

We retrieve phase and amplitude of the signal from the quadratures I and Q simply considering that

$$\begin{aligned} \phi_0 &= \tan^{-1}(Q/I), \\ r_0 &= 2\sqrt{I^2 + Q^2}. \end{aligned} \quad (2.33)$$

Here, the factor of 2 is needed because our filter erases the information on the negative frequencies.

The post-processing of the data is completely done in Python. We use the Scipy library to create a Butterworth filter, setting as parameters its order, center frequency and BW. We work with first order filters, and tailor the cutoff frequency case by case. Usually, we need a BW between 1 kHz and 2 kHz to

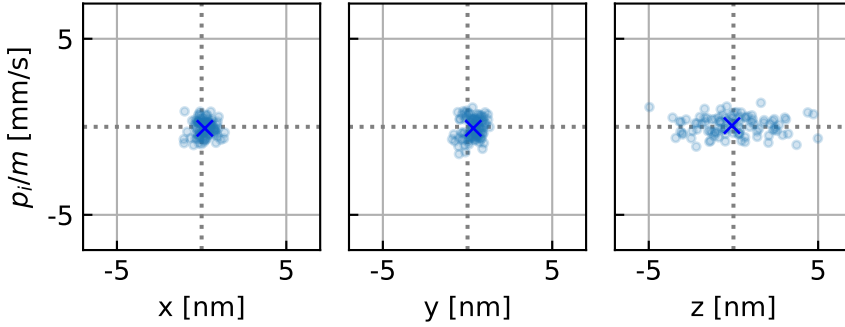


Figure 2.22: Phase space reconstruction of the cooled COM modes before release, at $t = 0$. The axes are converted to displacement and velocity units by using the factor c in Tab. 2.1. Compared to x and y , the phase space reconstruction for the z mode looks larger along the position axis. This is due to the lower eigenfrequency $\Omega_{z,0} = 2\pi \cdot 40.6(1)$ kHz, compared to $\Omega_{x,0} = 2\pi \cdot 116.6(1)$ kHz and $\Omega_{y,0} = 2\pi \cdot 141.6(1)$ kHz.

optimize the filtering for the x and y COM mode signals, while the z mode requires a narrower BW between 50 Hz and 100 Hz. Once r and ϕ are known, we find the phase space coordinates of each realization of the experiment by noting that, for harmonic motion, at $t = 0$ we have

$$\begin{aligned} q_i &= r_0 \cos(\phi_0)/c, \\ p_i &= \dot{q}_i m = -r_0 m \Omega_{i,0} \sin(\phi_0)/c, \end{aligned} \quad (2.34)$$

where m is the mass of the particle, $\Omega_{i,0}$ the eigenfrequency of the mode along axis i and c (in V/m) the calibration factor that converts our signals from volts to meters (see Tab. 2.1).

In Fig. 2.22 we show the reconstructed phase space of the cooled COM modes at $t = 0$, where each point represents one of the hundred realizations. Here the position frame of reference is centered on the first tweezer. As expected, the states lay roughly around the origin of the frame. The spread of each state is proportional to the standard deviation along the relative axis (i.e., the initialization temperature $T_{i,0}$).

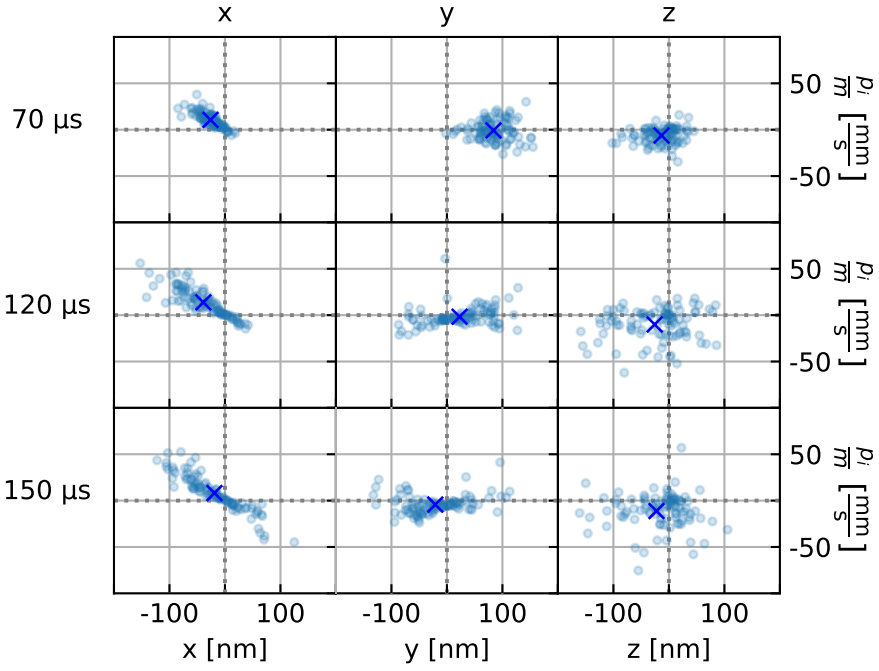


Figure 2.23: Phase space reconstruction of the thermal state at recapture, for a particle dropped between traps separated by $-89(3)$ nm ($\Delta f_{\text{AOM}} = 1$ MHz). The center of the $\mathcal{P}(q_y)$ distribution at $\tau \approx 120$ μs (optimal recapture time, as seen in Fig. 2.16) lies above the origin of the trap, as predicted by Eq. 2.25.

2.4.2 Phase space reconstruction after the free evolution

The reconstruction of the phase space distributions just before recapture requires some extra care. Due to saturation of the QPD's amplification electronics, the first few microseconds of recorded data are distorted (Fig. 2.15) and cannot be used to directly recover information on the particle's motion. We exploit the part of the timetrace that is not corrupted by the electronic artefacts to perform a retrodiction process, back propagating the signal in time until τ , to reconstruct the unreadable parts of the trace and infer from them r and ϕ at τ .

To do so, we apply the Butterworth filter on the time-reversed demodulated quadratures I and Q , which we then back-propagate in time until τ . We reverse the demodulated signal in time again, and obtain ϕ_τ , r_τ , $q_i(\tau)$ and $v_i(\tau)$ according to Eqs. 2.33 and 2.34.

Fig. 2.23 shows the experimental reconstructions of $\mathcal{P}(q_i)$ and $\mathcal{P}(p_i/m)$ at recapture as a function of free evolution time, for all three COM modes. The blue crosses indicate the center of each distribution. We are "looking" at the particle from the second tweezer's reference frame, so the origin of phase space is now coincident with the center of the recapturing trap.

As expected, the reconstructed distributions for the z and x mode stay roughly centered on the same point during the evolution, since the particle's COM is not subjected to any acceleration along these axes. The phase space distribution of the x mode also shows increasing levels of squeezing for longer free fall times, as the points lying at the extremities of the $\mathcal{P}(p_i/m)$ distribution increase their displacement linearly in time. We note that points with positive velocities seem to move towards the negative x axis. This effect can be attributed to a phase delay of the x QPD signal, different with respect to the y channel, which rotates the distribution in phase space with an angle proportional to the delay. Looking at the evolution of the distributions reconstructed for the z axis, it is more difficult to unambiguously infer the squeezing effect, also due to the low SNR for this mode. As expected though, as the time increases, the distributions expand.

Along the y axis, for increasing τ the mean displacement changes from positive to negative values, meaning from above to below the center of the recapturing trap.

	x	y	z
$q'_{i,0}$ [nm]	-27(5)	113 (11)	11(3)
g_i [m/s ²]	0.0(7)	-12(1)	0.0(6)

Table 2.5: Fit results of the parameters defining the phase space trajectories of the x , y and z COM mode. Here $q'_{i,0}$ is measured from the center of the recapturing trap.

In Fig. 2.24 we plot the behavior of the mean μ_{q_i} of $\mathcal{P}(q_i)$ as a function of τ . The black dotted lines are fits of the data according to the model of uniformly accelerated motion

$$\mu_{q_i} \approx q'_{i,0} + \frac{1}{2}g_i\tau^2. \quad (2.35)$$

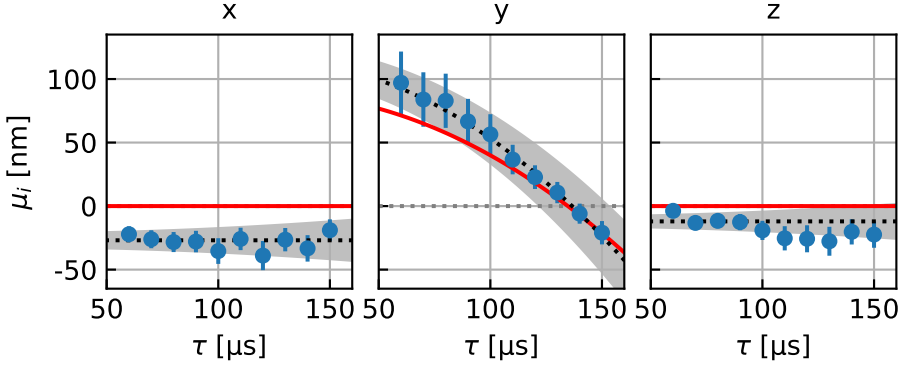


Figure 2.24: Evolution of the mean μ_{q_i} of $\mathcal{P}(q_i)$, as a function of free fall time, for a trap separation of $-89(3)$ nm ($\Delta f_{\text{AOM}} = 1$ MHz). The error bars represent the unbiased standard error calculated over the one hundred samples. The red curves are theory model trends (Eq. 2.35), evaluated assuming $\mathbf{q}'_0 = (0, 89, 0)$ nm, and $\mathbf{g} = (0, -9.81, 0)$ m/s². In black dotted lines, we fit the data to the model with \mathbf{q}'_0 and \mathbf{g} as fit parameters. Along the y axis, the center of the distributions behave congruently with uniformly accelerated motion. Along z and x , the center of the distributions are offset from the origin of the recapturing trap.

Here $q'_{i,0} \neq 0$ is the initial average position measured from the center of the recapturing trap. We fitted the trajectories of all three COM modes leaving $q'_{i,0}$ and g_i as fit parameters, and present the results in Tab. 2.5. The grey shaded areas picture the interval defined by Eq. 2.35 from the fit results and their associated errors. The red traces represent the expected behavior of the distributions in time, according to our model, assuming $\mathbf{q}'_0 = (0, 89, 0)$ nm, and $\mathbf{g} = (0, -9.81, 0)$ m/s².

The evolution of the y COM mode shows the clear signature of an acceleration acting along the axis. The nanoparticle crosses the center of the recapturing trap at $t = 136(5)$ μ s.

Along z and x we observe an offset of the center of the distributions with respect to the trap origin, respectively by $11(3)$ nm, and $-27(5)$ nm. Along the x axis, this indicates that the displaced tweezer is moving diagonally in the laboratory frame of reference. Along z , the effect indicates a shift of the focus' position along the beam propagation axis. The displacement seems to depend on the recapture time, so we speculate it might be due to drifts of the lens' temperature during the protocol, which would affect the diffraction index of the glass and thus the lens' effective focal length.

2.5 State expansion as a function of free evolution time

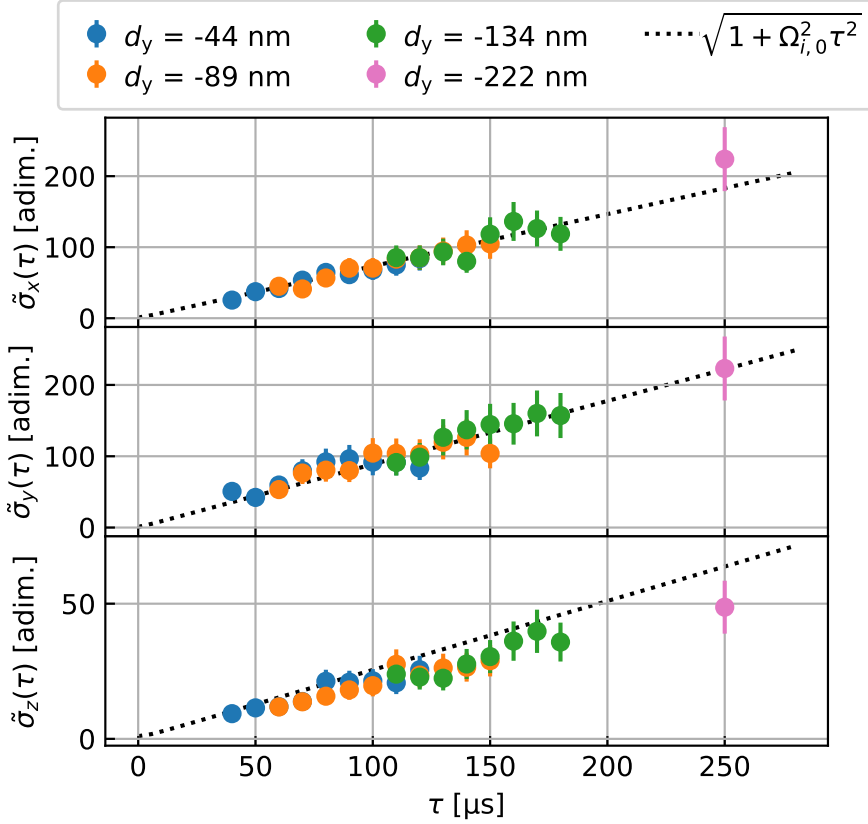


Figure 2.25: Evolution of $\sigma_{q_i}(\tau)$, for all three axis, normalized by the initial state width $\sigma_{q_i}(0)$. The dotted black lines are free parameter theory curves for the expected trend, in Eq. 2.36.

We now analyze how the standard deviation of $\mathcal{P}(q_i)$ evolves as a function of τ . In Section 2.1.1 we have seen that for $\gamma \rightarrow 0$ we expect σ_{q_i} to evolve linearly in time, according to the square root of the initial second moment of velocity $\langle v_{q_i}^2(0) \rangle = \Omega_{i,0}^2 \langle \sigma_{q_i}^2(0) \rangle$. We are interested in the ratio $\tilde{\sigma}_{q_i}(\tau)$ between

the standard deviation of $\mathcal{P}(q_i)$ at release time $t = 0$, and at τ :

$$\begin{aligned}\tilde{\sigma}_{q_i}(\tau) &= \frac{\sigma_{q_i}(\tau)}{\sigma_{q_i}(0)} \approx \sqrt{1 + \frac{\langle v_{i,0}^2 \rangle}{\sigma_{q_i}^2(0)} \tau^2} \\ &= \sqrt{1 + \Omega_{i,0}^2 \tau^2}.\end{aligned}\tag{2.36}$$

Note how a stiffer potential implies a faster expansion, because of the higher $\Omega_{i,0}^2$.

In Fig. 2.25 we plot the ratios between the horizontal projections $\sigma_{q_i}(\tau)$ and $\sigma_{q_i}(0)$ of the reconstructed phase space distributions, representing the standard deviations of $\mathcal{P}(q_i)$ at recapture time and before release.

The blue, orange and green data are extrapolated from the three datasets presented earlier. The pink data point is the average over 100 free evolutions realized with a different nanoparticle, for which we increased both the tweezer displacement ($\Delta f_{\text{AOM}} = 2.5$ MHz, for 222 nm of tweezer separation) and free fall time (250 μs).

The error bars are the total error evaluated from the propagation of the uncertainties on $\sigma_{q_i}(\tau)$ and $\sigma_{q_i}(0)$, which we calculate as the standard deviation itself multiplied by $\sqrt{2/(100 - 1)}$.

The black dotted lines are our model, from Eq. 2.36. The eigenfrequencies depend on the laser power and the particle's density. The power is constant for all acquisitions, and we assume the two particles have identical density, since they come from the same supply. We measure $\Omega_{i,0}$ from the data at $t < 0$, and find that each mode's eigenfrequency lies within 1.5% from the average calculated over all sets. In Eq. 2.36 we thus choose $\Omega_{i,0}$ as the average calculated across all four sets.

We see how for all axes $\tilde{\sigma}_{q_i}(\tau)$ grows linearly in time, as expected.

We note that in the back-propagation of the signal until time τ we are not correcting for delays introduced by the electronics and the AOM's response time. We use the properties of harmonic motion to link q_i and p_i (Eq. 2.34), to extrapolate them at the recapture time, so any error δt in the timing will result in a distribution rotated in phase space by an angle $\Omega_{i,0} \delta t$, which is negligible for small δt .

2 Free evolution of a thermal state

Here we extract only the projection of the rotated ellipse along the axis q_i , and not its major axis. Hence, we might be underestimating the state expansion.

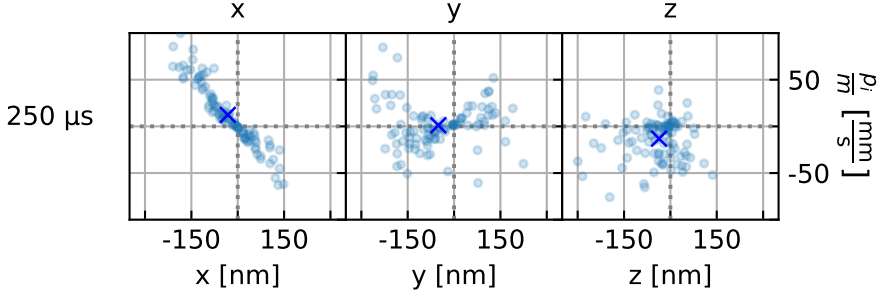


Figure 2.26: Phase space reconstruction of the thermal state at recapture, for a free fall of $250 \mu\text{s}$, between traps separated by -222 nm .

t [μs]	$\sigma_x(t)$ [nm]	$\sigma_y(t)$ [nm]	$\sigma_z(t)$ [nm]
0	0.38(5)	0.51(7)	1.9(3)
250	86(12)	115(16)	93(13)
$\bar{\sigma}_{q_i}(250 \mu\text{s})$ [adim.]	224(45)	223(45)	49(10)

Table 2.6: Standard deviation of the thermal state as a function of free evolution time, extracted for all COM modes at release time $t = 0$, and after a free evolution time of $250 \mu\text{s}$.

Now we focus on the analysis of the expansion rate along the different axes. Compared to the y and x axes, the expansion along z is much smaller, with $\bar{\sigma}_z(250 \mu\text{s}) = 49(10)$. This is due to the lower eigenfrequency of the COM mode along the axis of propagation of the laser, where the confining potential has a larger waist.

Along the y axis instead, just before releasing the particle from the confining potential, the width of the thermal state is $\sigma_y(0) = 0.51(7) \text{ nm}$. From the data we extract $\sigma_y(250 \mu\text{s}) = 115(16) \text{ nm}$. We thus achieved an expansion for the thermal state along the y axis of a factor $\bar{\sigma}_y(250 \mu\text{s}) = 223(45)$.

Similarly, along the x axis we measure $\sigma_x(0) = 0.38(5) \text{ nm}$ before release, and $\sigma_x(250 \mu\text{s}) = 86(12) \text{ nm}$ at $\tau = 250 \mu\text{s}$, indicating an expansion factor of

224(45).

We thus experimentally realized a free fall expansion of a thermal state by more than two-hundred-fold its initial size. In Tab. 2.6 we summarize our findings for all three axis.

2.6 On the scalability of the setup

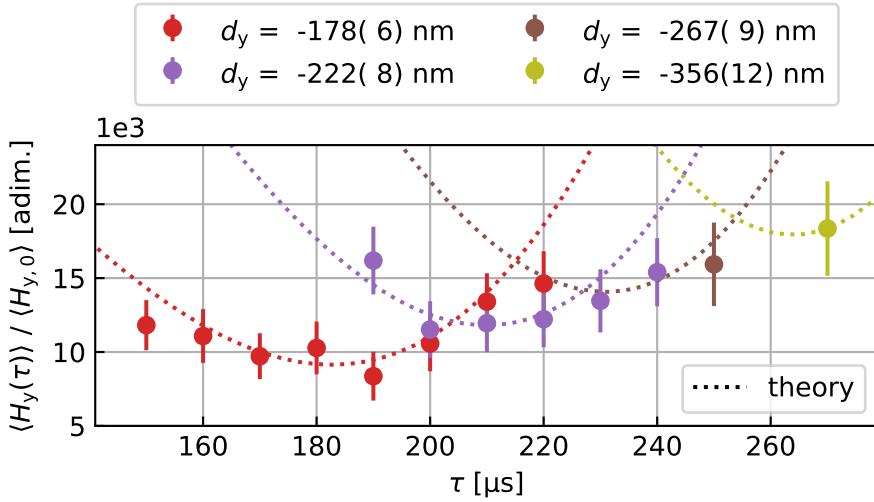


Figure 2.27: Energy of the y COM mode at recapture measured for free falls up to 270 μs , and trap displacements up to 356 nm. The datasets were acquired with three different particles. The dotted lines are free parameter theory curves, assuming an initial temperature of 10 mK. The error bars represent the unbiased sample error calculated over the $N < 50$ samples of each set.

Here we show some of the data that we did not include in our previous analysis. In Fig. 2.27 we plot the normalized y COM mode energy at recapture (Eq. 2.31) measured for four datasets acquired with different nanoparticles. We tuned the tweezers' displacement from 178 nm to 356 nm, achieving a record free fall time of 270 μs .

The dotted lines are not fits, but free parameter curves calculated from Eq. 2.31, assuming an initial temperature of 10 mK, and a scaling factor $A = 0.7$.

The datasets are omitted from the previous sections because for each

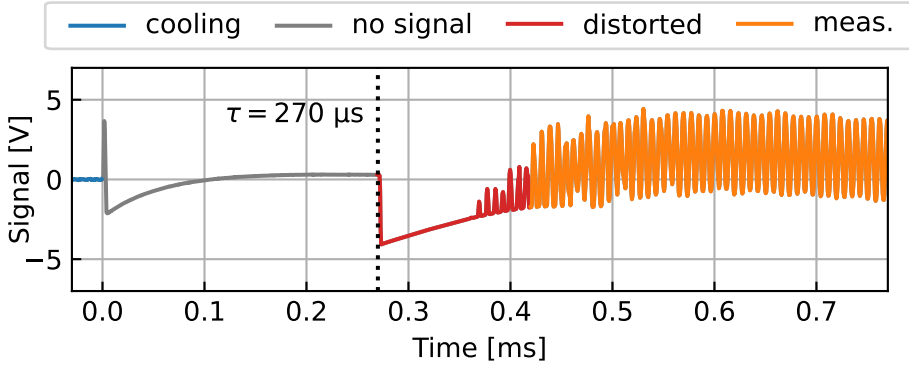


Figure 2.28: QPD y signal of a $270 \mu\text{s}$ free fall. We use different colors to highlight the various sections of the timetrace, according to what described in Sec. 2.3.3.

configuration of d_y and τ we could complete only between thirty and fifty repetitions, due to failure of the PFC. The particles were recaptured each time, but heated out of the trap by the unlocked PLLs. In the future, we plan on using linear feedback cooling, which according to our experience is more resistant to sudden frequency shifts due to the higher bandwidth of the filter. The particle has no charge, so we will deliver the feedback by adding a secondary laser beam, to apply the viscous force by tuning the radiation pressure acting on the particle [69, 70].

For the longer free falls we observed saturation of the detector output. As the oscillation amplitude of the particle increases, the detection becomes non linear. In some cases the voltage signal saturates the output, resulting in a clipped timetrace. This leads to an underestimation of $\langle q_i^2(\tau) \rangle$, making the data unusable for our analysis.

We plan on upgrading the detector to one with a higher dynamic range.

As of today, the PLL performance and the dynamic range of the detector are the two factors that constrain the repeatability of our protocol. Nevertheless, the data in Fig. 2.27 shows how our platform is scalable to a wide range of configurations, allowing us to drop and recapture the nanoparticle over a distance more than three times its diameter.

2.7 Conclusions

To summarize, with this project we developed a platform for the study of free state evolutions with a femtogram nanoparticle, with a mass over 10^9 AMU.

With our experimental protocol based on the release and recapture of a neutral nanoparticle between separated optical tweezers, we let a thermal state evolve in absence of confining potentials, accelerated by gravity across distances bigger than the particle's dimensions, and for timescales up to 270 μs .

More importantly, our platform fulfills the condition of making such free evolution protocols controllable and repeatable with the same particle. This is of utmost importance to test quantum protocols with levitated nanoparticles, as each one is unique, therefore imposing that all repetitions of the experiment necessary for statistical verification must be done with the same object.

As of today, the maximum achievable free evolution time is limited by the performance of the parametric feedback cooling. Longer evolution times mean higher energies at recapture. The consequent redshift of the COM eigenfrequencies challenges the PLL's limited bandwidth, causing it to lose lock, and heating the particle out of the trap. In the future, we plan on implementing a linear feedback cooling scheme, to take advantage of the higher bandwidth around the eigenfrequencies, and increase the reliability of the cooling at recapture.

With respect to what has been achieved up until today in the levitodynamics community [21], one advantage of our system is that the state expansion is unbounded. We experimentally demonstrate that the evolution happens linearly in time, and calculate an expansion factor of 223(45) of the y COM mode for a free evolution of 250 μs . To our knowledge, it is the first time that such a state expansion factor has been realized with femtogram levitated masses, on sub-millisecond timescales.

The combination of all these factors makes our platform a viable candidate for the experimental realization of large quantum state expansions with massive levitated objects.

3

Levitated optomechanics for coherent state expansion

Our work demonstrates how levitated optomechanics is a promising platform for the realization of big delocalized states with massive objects, due to its excellent versatility and low-dissipation properties.

In particular we discussed two settings that highlight the capabilities of levitated systems.

In Chapter 1 we demonstrated how to bring a silica nanoparticle ($> 10^9$ AMU) to the quantum regime, by trapping it in a cryogenic environment and cooling one of its COM modes below single phonon occupation, exerting active control on its motion derived from a high-efficiency measurement.

In Chapter 2 we answered the necessity of working in absence of confining potentials, to achieve arbitrarily large state expansions in absence of photon recoil. We did so by taking advantage of the action of gravitational acceleration, and letting a nanoparticle with zero net charge free fall between separated intermittent tweezers. We experimentally verified the expansion of a thermal state up to a factor of 224(45) during the free fall, and proved a high level of controllability and repeatability of the experiment.

The natural evolution of this work is to combine the two projects together, and experimentally conduct free evolution protocols with a nanoparticle cooled to its ground state, in free fall between displaced tweezers.

Compared to other platforms, which rely on Coulomb interaction to keep the nanoparticle in a confined volume during the evolution, working with neutral objects has the intrinsic advantage of being insensitive to stray electric fields.

One point to address is how to efficiently cool a neutrally charged nanoparticle to the quantum regime. To this end, we stress that parametric feedback is delivered through light intensity modulations, and acts independently of the particle's charge. Mean occupations below 100 phonons have already been reported in the past [31, 43].

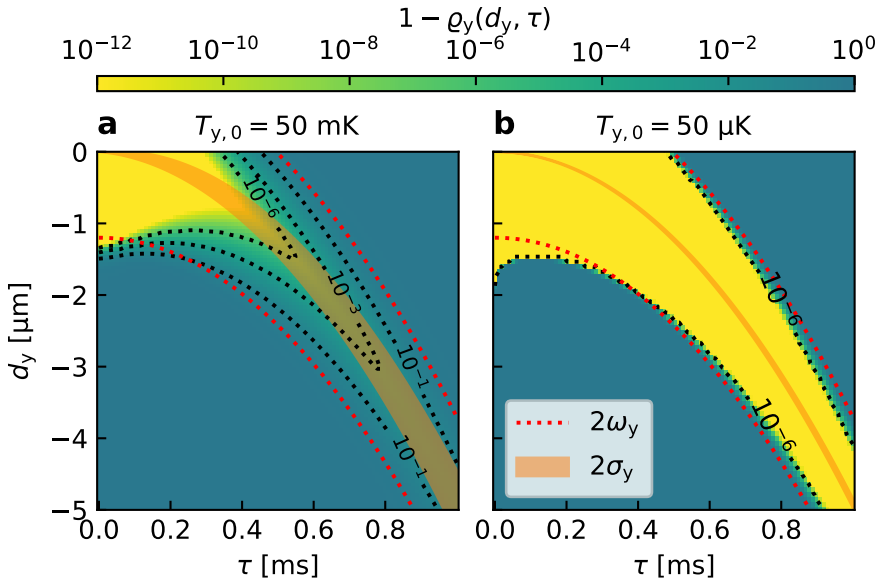


Figure 3.1: Loss probability $1 - \rho_y$ as a function of trap displacement d_y and free fall time τ . Comparison between (a) our experiment, in which $T_y = 50 \text{ mK}$, and (b) a case-study in which a nanoparticle is cooled to $50 \mu\text{K}$. The red dotted line indicates an interval of two time the trap's waist ω_y from the particle's average position (μ_q , Eq. 2.9). The orange shadowed area represents the state's expansion as a function of free evolution time. See Sections 2.1.2 and 2.1.3 for more details.

Nevertheless, linear feedback cooling is the more efficient tool for reaching

single digit phonon populations. In our work, we demonstrated ground-state cooling of a charged nanoparticle through the use of an electric linear feedback, but cold damping can also be applied through optical fields, without recurring to Coulomb interaction. The feedback is delivered either by moving the tweezer's focus, inducing a linear force on the particle [71], or through the modulation of radiation pressure with the introduction of additional laser beams [69, 70].

Initializing the particle's COM in lower mean phonon occupations would dramatically increase the parameter domain in which a free fall protocol could in principle be operated with high repeatability, as we show in Fig. 3.1.

Here, we illustrate the loss probability for experiments conducted with a particle cooled to 50 mK, and 50 μ K, for trap displacements up to 5 μ m, and free evolutions times up to 1 ms. From our calculations, the lower initial COM temperature, corresponding to ~ 10 phonons of mean occupation, would grant high repetition rate (1 particle lost every billion realizations) even for 1 ms free falls. In red dotted lines we delimit an area twice as wide as the trap, centered around the average position of the free falling particle. In orange we picture the expansion of the state. A higher initial temperature determines a faster state expansion (Eq. 2.10), which in turn limits the maximum achievable evolution time due to the limitations on the system's total potential energy imposed by the trap's characteristics.

In the future, we envision working with a setup that combines the detection efficiency and decoherence properties of our cryogenic system, together with the high level of control over the tweezers' power and position of our room-temperature system.

We would still use an AOM (or a deflector) to control the trap's coordinates, and adopt a backscattering detection scheme to improve the efficiency of the measurement. We expect a better SNR compared to forward detection, by avoiding the need to attenuate the signal due to the intense LO (> 100 mW).

Similar to what we do now in forward detection, we would use a telescope to image the fields onto the detector, keeping the signals centered on its diodes regardless of beam orientation. The measured signal would then be used to create the light-activated active feedback for state initialization.

The use of a cryostat, although susceptible to higher mechanical noise, is useful to limit decoherence due to interactions with residual gas molecules, and blackbody radiation emission.

We can think of minimizing the time for which the optical trap is on, to maintain the internal temperature of the nanosphere in equilibrium with the surrounding cryogenic environment. Assuming the particle's environment to be equilibrated at 60 K, and at a pressure of 10^{-12} mbar, well within the reach of state-of-the-art cryostats [72], we estimate a coherent evolution time of around 50 ms [5].

For a conservative estimation, let us constrain ourselves to 1 ms of evolution. Starting from the ground state, with $y_{\text{zpf}} \approx 10$ pm, in 1 ms we could expand the state by a factor 880, to 8.8 nm.

Considering the scalability of our system, we are confident that the parameter range of operation of our setup could be expanded in the future, to achieve free evolutions even longer than 1 ms. A free fall of 10 ms would be sufficient to coherently expand the wave function up to a size comparable with the nanosphere itself, bringing the exploration of macroscopic quantum effects within experimental reach.

This outlook is partially based on the publication [3].



Design of the mechanical components

This section is partially based on the supplementary information to the publication [3].

Both experiments presented in this work require highly specialized setups. During the development of each project, custom mechanical parts were designed and manufactured ad hoc to accommodate the needs of the experiments, whether they be related to vacuum compatibility, mechanical stability, thermal performance etc.

In the following sections, we will give more details on the fabrication of some of the mechanical elements. We tried to engineer solutions which would be easiest to manufacture, and most cost-effective, while still satisfying all of the necessary specifications. All parts are also designed with ease of use (and replacement) in mind.

A.1 Lens mounts

The trapping lens of our choice for both projects is the C-coated LightPath 355617, due to its high NA of 0.75. The lens is sold bare, without any enclosure. It has a relatively small form factor, with just 1.4 mm of diameter and less

than 1 mm of thickness. In both experiments, we also use a collecting lens (LightPath, model 355330, C coated), with a lower NA of 0.6 at 1064 nm wavelength, and bigger dimensions (6.3 mm diameter, 2.7 mm thickness). This model is sold already glued in a steel enclosure, with a M9×0.5 thread.

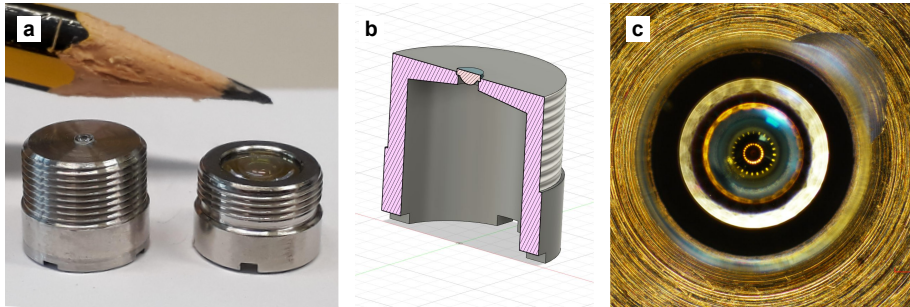


Figure A.1: **a.** Trapping (left) and collimating (right) lenses, installed in their respective metal casings. **b.** Section view of the custom mount for the trapping lens. On the top flat surface, a round aperture with a ledge allows the lens to be dropped in, with the curved surface facing the inside of the mount. **c.** Dark field image of the trapping lens glued to the mount. The microscope is focused on the ledge of the aperture, to check if the lens is centered. In the top right corner, a drop of glue keeps the lens in place.

We designed a custom casing to mount the trapping lens in our setup, which allows us to also easily tune its distance from the collecting lens, hence increasing the performance of our forward detection by maximising the light collimated outside the chamber.

The mount (in Fig. A.1b) is of stainless steel. It features a 8 mm body with M9×0.5 threading. The trapping lens rests above a circular ledge milled around an aperture in the top flat surface of the mount. The lens is then secured in place with a drop of vacuum-compatible glue¹. The gluing process is performed under the microscope, to ensure that the lens is concentric with the mount.

The choice of the material is functional to the experiment. We drive the levitated nanoparticle's motion with electrical signals: since the lens mounts are made of conductive metal, we tape the electrodes directly on them. The closeness of the mounts' surfaces to the particle ensures that the resulting electric field is strong enough to drive the particle's motion.

¹Norland Optical Adhesive 83H

A.2 Trap couplers

Once the lenses are glued on a proper mount, we position them at the right distance to each other by screwing them in a trap coupler, and then fix them inside the vacuum chambers.

The two projects required the design of different trap couplers, but key characteristics are common to both. In fact, we need a trap holder that:

- ensures the two lenses are well co-aligned;
- allows to easily tune the distance between the lenses;
- is made of a non-conductive, vacuum-compatible material;
- is stable, both against mechanical vibrations and temperature fluctuations;
- has an access port for the nebulized particles to reach the trapping volume.

The couplers are made of polyether ether ketone (PEEK), a plastic material easily machinable, and with enough chemical and thermal stability for our applications. A horizontal bore with M9×0.5 threading accepts the two lenses, each screwed in from either side of the coupler. This design grants the co-alignment of the lenses, and allows fine adjustments of their relative distance, while a tight thread clearance prevents accidental movements. On the top of each holder, a 4 mm vertical channel is cut out to allow access to the volume between the two lenses. Here the nebulized particles can be dropped, and trapped. Both trap holders were machined by the D-ITET Workshop² of ETH Zurich.

A.3 Cryostat 4 K shield

The vacuum chamber of the cryostat setup is divided in three main volumes, each delimited by a "shield". With this term, we refer to a metal casing which is thermalized at a specific temperature, and blocks "hot" molecules from reaching the inner volume of the cryogenic chamber. The most external shield (which we call "the 300 K" shield) is simply provided by the vacuum chamber³, which

²<https://werkstatt.ee.ethz.ch/en/>

³Kimball Physics, model MCF800-ExtOct-G2C8

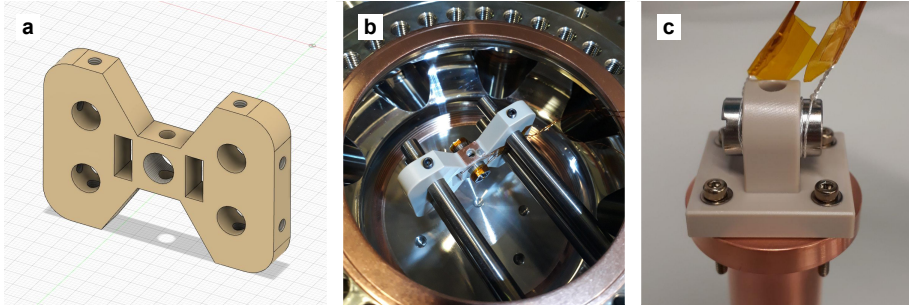


Figure A.2: **a.** 3D model of the lens coupler for the second project. **b.** Lens coupler installed in the chamber, fitted with lenses and electrodes. Initially, we had prepared the assembly with six electrodes, two for each axis of motion, so that electrical tones could drive the particle from all directions. **c.** Lens coupler for the cryogenic setup, mounted on a solid copper post to ensure good thermal contact with the cold plate of the cryostat.

fully encloses the cold breadboard of the cryostat⁴.

The cold breadboard itself sits flush with the table, and comprises of two stages: an innermost round 4 K plate, surrounded by the outermost 40 K base. On top of this external base we screw the "40 K shield", a cylinder made of aluminum, closed at the top with a removable lid. The innermost volume is

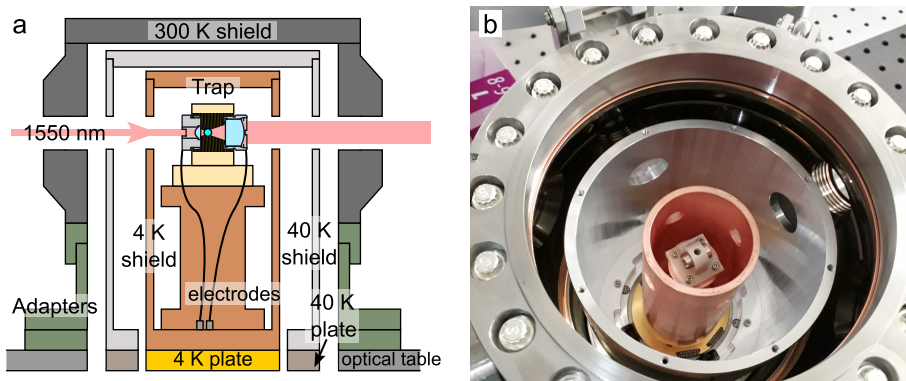


Figure A.3: Section (a) and top (b) view of the cryostat vacuum chamber, with the shields and trap assembly positioned in place (here seen before installation of the electrodes for linear feedback cooling).

protected by the 4 K shield, also cylindrical, but manufactured out of oxide-free copper. The 4 K shield's base is in direct thermal contact with the cold plate

⁴attocube attoDRY800

of the cryostat. At the top, the shield is closed with a removable lid. Four perpendicular round cut outs allow optical access to the inside of the volume. Here is where the trap sits, fastened on top of a cylindrical post also made of oxide-free copper.

The shields block blackbody radiation from the external environment, and help achieving low pressures inside the innermost volume through the cryopumping effect. As the temperatures drop below 60 K, residual molecules in the chamber stick and freeze onto the metal surfaces. At the 300 K shield we read pressures of $\sim 1 \times 10^{-9}$ mbar. We estimate that the pressure at the core of the assembly should be lower by several orders of magnitude [72].

B

Detailed solution to the Langevin Equation

In this section, we present in more detail the calculations that lead to the equations in Sections 2.1.1 and 2.1.4.

B.1 Velocity as a function of time

We start considering the equation of motion of the nanoparticle's COM. At time $t = 0$ we switch off the optical trap. The equation of motion along a generic axis y reads:

$$\ddot{y}(t) + \gamma\dot{y}(t) = g_y + \eta(t), \quad (\text{B.1})$$

in which g_y is the acceleration along the considered axis, γ is the damping due to gas interactions, and $\eta(t) = F(t)/m$ is a Gaussian distributed white noise, proportional to the fluctuating force $F(t)$ acting on a particle of mass m . Its magnitude f is given by the autocorrelation function $\langle \eta_i(t)\eta_i(t+t') \rangle = f\delta(t')$. It is linked to the damping rate γ by the fluctuation-dissipation theorem: $f = 2\gamma k_B T_{\text{gas}}/m$ in (one-dimensional case) [60].

We solve to equation for \dot{y} by observing that

$$\frac{d}{dt} (e^{\gamma t} \dot{y}(t)) = e^{\gamma t} (\ddot{y}(t) + \gamma\dot{y}(t)). \quad (\text{B.2})$$

We use this relation to solve Eq. B.1 for the velocity, by multiplying the terms by $e^{\gamma t}$, then rearranging them and integrating in time domain:

$$\begin{aligned}
 \frac{d}{dt}(e^{\gamma t} \dot{y}(t)) &= e^{\gamma t} (g_y + \eta(t)) \\
 \int_0^t \frac{d}{dt}(e^{\gamma t} \dot{y}(t)) dt &= \int_0^t g_y e^{\gamma t} + e^{\gamma t} \eta(t) dt \\
 \dot{y}(t) e^{\gamma t} - \dot{y}_0 &= g_y \frac{1}{\gamma} (e^{\gamma t} - 1) + \int_0^t e^{\gamma t} \eta(t) dt \\
 \dot{y}(t) &= \dot{y}_0 e^{-\gamma t} + \frac{g_y}{\gamma} (1 - e^{-\gamma t}) + \int_0^t e^{-\gamma(t-t')} \eta(t') dt'.
 \end{aligned} \tag{B.3}$$

Taking the average of the result of Eq. B.3, we find that a particle subjected to a free fall for a time t , will have average velocity $\langle \dot{y}(t) \rangle$

$$\langle \dot{y}(t) \rangle = \langle \dot{y}_0 \rangle e^{-\gamma t} + \frac{g_y}{\gamma} (1 - e^{-\gamma t}). \tag{B.4}$$

For $t \rightarrow \infty$, we see that the dominating contribution is the one due to the acceleration g_y . Thus, for a free particle moving of Brownian motion, the mean velocity is null [73]. We also want to calculate the variance of this quantity, as $\sigma_y^2 = \langle \dot{y}^2(t) \rangle - \langle \dot{y}(t) \rangle^2$. We first evaluate $\langle \dot{y}^2(t) \rangle$. To simplify the notation, we write

$$\begin{aligned}
 A &= \dot{y}_0 e^{-\gamma t} + \frac{g_y}{\gamma} (1 - e^{-\gamma t}) \\
 B &= \int_0^t e^{-\gamma(t-t')} \eta(t') dt' \\
 \langle \dot{y}^2(t) \rangle &= \langle A^2 + B^2 + 2AB \rangle = \langle A^2 \rangle + \langle B^2 \rangle + \langle 2AB \rangle.
 \end{aligned} \tag{B.5}$$

We first focus on the term $\langle A^2 \rangle$:

$$\begin{aligned}
 \langle A^2 \rangle &= \left\langle \left[\dot{y}_0 e^{-\gamma t} + \frac{g_y}{\gamma} (1 - e^{-\gamma t}) \right]^2 \right\rangle \\
 &= \langle \dot{y}_0^2 \rangle e^{-2\gamma t} + \frac{g_y^2}{\gamma^2} (1 - e^{-\gamma t})^2 + 2g_y \frac{\langle \dot{y}_0 \rangle}{\gamma} e^{-\gamma t} (1 - e^{-\gamma t}).
 \end{aligned} \tag{B.6}$$

B Detailed solution to the Langevin Equation

We now evaluate the time correlation function $\langle B^2 \rangle$:

$$\langle B^2 \rangle = \left\langle \int_0^{t_1} \int_0^{t_2} e^{-\gamma(t-t')} \eta(t') dt' e^{-\gamma(t-t'')} \eta(t'') dt'' \right\rangle \quad (\text{B.7})$$

We move the averaging sign inside the integral, knowing that $\langle \eta(t') \eta(t'') \rangle = f \delta(t' - t'')$. Hence, the integral is non-zero only if $t' = t''$:

$$\begin{aligned} \langle B^2 \rangle &= f \int_0^{t_1} e^{-2\gamma(t-t')} dt' \\ &= \frac{f}{2\gamma} (1 - e^{-2\gamma t_1}). \end{aligned} \quad (\text{B.8})$$

Finally, we get

$$\begin{aligned} \langle \dot{y}^2(t) \rangle &= \langle A^2 \rangle + \langle B^2 \rangle + \langle 2AB \rangle \\ &= \langle \dot{y}_0^2 \rangle e^{-2\gamma t} + \frac{g_y^2}{\gamma^2} (1 - e^{-\gamma t})^2 + 2g_y \frac{\langle \dot{y}_0 \rangle}{\gamma} e^{-\gamma t} (1 - e^{-\gamma t}) + \\ &\quad + \frac{f}{2\gamma} (1 - e^{-2\gamma t}), \end{aligned} \quad (\text{B.9})$$

recalling that $\langle 2AB \rangle = 0$ because $\langle B \rangle = 0$. As a check, we observe that the behavior over long timescales is

$$\langle \dot{y}^2(t \rightarrow \infty) \rangle \simeq \frac{g_y^2}{\gamma^2} + \frac{f}{2\gamma}. \quad (\text{B.10})$$

The variance of the velocity as a function of time is thus

$$\begin{aligned} \sigma_y^2 &= \langle \dot{y}^2(t) \rangle - \langle \dot{y}(t) \rangle^2 \\ &= \langle \dot{y}_0^2 \rangle e^{-2\gamma t} - \langle \dot{y}_0 \rangle^2 + \frac{f}{2\gamma} (1 - e^{-2\gamma t}). \end{aligned} \quad (\text{B.11})$$

At equilibrium (i.e. over long timescales), we use the equipartition theorem to write

$$\begin{aligned} \sigma_y^2(t \rightarrow \infty) &= \frac{f}{2\gamma} \\ &= \frac{k_B T}{m} \end{aligned} \quad (\text{B.12})$$

from which we find that $f = 2\gamma k_B T/m$ in accordance with the fluctuation dissipation theorem.

B.2 Position as a function of time

We now turn to evaluating the position $y(t)$. We integrate over the velocity, to obtain

$$\begin{aligned}
 y(t) &= y_0 + \int_0^t \dot{y}(t) dt \\
 &= y_0 + \int_0^t \left[\dot{y}_0 e^{-\gamma t} + \frac{g_y}{\gamma} (1 - e^{-\gamma t}) + \int_0^t e^{-\gamma(t-t')} \eta(t') dt' \right] dt \\
 &= y_0 + \frac{\dot{y}_0}{\gamma} (1 - e^{-\gamma t}) + \frac{g_y}{\gamma} t - \frac{g_y}{\gamma^2} (1 - e^{-\gamma t}) + \\
 &\quad + \int_0^t \int_0^t e^{-\gamma(t-t')} \eta(t') dt' dt \\
 &= y_0 + \frac{\dot{y}_0}{\gamma} (1 - e^{-\gamma t}) + \frac{g_y}{\gamma} t - \frac{g_y}{\gamma^2} (1 - e^{-\gamma t}) + \\
 &\quad + \frac{1}{\gamma} \int_0^t \eta(t') (1 - e^{-\gamma(t-t')}) dt'.
 \end{aligned} \tag{B.13}$$

Similar to before, we calculate how the average $\langle y(t) \rangle$ and variance $\sigma_y^2 = \langle y^2(t) \rangle - \langle y(t) \rangle^2$ of the position evolve in time.

$$\langle y(t) \rangle = \langle y_0 \rangle + \frac{\langle \dot{y}_0 \rangle}{\gamma} (1 - e^{-\gamma t}) + \frac{g_y}{\gamma} t - \frac{g_y}{\gamma^2} (1 - e^{-\gamma t}). \tag{B.14}$$

We redefine

$$\begin{aligned}
 A &= y_0 + \frac{\dot{y}_0}{\gamma} (1 - e^{-\gamma t}) + \frac{g_y}{\gamma} t - \frac{g_y}{\gamma^2} (1 - e^{-\gamma t}); \\
 B &= \frac{1}{\gamma} \int_0^t \eta(t') (1 - e^{-\gamma(t-t')}) dt'; \\
 \langle y^2(t) \rangle &= \langle A^2 + B^2 + 2AB \rangle = \langle A^2 \rangle + \langle B^2 \rangle + \langle 2AB \rangle.
 \end{aligned} \tag{B.15}$$

We calculate the non-null contributions $\langle A^2 \rangle$ and $\langle B^2 \rangle$, putting to 0 all terms depending on $\langle y_0 \rangle$:

$$\begin{aligned}
 \langle A^2 \rangle &= \left\langle \left[y_0 + \frac{\dot{y}_0}{\gamma} (1 - e^{-\gamma t}) + \frac{g_y}{\gamma} t - \frac{g_y}{\gamma^2} (1 - e^{-\gamma t}) \right]^2 \right\rangle \\
 &= \left\langle \left[y_0 + \frac{\dot{y}_0}{\gamma} (1 - e^{-\gamma t}) \right]^2 + \left[\frac{g_y}{\gamma} t - \frac{g_y}{\gamma^2} (1 - e^{-\gamma t}) \right]^2 + \right. \\
 &\quad \left. + 2 \left[y_0 + \frac{\dot{y}_0}{\gamma} (1 - e^{-\gamma t}) \right] \left[\frac{g_y}{\gamma} t - \frac{g_y}{\gamma^2} (1 - e^{-\gamma t}) \right] \right\rangle \\
 &= \langle y_0^2 \rangle + \frac{\langle \dot{y}_0^2 \rangle}{\gamma^2} (1 - e^{-\gamma t})^2 + \\
 &\quad + \frac{g_y^2}{\gamma^2} t + \frac{g_y^2}{\gamma^4} (1 - e^{-\gamma t})^2 - 2 \frac{g_y^2}{\gamma^3} t (1 - e^{-\gamma t}) + \\
 &\quad + \frac{2}{\gamma} \langle y_0 \rangle g_y t - \frac{2g_y}{\gamma^2} \langle y_0 \rangle (1 - e^{-\gamma t}); \tag{B.16} \\
 \langle B^2 \rangle &= \left\langle \int_0^t \frac{1}{\gamma} (1 - e^{-\gamma(t-t')}) \eta(t') dt' \int_0^t \frac{1}{\gamma} (1 - e^{-\gamma(t-t'')}) \eta(t'') dt'' \right\rangle \\
 &= \frac{f}{\gamma^2} \int_0^t (1 - e^{-\gamma(t-t')})^2 dt' \\
 &= \frac{f}{\gamma^2} \left[t + \frac{1}{2\gamma} (1 - e^{-2\gamma t}) - \frac{2}{\gamma} (1 - e^{-\gamma t}) \right] \\
 &= \frac{f}{\gamma^2} t - \frac{f}{2\gamma^3} (3 - e^{-\gamma t}) (1 - e^{-\gamma t}).
 \end{aligned}$$

Finally, after taking the square of Eq. B.14, we obtain the variance

$$\sigma_y^2 = \langle y_0^2 \rangle - \langle y_0 \rangle^2 + \frac{\langle \dot{y}_0^2 \rangle}{\gamma^2} (1 - e^{-\gamma t})^2 + \frac{f}{\gamma^2} t - \frac{f}{2\gamma^3} (3 - e^{-\gamma t}) (1 - e^{-\gamma t}). \tag{B.17}$$

Also in this case, we observe that on long timescales [73]

$$\begin{aligned}
 \sigma_y^2(t \rightarrow \infty) &= \langle y_0^2 \rangle + \frac{f}{\gamma^2} t \\
 &\approx \frac{f}{\gamma^2} t = \frac{2k_B T}{m\gamma} t = 2Dt. \tag{B.18}
 \end{aligned}$$

C

Stabilization of the optical trap depth

We perform the free evolutions by implementing a catch-and-release protocol, using an AOM to tilt the trapping beam by driving it with different RF tones. It is important that the depth of the optical trap stays constant while displacing it. Two main factors influence this.

First, the diffraction efficiency of the AOM (which depends on the RF frequency) affects the mean power of the trapping beam. Second, as the beam is tilted, a misalignment from the center of the trapping lens can change the shape of the focused field.

In the following paragraphs we study the stability of the optical trap depth.

The first step is to characterize how the beam power changes as a function of RF tone frequency and amplitude. To analyze this, we sweep the RF signal amplitude while measuring the power of the beams emerging from the AOM, repeating the procedure for different RF frequencies.

In Fig. C.1a we plot an example of the data acquired with this procedure. The curves describe how to change the amplitude of the RF tones as a function of the chosen RF frequency, to stabilize the trapping beam power. Once the relation between RF frequency, amplitude and trap power is known, we trap a

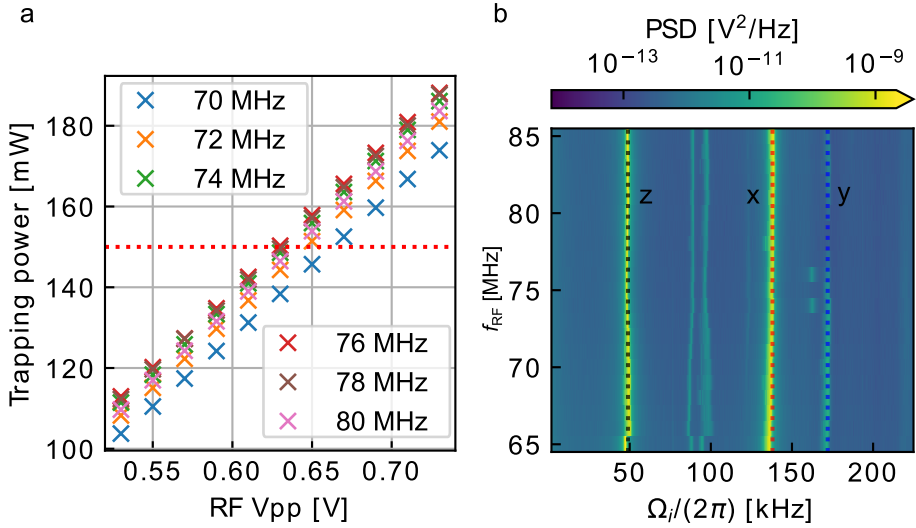


Figure C.1: **a.** Power of the trapping beam as a function of the RF tone frequency and amplitude (for a previous iteration of the setup). At the time, we were working with trapping powers of 150 mW. **b.** Mechanical eigenfrequencies Ω_i as a function of AOM input RF frequency.

particle and sweep the RF tone parameters, while monitoring the stability of the COM eigenfrequencies. The data in Fig. C.1b was acquired with a 177 nm particle, trapped with a 150 mW beam. We swept the RF frequency from 65 MHz to 85 MHz, stabilizing the trapping power according to the curves in Fig. C.1a, and measured an eigenfrequency drift of 4 % across the whole range.

This check also indicates how well the tilted beams stay aligned on the trapping lens. As the particle is dragged up and down with the trap focus, if the imaging telescope (see Fig. 2.8) is well aligned on the CA of the lens, we expect Ω_i to stay constant.

D

Notation

Symbols used in this work, listed by chapter.

Table D.1: List of symbols used in Chapter 1.

Symbol	Description
m	Mass of the particle
Ω_z	Eigenfrequency of the particle along the optical axis
z_{zpf}	Zero-point fluctuation size: $z_{\text{zpf}} = \sqrt{\hbar/(2m\Omega_z)}$
γ_{eff}	Effective feedback-induced mechanical damping rate
γ_{th}	Damping rate due to thermal bath: $\gamma_{\text{th}} \ll \gamma_{\text{eff}}$
T	Bath temperature
Γ_{th}	Thermal decoherence rate (phonons/s): $\Gamma_{\text{th}} = \gamma_{\text{th}} k_B T / (\hbar\Omega_z)$
Γ_{qba}	Decoherence rate due to quantum backaction
Γ_{exc}	Excess decoherence rate including Γ_{th}

Continued on next page

Table D.1: List of symbols used in Chapter 1. (Continued)

Symbol	Description
Γ_{tot}	Total decoherence rate: $\Gamma_{\text{tot}} = \Gamma_{\text{qba}} + \Gamma_{\text{exc}} = \Gamma_{\text{qba}}(1 + 1/C_q)$
C_q	Quantum cooperativity: $C_q = \Gamma_{\text{qba}}/\Gamma_{\text{exc}}$
η_d	Detection efficiency
Γ_{meas}	Measurement rate: $\Gamma_{\text{meas}} = \eta_d \Gamma_{\text{qba}}$
η_{meas}	Measurement efficiency: $\eta_{\text{meas}} = \Gamma_{\text{meas}}/\Gamma_{\text{tot}} = \eta_d/(1 + 1/C_q)$
\bar{n}	Phonon occupation number of the particle's z -motion
$\chi_{\text{eff}}(\Omega)$	Effective mechanical susceptibility: $\chi_{\text{eff}}(\Omega) = m^{-1}/(\Omega_z^2 - \Omega^2 - i\gamma_{\text{eff}}\Omega)$
$\bar{S}_{FF}^{\text{tot}}$	Two-sided, symmetrized total force noise PSD: $\bar{S}_{FF}^{\text{tot}} = \hbar^2 \Gamma_{\text{tot}} / (2\pi z_{\text{zpf}}^2)$
\bar{S}_{imp}	Detector imprecision noise PSD: $\bar{S}_{\text{imp}} = z_{\text{zpf}}^2 / (8\pi \Gamma_{\text{meas}})$
$\bar{S}_{\text{imp}} \bar{S}_{FF}^{\text{tot}}$	Measurement-disturbance relation: $\bar{S}_{\text{imp}} \bar{S}_{FF}^{\text{tot}} = (\hbar/4\pi)^2 / \eta_{\text{meas}}$
$\bar{S}_{zz}(\Omega)$	Two-sided, symmetrized particle position PSD: $\langle z^2 = \rangle \int d\Omega \bar{S}_{zz}(\Omega)$
$\bar{S}_{zz}^{\text{hom}}(\Omega)$	Measured in-loop position PSD on the homodyne detector
$\bar{S}_{rr}(\Omega)$	Heterodyne detector position PSD at the Stokes (red) sideband
$\bar{S}_{bb}(\Omega)$	Heterodyne detector position PSD at the anti-Stokes (blue) sideband
$\bar{S}_{rb}(\Omega)$	Cross-PSD between Stokes and anti-Stokes sidebands

Table D.2: List of symbols used in Chapter 2.

Symbol	Description
m	Mass of the particle
$\Omega_i(t)$	Eigenfrequency of the COM mode along axis $i = x, y, z$, at time t
$\Omega_{i,0}$	Eigenfrequency of the COM mode along axis $i = x, y, z$, at time $t = 0$
τ	Recapture time
P_{gas}	Gas pressure
T_{gas}	Gas bath temperature
γ	Gas damping rate
$T_{i,0}$	Initialization temperature for the COM mode along axis $i = x, y, z$, at time $t = 0$
q_i	Position along axis $i = x, y, z$
v_i	Velocity along axis $i = x, y, z$
p_i	Momentum along axis $i = x, y, z$
$\eta(t)$	Fluctuating force normalized by the mass of the particle: $\eta(t) = F_{\text{fluct}}(t)/m$
f	Magnitude of $\eta(t)$: $f = 2\gamma k_B T_{\text{gas}}/m$
\mathbf{g}	Gravitational acceleration: $\mathbf{g} = (g_x, g_y, g_z) = (0, -g, 0)$
K	Kinetic energy
U	Potential energy
$\langle q_{i,0}^2 \rangle$	Second moment of position at $t = 0$
$\langle v_{i,0}^2 \rangle$	Second moment of velocity at $t = 0$
$\mathcal{P}(q_i)$	Position probability density distribution along axis i
$\mathcal{P}(v_i)$	Velocity probability density distribution along axis $i = x, y, z$

Continued on next page

Table D.2: List of symbols used in Chapter 2. (Continued)

Symbol	Description
$\mathcal{P}(p_i)$	Momentum probability density distribution along axis i : $\mathcal{P}(p_i) = \mathcal{P}(m v_i)$
$\mu_{q_i}(t)$	Mean of $\mathcal{P}(q_i)$
$\mu_{v_i}(t)$	Mean of $\mathcal{P}(v_i)$
$\sigma_{q_i}^2(t)$	Variance of $\mathcal{P}(q_i)$
$\sigma_{v_i}^2(t)$	Variance of $\mathcal{P}(v_i)$
U_0	Trap depth; $U_0 \approx 50 k_B T_{\text{gas}}$
ω_i	Trap waist radius along axis i
\mathbf{d}	Trap displacement: $\mathbf{d} = (d_x, d_y, d_z)$
ρ_i	Recapture probability along axis i
$\mathcal{W}(q_i, p_i)$	Probability of finding a particle in phase space with position q_i and momentum $p_i = m v_i$
$U(q_i - d_i)$	Trapping potential displaced by d_i along axis i
c	Conversion factor, in V/m
$\langle H_i(\tau) \rangle$	Expected average energy of mode i at recapture
$\langle H_{y,\text{min}} \rangle$	Minimum recapture energy
θ_B	Bragg angle
f_1 and f_2	RF frequencies of the AOM driving tones
Δf_{AOM}	Difference between f_1 and f_2
$\tilde{H}_i(\tau)$	Normalized recapture energy: $\tilde{H}_i(\tau) = \langle H_i(\tau) \rangle / \langle H_{i,0} \rangle$
ϕ_0	Phase of the oscillatory motion at $t = 0$
r_0	Amplitude of the oscillatory motion at $t = 0$
ϕ_τ	Phase of the oscillatory motion at $t = \tau$
r_τ	Amplitude of the oscillatory motion at $t = \tau$

Continued on next page

Table D.2: List of symbols used in Chapter 2. (Continued)

Symbol	Description
I and Q	Demodulated, filtered quadratures
$q'_{i,0}$	Initial phase space coordinate along the position domain, calculated from the recapturing trap
$\tilde{\sigma}_{q_i}(\tau)$	Normalized state expansion along axis i at time τ : $\tilde{\sigma}_{q_i}(\tau) = \sigma_{q_i}(\tau)/\sigma_{q_i}(0)$

E

Abbreviations

List of abbreviations used in this work.

Table E.1:

Abbreviation	Description
adim.	Adimensional
a. u.	Arbitrary units
AOM	Acousto-optic modulator
BW	Bandwidth
CA	Clear aperture
CMMR	Common-mode rejection ratio
COM	Center-of-mass
EOM	Electro-optic modulator
FPGA	Field-programmable gate array

Continued on next page

Table E.1: (Continued)

Abbreviation	Description
NA	Numerical aperture
PFC	Parametric feedback cooling
PLL	Phase-locked loop
QPD	Quadrant photodiode
RF	Radio frequency
SNR	Signal-to-noise ratio

References

- [1] U. Delić, M. Reisenbauer, D. Grass, N. Kiesel, V. Vuletić, and M. Aspelmeyer, *Cavity Cooling of a Levitated Nanosphere by Coherent Scattering*, Phys. Rev. Lett. **122**, 123602 (2019).
- [2] U. Delić, M. Reisenbauer, K. Dare, D. Grass, V. Vuletić, N. Kiesel, and M. Aspelmeyer, *Cooling of a levitated nanoparticle to the motional quantum ground state*, Science **367**, 892 (2020).
- [3] F. Tebbenjohanns, M. L. Mattana, M. Rossi, M. Frimmer, and L. Novotny, *Quantum control of a nanoparticle optically levitated in cryogenic free space*, Nature **595**, 378 (2021), doi: 10.1038/s41586-021-03617-w, URL <https://www.nature.com/articles/s41586-021-03617-w>.
- [4] L. Magrini, P. Rosenzweig, C. Bach, A. Deutschmann-Olek, S. G. Hofer, S. Hong, N. Kiesel, A. Kugi, and M. Aspelmeyer, *Real-time optimal quantum control of mechanical motion at room temperature*, Nature **595**, 373 (2021).
- [5] O. Romero-Isart, *Quantum superposition of massive objects and collapse models*, Phys. Rev. A **84**, 052121 (2011).
- [6] C. Gonzalez-Ballester, M. Aspelmeyer, L. Novotny, R. Quidant, and O. Romero-Isart, *Levitodynamics: Levitation and control of microscopic objects in vacuum*, Science **374**, eabg3027 (2021).
- [7] T. Kovachy, P. Asenbaum, C. Overstreet, C. A. Donnelly, S. M. Dickerson, A. Sugarbaker, J. M. Hogan, and M. A. Kasevich, *Quantum superposition at the half-metre scale*, Nature **528**, 530 (2015).
- [8] L. Novotny and B. Hecht, *Principles of nano-optics, 2nd edn.*, Cambridge university press, 2012.
- [9] J. Gieseler, *Dynamics of optically levitated nanoparticles in high vacuum*, PhD thesis, ICFO, 2015.

REFERENCES

- [10] J. D. Teufel, T. Donner, D. Li, J. W. Harlow, M. S. Allman, K. Cicak, A. J. Sirois, J. D. Whittaker, K. W. Lehnert, and R. W. Simmonds, *Sideband cooling of micromechanical motion to the quantum ground state*, *Nature* **475**, 359 (2011).
- [11] J. Chan, T. M. Alegre, A. H. Safavi-Naeini, J. T. Hill, A. Krause, S. Gröblacher, M. Aspelmeyer, and O. Painter, *Laser cooling of a nanomechanical oscillator into its quantum ground state*, *Nature* **478**, 89 (2011).
- [12] L. Qiu, I. Shomroni, P. Seidler, and T. J. Kippenberg, *Laser Cooling of a Nanomechanical Oscillator to Its Zero-Point Energy*, *Phys. Rev. Lett.* **124**, 173601 (2020).
- [13] M. Aspelmeyer, T. J. Kippenberg, and F. Marquardt, *Cavity optomechanics*, *Rev. Mod. Phys.* **86**, 1391 (2014).
- [14] M. Rossi, D. Mason, J. Chen, Y. Tsaturyan, and A. Schliesser, *Measurement-based quantum control of mechanical motion*, *Nature* **563**, 53 (2018).
- [15] H. M. Wiseman and G. J. Milburn, *Quantum Measurement and Control*, Cambridge University Press, 2010.
- [16] T. van Zoest et al., *Bose-Einstein condensation in microgravity*, *Science* **328**, 1540 (2010).
- [17] S. Gerlich, S. Eibenberger, M. Tomandl, S. Nimmrichter, K. Hornberger, P. J. Fagan, J. Tüxen, M. Mayor, and M. Arndt, *Quantum interference of large organic molecules*, *Nature communications* **2**, 263 (2011).
- [18] E. Hebestreit, *Thermal properties of levitated nanoparticles*, PhD thesis, ETH Zurich, 2017.
- [19] R. Kaltenbaek, G. Hechenblaikner, N. Kiesel, O. Romero-Isart, K. C. Schwab, U. Johann, and M. Aspelmeyer, *Macroscopic quantum resonators (MAQRO) Testing quantum and gravitational physics with massive mechanical resonators*, *Experimental Astronomy* **34**, 123 (2012).
- [20] E. Bonvin, L. Devaud, M. Rossi, A. Militaru, L. Dania, D. S. Bykov, M. Teller, T. E. Northup, L. Novotny, and M. Frimmer, *Hybrid Paul-optical trap with large optical access for levitated optomechanics*, arXiv preprint arXiv:2312.10131 (2023).
- [21] E. Bonvin, L. Devaud, M. Rossi, A. Militaru, L. Dania, D. S. Bykov, O. Romero-Isart, T. E. Northup, L. Novotny, and M. Frimmer, *State expansion of a levitated nanoparticle in a dark harmonic potential*, arXiv preprint arXiv:2312.13111 (2023).
- [22] E. Bonvin, *Hybrid Traps for Coherent State Expansion of a Levitated Nanoparticle*, PhD thesis, ETH Zürich, 2023.
- [23] N. Kiesel, F. Blaser, U. Delić, D. Grass, R. Kaltenbaek, and M. Aspelmeyer, *Cavity cooling of an optically levitated submicron particle*, *Proc. Natl. Acad. Sci.*

- USA **110**, 14180 (2013).
- [24] D. Windey, C. Gonzalez-Ballester, P. Maurer, L. Novotny, O. Romero-Isart, and R. Reimann, *Cavity-Based 3D Cooling of a Levitated Nanoparticle via Coherent Scattering*, Phys. Rev. Lett. **122**, 123601 (2019).
- [25] J. Piotrowski, D. Windey, J. Vijayan, C. Gonzalez-Ballester, A. de los Ríos Sommer, N. Meyer, R. Quidant, O. Romero-Isart, R. Reimann, and L. Novotny, *Simultaneous ground-state cooling of two mechanical modes of a levitated nanoparticle*, Nature Physics, 1 (2023).
- [26] P. F. Cohadon, A. Heidmann, and M. Pinard, *Cooling of a Mirror by Radiation Pressure*, Phys. Rev. Lett. **83**, 3174 (1999).
- [27] M. Poggio, C. L. Degen, H. J. Mamin, and D. Rugar, *Feedback Cooling of a Cantilever's Fundamental Mode below 5 mK*, Phys. Rev. Lett. **99**, 017201 (2007).
- [28] D. Wilson, V. Sudhir, N. Piro, R. Schilling, A. Ghadimi, and T. J. Kippenberg, *Measurement-based control of a mechanical oscillator at its thermal decoherence rate*, Nature **524**, 325 (2015).
- [29] F. Tebbenjohanns, M. Frimmer, V. Jain, D. Windey, and L. Novotny, *Motional Sideband Asymmetry of a Nanoparticle Optically Levitated in Free Space*, Phys. Rev. Lett. **124**, 013603 (2020).
- [30] T. P. Purdy, R. W. Peterson, and C. A. Regal, *Observation of Radiation Pressure Shot Noise on a Macroscopic Object*, Science **339**, 801 (2013).
- [31] V. Jain, J. Gieseler, C. Moritz, C. Dellago, R. Quidant, and L. Novotny, *Direct Measurement of Photon Recoil from a Levitated Nanoparticle*, Phys. Rev. Lett. **116**, 243601 (2016).
- [32] S. Mancini, D. Vitali, and P. Tombesi, *Optomechanical Cooling of a Macroscopic Oscillator by Homodyne Feedback*, Phys. Rev. Lett. **80**, 688 (1998).
- [33] R. Kaltenbaek, G. Hechenblaikner, N. Kiesel, O. Romero-Isart, K. C. Schwab, U. Johann, and M. Aspelmeyer, *Macroscopic quantum resonators (MAQRO)*, Experimental Astronomy **34**, 123 (2012).
- [34] A. J. Leggett, *Testing the limits of quantum mechanics: motivation, state of play, prospects*, Journal of Physics: Condensed Matter **14**, R415 (2002).
- [35] F. Tebbenjohanns, M. Frimmer, and L. Novotny, *Optimal position detection of a dipolar scatterer in a focused field*, Physical Review A **100**, 043821 (2019).
- [36] J. Gieseler, B. Deutsch, R. Quidant, and L. Novotny, *Subkelvin Parametric Feedback Cooling of a Laser-Trapped Nanoparticle*, Phys. Rev. Lett. **109**, 103603 (2012).
- [37] J. Millen, P. Z. G. Fonseca, T. Mavrogordatos, T. S. Monteiro, and P. F. Barker, *Cavity Cooling a Single Charged Levitated Nanosphere*, Phys. Rev. Lett. **114**, 123602 (2015).

REFERENCES

- [38] M. Frimmer, K. Luszcz, S. Ferreiro, V. Jain, E. Hebestreit, and L. Novotny, *Controlling the net charge on a nanoparticle optically levitated in vacuum*, Phys. Rev. A **95**, 061801 (2017).
- [39] J. Ahn, Z. Xu, J. Bang, Y.-H. Deng, T. M. Hoang, Q. Han, R.-M. Ma, and T. Li, *Optically Levitated Nanodumbbell Torsion Balance and GHz Nanomechanical Rotor*, Phys. Rev. Lett. **121**, 033603 (2018).
- [40] E. Hebestreit, M. Frimmer, R. Reimann, C. Dellago, F. Ricci, and L. Novotny, *Calibration and energy measurement of optically levitated nanoparticle sensors*, Rev. Sci. Instr. **89**, 033111 (2018).
- [41] F. van der Laan, R. Reimann, A. Militaru, F. Tebbenjohanns, D. Windey, M. Frimmer, and L. Novotny, *Optically levitated rotor at its thermal limit of frequency stability*, Phys. Rev. A **102**, 013505 (2020).
- [42] F. van der Laan, *Rotational Levitodynamics*, PhD thesis, ETH Zürich, 2022.
- [43] J. Gao, F. van der Laan, J. A. Zielinska, A. Militaru, L. Novotny, and M. Frimmer, *Feedback cooling a levitated nanoparticle's libration to below 100 phonons*, arXiv preprint arXiv:2402.19245 (2024).
- [44] D. E. Chang, C. A. Regal, S. B. Papp, D. J. Wilson, J. Ye, O. Painter, H. J. Kimble, and P. Zoller, *Cavity opto-mechanics using an optically levitated nanosphere*, Proc. Natl. Acad. Sci. USA **107**, 1005 (2010).
- [45] F. Tebbenjohanns, *Linear Feedback Cooling of a Levitated Nanoparticle in Free Space*, PhD thesis, ETH Zürich, 2020.
- [46] A. A. Clerk, M. H. Devoret, S. M. Girvin, F. Marquardt, and R. J. Schoelkopf, *Introduction to quantum noise, measurement, and amplification*, Rev. Mod. Phys. **82**, 1155 (2010).
- [47] A. H. Safavi-Naeini, J. Chan, J. T. Hill, T. P. M. Alegre, A. Krause, and O. Painter, *Observation of Quantum Motion of a Nanomechanical Resonator*, Phys. Rev. Lett. **108**, 033602 (2012).
- [48] F. Tebbenjohanns, M. Frimmer, A. Militaru, V. Jain, and L. Novotny, *Cold damping of an optically levitated nanoparticle to microkelvin temperatures*, Physical review letters **122**, 223601 (2019).
- [49] T. P. Purdy, K. E. Grutter, K. Srinivasan, and J. M. Taylor, *Quantum correlations from a room-temperature optomechanical cavity*, Science **356**, 1265 (2017).
- [50] A. B. Shkarin, A. D. Kashkanova, C. D. Brown, S. Garcia, K. Ott, J. Reichel, and J. G. E. Harris, *Quantum Optomechanics in a Liquid*, Phys. Rev. Lett. **122**, 153601 (2019).
- [51] V. Sudhir, D. J. Wilson, R. Schilling, H. Schütz, S. A. Fedorov, A. H. Ghadimi, A. Nunnenkamp, and T. J. Kippenberg, *Appearance and disappearance of quantum correlations in measurement-based feedback control of a mechanical*

- oscillator*, Physical Review X **7**, 011001 (2017).
- [52] C. Sayrin et al., *Real-time quantum feedback prepares and stabilizes photon number states*, Nature **477**, 73 (2011).
- [53] R. Vijay, C. Macklin, D. Slichter, S. Weber, K. Murch, R. Naik, A. N. Korotkov, and I. Siddiqi, *Stabilizing Rabi oscillations in a superconducting qubit using quantum feedback*, Nature **490**, 77 (2012).
- [54] L. Magrini, P. Rosenzweig, C. Bach, A. Deutschmann-Olek, S. G. Hofer, S. Hong, N. Kiesel, A. Kugi, and M. Aspelmeyer, *Optimal quantum control of mechanical motion at room temperature: ground-state cooling*, 2020.
- [55] S. Burd, R. Srinivas, J. Bollinger, A. Wilson, D. Wineland, D. Leibfried, D. Slichter, and D. Allcock, *Quantum amplification of mechanical oscillator motion*, Science **364**, 1163 (2019).
- [56] O. Romero-Isart, A. C. Pflanzer, F. Blaser, R. Kaltenbaek, N. Kiesel, M. Aspelmeyer, and J. I. Cirac, *Large Quantum Superpositions and Interference of Massive Nanometer-Sized Objects*, Phys. Rev. Lett. **107**, 020405 (2011).
- [57] E. E. Wollman, C. Lei, A. Weinstein, J. Suh, A. Kronwald, F. Marquardt, A. A. Clerk, and K. Schwab, *Quantum squeezing of motion in a mechanical resonator*, Science **349**, 952 (2015).
- [58] M. Xin, W. S. Leong, Z. Chen, Y. Wang, and S.-Y. Lan, *Rapid quantum squeezing by jumping the harmonic oscillator frequency*, Physical Review Letters **127**, 183602 (2021).
- [59] E. Hebestreit, M. Frimmer, R. Reimann, and L. Novotny, *Sensing Static Forces with Free-Falling Nanoparticles*, Phys. Rev. Lett. **121**, 063602 (2018).
- [60] D. S. Lemons and A. Gythiel, *Paul Langevin's 1908 paper "On the Theory of Brownian Motion" ["Sur la thiorie du mouvement brownien," CR Acad. Sci.(Paris) 146, 530-533 (1908)]*, American Journal of Physics **65**, 1079 (1997).
- [61] J. Mostowski and J. Pietraszewicz, *Wigner function for harmonic oscillator and the classical limit*, arXiv preprint arXiv:2104.06638 (2021).
- [62] J. M. T. Thompson and H. B. Stewart, *Nonlinear dynamics and chaos*, John Wiley & Sons, 2002.
- [63] B. H. Bransden and C. J. Joachain, *Introduction to quantum mechanics*, (1989).
- [64] R. Clausius, *XVI. On a mechanical theorem applicable to heat*, The London, Edinburgh, and Dublin Philosophical Magazine and Journal of Science **40**, 122 (1870).
- [65] M. Frimmer, K. Luszcz, S. Ferreira, V. Jain, E. Hebestreit, and L. Novotny, *Controlling the net charge on a nanoparticle optically levitated in vacuum*, Physical Review A **95**, 061801 (2017).
- [66] J. Gieseler, B. Deutsch, R. Quidant, and L. Novotny, *Subkelvin parametric*

REFERENCES

- feedback cooling of a laser-trapped nanoparticle*, Physical review letters **109**, 103603 (2012).
- [67] G. Duffing, *Erzwungene Schwingungen bei veränderlicher Eigenfrequenz und ihre technische Bedeutung*, Number 41-42, Vieweg, 1918.
- [68] *MFLI User Manual, PID/PLL Tab*, https://docs.zhinst.com/mfli_user_manual/functional_description/pid.html, Accessed: 2023/12/31.
- [69] M. Kamba, R. Shimizu, and K. Aikawa, *Optical cold damping of neutral nanoparticles near the ground state in an optical lattice*, Optics Express **30**, 26716 (2022).
- [70] M. Kamba, R. Shimizu, and K. Aikawa, *Nanoscale feedback control of six degrees of freedom of a near-sphere*, Nature Communications **14**, 7943 (2023).
- [71] J. Vijayan, Z. Zhang, J. Piotrowski, D. Windey, F. van der Laan, M. Frimmer, and L. Novotny, *Scalable all-optical cold damping of levitated nanoparticles*, Nature Nanotechnology **18**, 49 (2023).
- [72] P. Micke, J. Stark, S. A. King, T. Leopold, T. Pfeifer, L. Schmöger, M. Schwarz, L. J. Spieß, P. O. Schmidt, J. R. C. López-Urrutia, and et al., *Closed-cycle, low-vibration 4 K cryostat for ion traps and other applications*, Rev. Sci. Instr. **90**, 065104 (2019).
- [73] A. Einstein, *Über die von der molekularkinetischen Theorie der Wärme geforderte Bewegung von in ruhenden Flüssigkeiten suspendierten Teilchen*, Annalen der physik **4** (1905).

List of Publications

This thesis is based in part on the following publication:

F. Tebbenjohanns¹, **M. L. Mattana¹**, M. Rossi¹, M. Frimmer, and L. Novotny, *Quantum control of a nanoparticle optically levitated in cryogenic free space*, *Nature* **565**, 378 (2021), doi: 10.1038/s41586-021-03617-w, URL <https://www.nature.com/articles/s41586-021-03617-w>.

¹These authors contributed equally.

Curriculum Vitae

Maria Luisa Mattana, born on the 30th of April 1995, in Cagliari, Sardegna, Italy.

Professional experience

- 2020 – 2024 Doctoral Researcher,
Photonics Laboratory, ETH Zurich, Switzerland
- 2020 Research Assistant,
Photonics Laboratory, ETH Zurich, Switzerland
- 2019 Research Assistant & Master Thesis Intern,
Quantum Optoelectronics Laboratory, ETH Zurich,
- 2018 Student Intern,
Finley Group, Walter Schottky Institute, Munich, Germany

Education

- 2017 – 2018 Master of Science in Physics,
Università degli Studi di Cagliari, Sardegna, Italy
- 2014 – 2017 Bachelor of Science in Physics,
Università degli Studi di Cagliari, Sardegna, Italy